Ministerul Cercetării și Inovării

ifa

EUROfusion

Romanian Participation in EUROfusion

Annual Report 2016

Bucharest-Magurele, ROMANIA
2016

Institute of Atomic Physics

Romanian Participation in EUROfusion

Annual Report 2016

Institute of Atomic Physics

http://www.ifa-mg.ro/index.php

Acknowledgments

This work has been carried out within the framework of the EUROfusion Consortium and has received funding from the Euratom research and training programme 2014-2018 under grant agreement No 633053. The views and opinions expressed herein do not necessarily reflect those of the European Commission.

The work carried out on complementary projects has been received funding from the Romanian National Education Ministry / Institute of Atomic Physics under contract 1EU-6/2014 and 2/2016.

Foreword

EUROfusion, the '*European Consortium for the Development of Fusion Energy*' (*https://www.euro-fusion.org/*), is a consortium of national fusion research institutes located in the European Union and Switzerland. It was established in 2014 to succeed the European Fusion Development Agreement (EFDA - *https://en.wikipedia.org/wiki/European_Fusion_Development_Agreement*) as the umbrella organisation of Europe's fusion research laboratories. The consortium is currently funded by the Euratom Horizon 2020 programme. EUROfusion manages and funds European fusion research activities on behalf of Euratom. Thirty research organisations and universities from 26 European Union member states plus Switzerland and Ukraine signed the EUROfusion consortium agreement. In addition, more than 100 Third Parties contribute to the research activities through the Consortium members. EUROfusion collaborate with Fusion for Energy (*http://fusionforenergy.europa.eu/*) and intensively support the ITER International Organization (*www.iter.org*).

EUROfusion funds fusion research activities in accordance with the Roadmap to the realization of fusion energy (*https://www.euro-fusion.org/wpcms/wp-content/uploads/2013/01/JG12.356-web.pdf*). The Roadmap outlines the most efficient way to realize fusion electricity. It is the result of an analysis of the European Fusion Programme undertaken in 2012 by the Research laboratories within EFDA. Its main objectives are: the preparation for the experiments on ITER, the world's largest tokamak, a magnetic fusion device that has been designed to prove the feasibility of fusion as a large-scale and carbon-free source of energy based on the same principle that powers our Sun and stars and the development of the concepts for the fusion power demonstration plant DEMO (https://www.euro-fusion.org/newsletter/demo-and-the-road-to-fusion-power/). The roadmap breaks the overall task into eight missions:

- **Plasma regimes of operation:** as plasmas must be confined at temperatures 20 times higher than the temperature of the core of the sun it is necessary to minimize the energy losses due to small-scale turbulence and the taming of plasma instabilities.
- **Heat-exhaust systems:** the power necessary to maintain plasmas at high temperatures is ultimately exhausted in a narrow region of the reaction chamber called the divertor. The need to withstand large heat loads led to the development of plasma facing materials and exhaust systems that should be adequate for ITER.
- **Neutron resistant materials:** The ultimate goal is to produce suitable structural and high-heat flux materials that will be able to ensure efficient electricity production and adequate plant availability; they also need to exhibit reduced activation so as to avoid permanent waste repositories.
- **Tritium self-sufficiency:** efficient breeding and extraction systems to minimize tritium inventory are necessary as DEMO will burn about 0.4kg of tritium per operational day; the choices of the materials and the coolant of the breeding blanket will have to be made consistently with the choice of the components for the transformation of the high-grade heat into electricity
- **Implementation of the intrinsic safety features of fusion:** fusion has intrinsic safety features which should be implemented in a coherent architecture in order to ensure the inherent passive resistance to any incidents and to avoid the need of evacuation in the worst incident case. The development of methods for reducing the problem associated with the presence of tritium in the components extracted for disposal and the definition of appropriate disposal routes are the main requirements.
- **Integrated DEMO design and system development:** compared to ITER, DEMO will need a more efficient technical solution for remote maintenance as well as highly reliable components; in addition, DEMO will need to exploit a highly efficient heat transfer and associated electrical generation systems.
- **Competitive cost of electricity:** the perspective of economic electricity production from fusion has to be set as a target, e.g. minimizing the DEMO capital costs. In order to meet this target, we must build on the experience of ITER, design solutions demonstrating a reliable plant with a high availability and serve as a credible data basis for commercial energy production.
- **Stellarators:** an additional objective is to bring the stellarator line to maturity as a possible long-term alternative to tokamaks. Stellarators have indeed intrinsic advantages relative to the tokamak, but their physics basis is not mature enough to achieve the goal of electricity from fusion by 2050.

EUROfusion funds the Research Units in accordance with their participation to the mission-oriented Work Packages outlined in the Consortium Work Plan. The Institute of Atomic Physics (IAP – *www.ifa-mg.ro*) is a member of the EUROfusion since the establishment of the Consortium, in 2014. IAP ensures the management of the Romanian participation in EUROfusion by coordinating the activity of 5 research institutes:

- *National Institute of Laser, Plasma and Radiation Physics (NILPRP),*
- *National Institute of Cryogenic and Isotope Technology (NICIT),*
- *National Institute for Research and Development in Optoelectronics (INOE 2000),*
- *National Institute of Physics of Materials (NIPM),*
- *National Institute of Physics and Nuclear Engineering (NIPNE)*

and three universities:

- *University of Craiova (UCv),*
- *University A. I. Cuza from Iasi (UAIC),*
- *Technical University Cluj-Napoca (UTCN).*

which acts as linked-third-parties inside the Consoritum.

The Romanian reasearch activities have been developed manly inside the ITER Physics workpackages:

- *WPJET1 (JET campaigns)*
- *WPJET2 (JET Plasma-Facing Components)*
- *WPJET4 (JET Enhancements)*
- *WPPFC (Preparation of efficient PFC operation for ITER and DEMO)*
- *WPCD (Code Development for Integrated Modelling)*
- *WPMST1 (Medium-Size Tokamak campaigns)*
- *WPISA (Infrastructure Support Activities)*
- *WPSA (Preparation of exploitation of JT-60SA)*
-

and also in the framework of Power Plant Physics and Technology department:

- *WPMAG - Magnets system project*
- *WPMAT - Materials project*

A consistent contribution has also been brought for the ‚*Enabling Research*' (WPENR) work package. In addition to the mission-oriented work, WPENR aims at promoting fundamental understanding and longer research perspective dedicated to nuclear fusion.

The 'Education' work package (WPEDU) has ensured the support for several PhD and Master students studying different aspects of nuclear fusion science and technology.

The main results of these research activities are presented in this report together with a comprehensive list of publications.

Content

Confinement degradation and improvement in turbulent plasmas

M. Vlad[1], F. Spineanu[1], D.I. Palade[1], M. Croitoru[1], A. Zubarev[1], I. Petrisor[2], D. Constantinescu[2], M. Negrea[2]

[1]*National Institute for Lasers, Plasma and Radiation Physics, Bucharest-Magurele, Romania*

[2]*University of Craiova, Craiova, Romania*

WP-ENR-C

The aim of the project is to clarify the dual nature of some basic plasma processes, which are exhibited in the extreme conditions of a reactor: the turbulence and the magnetic stochasticity can lead both to degradation and improvement of confinement, with possible fast switching between these two manifestations. Our main instrument is the decorrelation trajectory method (DTM), a semy-analytic description of the statistics of the test particle trajectories, which proved to be sensitive to details of turbulence. It is supported by studies based on low-order Hamiltonian dynamics and by numerical calculations. The main results obtained in 2016 are:

- We have shown that radial variation of the amplitude of the turbulence (that always appears in experiments and numerical simulation) determines a new pinch mechanism. We have studied this process using the DTM in a realistic model of plasma turbulence. The dependence of the pinch velocity on turbulence parameters was determined. The conclusion the maximum of the convection velocity appears in the range of the transition from quasilinear to nonlinear transport. However, the maximum effect on plasma profiles that is determined by the peaking factor does not correspond to these range but to the nonlinear transport, characterized by smaller convection velocity.
- The effects of the neoclassical drifts on turbulent transport were analyzed by developing the test particle model and the DTM. The magnetic drifts determine a perpendicular decorrelation mechanism that competes with the parallel decorrelation. These effects are analyzed as function of turbulence parameters in both transport regimes. The conclusion is that the magnetic drift contributes to improved confinement in the quasilinear transport and that it has a weak effect in the nonlinear case.
- The combined effects of the stochastic magnetic field produced by the RMPs and of particle collisions were analyzed in a realistic model [1]. We have found that the effects observed in experiments (increased turbulent transport and generation of outward pinch) occur even when the turbulence is not modified by the RMPs. A direct influence of the RMPs on transport is produced through a decorrelation mechanism. Both RMPs and collisions have synergistic effects on the turbulent transport (small direct contributions and much larger variations of the turbulent transport coefficients). This is a nonlinear process determined by the space correlation of the stochastic potential. The results show that at high collisionality the transport is weakly affected by the RMPs, and that at low collisionality the RMPs determine significant degradation of the confinement. This effect appears in the nonlinear regime of the turbulent transport, while the quasilinear transport does not depend on the collisionality. The confinement degradation due to RMPs is a decreasing function of turbulence amplitude, which accounts for an interesting effect. The change of turbulence amplitude has an opposite effect on the degradation of the confinement. Namely, if the RMPs determine the increase of turbulence amplitude, then the confinement degradation is smaller than estimated at fixed amplitude. On the contrary, if the turbulence is attenuated, the degradation is larger than in the case of unchanged turbulence. According to our model, the results of the present experiments cannot be directly extrapolated to ITER conditions, because confinement degradation strongly increases with the product of the RMPs amplitude and plasma size.
- The first results in the development of an iterated self-consistent (ISC) description of turbulence evolution obtained in 2015 were developed in the present stage for the complex case of the nonlinear drift turbulence [2]. The ISC is a semi-analytic method based on the iterated analysis of the test modes and of the statistics of the stochastic trajectories. A computer code was developed, which calculates the evolution of turbulence spectrum. It is very fast (run times of few hours on a laptop), since it does not perform simulations of the turbulence. We have found two types of evolution depending on the strength of the drive of the instability. Drift turbulence evolution at weak drive is essentially determined by ion diffusion, which reduces the growth rate and determines a significant change of the spectrum that prevents the development of the coherent effects produced by trapping. The latter are important in the case of strong drive, where ion trajectories acquire both random and the quasi-coherent characteristics. Structures of trajectories are

generated. They influence the evolution of the drift turbulence by three mechanisms. One in the decrease (up to negative values) of the growth rates of the test modes on the fraction of trapped trajectories and on the size of the structures. The increase of the structures determines the generation of the zonal flow modes, which represent the second possible influence on the drift turbulence. Their action is indirect and consists of the modification of the diffusion and/or of the structures. The third mechanism is provided by the diffusion, which can be strongly changed by the structures.

- The study of the effects of turbulence on the transport of the fusion particles was finalized [3].
- A detailed study of the effects of the shear on the diffusion of the magnetic field lines was developed. The dispersion of the magnetic lines was analyzed for several spectra including the model proposed by Shalchi and Weinhorst and a Gaussian one. The diffusion coefficients in the radial and poloidal directions have been calculated using the quasi-linear method and the decorrelation trajectory method. The results are published in Phys. Plasmas [4], in [5] and [C5].
- We have studied a class of non-local models for the anomalous transport in fusion plasmas [C2-C4]. The framework of a general model that includes memory effects and asymmetric processes has been developed. A code based on the matrix approach and on the approximation of fractional derivatives through numerically computed Grundwald-Letnikov derivatives was constructed.

Determination of the effects of the constraint of the MHD invariant that connects the vorticity, current profile and density

F. Spineanu, M. Vlad, D. Palade, A. Croitoru, A. Zubarev

National Institute for Lasers, Plasma and Radiation Physics, Romania

WPENR-C

We propose to examine the states of tokamak plasma as resulting from invariances of topological, Lagrangian and "frozen-in" nature. The states of equilibria correspond to extrema of some functionals, like - for example - the rate of production of entropy. For a turbulent medium (as plasma usually is) the minimum rate of production of entropy is a valid principle governing the evolution of the system. The main parameters have only slow variation and the plasma is close to a static state, if it were ideal. When a system is driven, it accumulates substantial departures from equilibrium state and, left to relax, will produce maximum entropy. This behavior has created some theoretical confusion, but actually it is reasonably transparent: when a system relaxes from a state which was far from equilibrium, it evolves under the principle of maximum rate of entropy production. After reaching an equilibrium state, the slow drive that still exists induces an evolution governed by the minimum rate of entropy production. It is in this picture that we have to insert the presence of structures in a background of turbulence.

To understand and predict properties of the tokamak plasma it is necessary to investigate turbulent-induced transport processes and, of equal importance, coherent structures (like zonal flows, H-mode rotation layers and convective cells). The analytical and numerical approaches and the methods are however largely different, from statistical theory to exact integrability. It is then helpful to remember that both physical aspects, even if different in their manifestation, must obey a basic set of constraints which are due to the existence of Lagrangian invariants and of frozen-in invariants. The invariants are constraints that must be verified by any dynamical evolution of the system. In general for real plasma (*i.e.* with finite resistivity and viscosity) the invariance property can only be approximative, but the high temperature (typical for fusion reactor) reduces the collisional effects even in regions close to the plasma edge. Then the persistence of some invariants can still be used as a benchmark for our analytical models and for numerical simulations, similar to the conservation of the energy or the angular momentum.

We have investigated the invariants that include in their expression the plasma vorticity $\boldsymbol{\omega} = \nabla \times \mathbf{v}$, *i.e.* the sheared plasma rotation, which has constantly been proven an important factor in the confinement. Before applying to practical cases we explain the difference relative to topological invariants (non-local) like the Gauss linking number. The invariants for fluids, as introduced by Sagdeev Moiseev Tur and Yanovskii are defined and it is shown that the Ertel's theorem is a realization of this general structure. The Ertel's theorem is the origin of the quasi-three-dimensional description of the drift waves, where the Boltzmann response of the electrons imposes to account for the ion polarization drift, leading to the Hasegawa-Mima equation. This theorem is extended to a relationship between the magnetic field and the density, an invariant that is characterized by Yankov as expressing the "freeze-in" of tokamak plasma in the poloidal magnetic field. We make a comparison between the Turbulent Equipartition theory where the same combination (density divided to the magnetic field) is derived.

Finally we introduce the MHD invariant that combines the density, the vorticity and the magnetic field, an extension of both the Ertel's theorem and of the Yankov invariant. Two applications are made:

1. We show that a pellet that penetrates deep into the plasma (possibly from the High Field Side) will produce a radial current and implicitely a torque and poloidal plasma rotation. Then the invariant finds that there is a density of current located in the regions of sheared rotation. This is a source of reversal of the radial profile of the safety factor.
2. We examine the situation of the rotation layer at the edge in the H-mode. The accumulation of current density in order to preserve the invariance where the sheared vorticity is high goes beyond the bootstrap current generated in the pedestal. This is very important.

The diffusion coefficients evaluation of the magnetic field lines in magnetic turbulence

M. Negrea[1], I. Petrisor[1], D. Constantinescu[2]

[1]*University of Craiova, Department of Physics*

[2]*University of Craiova, Department of Applied Mathematics*

WPENR-C

In astrophysical plasmas, magnetic field lines represent a guide for the motions of thermal and non-thermal particles. The Field Line Random Walk (FLRW) is considered to depend on the magnetic Kubo number that reflects the level of turbulence of the magnetic field itself. Therefore it is very important to study the (FLRW) as a fundamental problem in order to understand the motion of energetic particles such as cosmic rays. In our work we included the effect of magnetic shear because it was shown in the literature that in astrophysics the magnetic shear influences the change of the energy in flares and we used the decorrelation trajectory (DCT) method in order to calculate the magnetic diffusion coefficients. For fusion plasma the DCT is a method that permits to analyze the high Kubo levels situations; it is also a semi-analytical method, the numerical calculations involved in are not very much time consuming. We have already compared the results obtained by DCT with those obtained by numerical simulations. The main idea of the method is to study the FLRW in subensembles S of the realizations of the stochastic functions that have given values of the the magnetic potential.

The FLRW is studied in the 2D + magnetic sheared model as a function of magnetic Kubo number K and the shear parameter K_s. By the DCT approach (a semi-analytical method), we determined the running diffusion coefficients from a set of deterministic trajectories obtained from the Eulerian correlation of the magnetic potential. The study is important for the nonlinear regime that is characterized by field line trapping and is important for space plasmas because there is clear evidence that the magnetic turbulence can be characterized by large Kubo numbers. Trapping is negligible for $K<1$, it is statistically relevant for $K>1$ and generates stochastic magnetic islands and is influenced by the magnetic shear parameter also. There is no general consensus on how to model the FLRW. The quasi-two-dimensional (quasi- $2D$) case, dominated by wave vectors nearly perpendicular to the main magnetic field B_0 is characterized by strong trapping effects in which some field lines are trapped in the geometrical structures temporarily or permanently.
The celebrated Corrsin approximation includes the quasilinear and Bohm approximations. The Corrsin approximation consists in two hypothesis: (a) the statistical independence between the particle trajectories and the stochastic velocity field and (b) the displacements have a Gaussian distribution. In our paper, the geometrical point localized on a magnetic field line plays the role of the test particle. The Corrsin approximation is a very good approximation for a Kubo number in the range $K<1$.
We have developed for our model the specific main tools of the DCT method whose idea concerns in the study of the Langevin system not in the whole space of the realizations of the magnetic potential fluctuations; the whole space is subdivided into *subensembles* S, characterized by given values of the potential and of the fluctuating field components at the starting point of the trajectories [P1-P3]. There is a strong correlation between the turbulence in the solar wind and geomagnetic activity, indicating that turbulence is an important mechanism to provide the coupling of the solar wind to the Earth's magnetosphere. We extended the DCT tools in the study of the diffusion of magnetic field lines in a solar wind taking into account for the anisotropic turbulence and the magnetic shear. The magnetic field model and the corresponding Langevin equations for the sheared stochastic magnetic field are established. The auto and cross correlations involving directly fluctuating magnetic field components $b_n(\mathbf{x};z)$ and the magnetic potential $\psi(\mathbf{x};z)$ are calculated and the DCT tools and some DCT trajectories are considered for a given subensemble, a fixed level of turbulence $K=5$ and different shear parameters $K_S = \{0, 1, 5\}$. Finally the running and the asymptotic diffusion coefficients are studied for different levels of the level of turbulence and of the shear Kubo parameter are analyzed.

We have also studied the bifurcations in a family of Hamiltonian systems and associated nontwist cubic maps. The aim of the work was to study systems with one-and-a-half degrees of freedom generated by a Hamiltonian with a quartic unperturbed part and broad perturbation spectrum. Interesting properties of the dynamics of the Poincare-Birkhoff or dimerised chains, such as pairs of homoclinic orbits to the same equilibrium point (sandglass) and triple reconnection were pointed out. Then the scenario of reconnections was used to explain the destruction of transport barriers in mathematical models for magnetic field configurations in tokamaks.

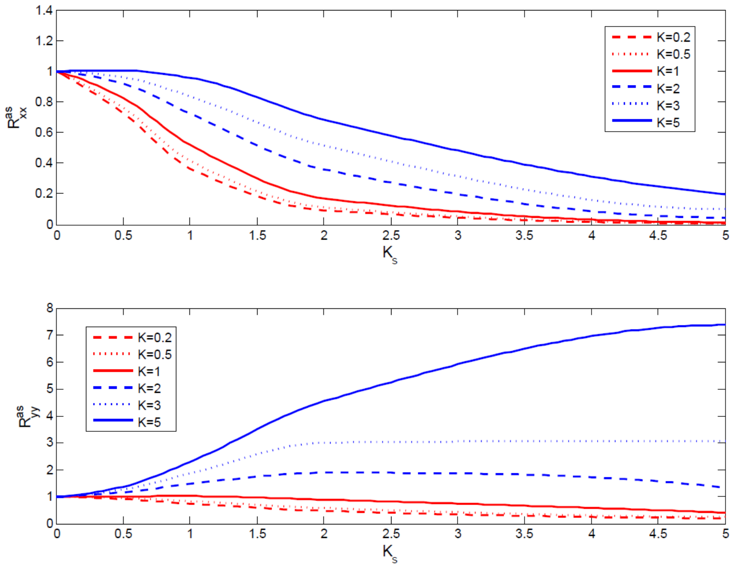

Figure 1 - Ratios of asymptotic diffusion coefficients as functions of the shear parameter K_s

We have also studied the fractional transport in turbulent reconnection. The energization of particles in a large scale environment of turbulent reconnection that is fragmented into a large number of randomly distributed Unstable Current Sheets was statistically analyzed in two important cases of energization mechanisms: electric field acceleration and acceleration by reflection at contracting magnetic islands. It was shown that the classical Fokker-Planck (FP) fails to reproduce the test particle simulation results. The reason is that transport in energy space is highly anomalous (strange), the particles perform Levy flights, and the energy distributions show extended power-law tails. This motivates the use of a fractional transport equation (FTE) whose specific form was derived. Its parameters and the order of the fractional derivatives were determined from the simulation data, and it was shown that the corresponding FTE is able to reproduce the simulation data very well.

The Creation of Finite Element Matrix Representation of the Energy Functional for Inductively Driven Eddy Currents by Using the Same Approach as for the Sink/Source Surface Currents

C.V. Atanasiu[1], L.E. Zakharov[2], K. Lackner[3], M. Hoelzl[3], E. Strumberger[3]

[1]*National Institute for Laser, Plasma and Radiation Physics, Romania*

[2]*Princeton Plasma Physics Laboratory, Princeton, USA*

[3]*Max Planck Institute for Plasma Physics, Garching, Germany*

WP-CD-P

The understanding of plasma disruptions in tokamaks and predictions of their effects require realistic simulations of electric currents excitation in 3-dimensional vessel structures by the plasma touching the walls. The Wall Touching Kink Modes (WTKM) are frequently excited during the Vertical Displacement Events (VDE) and cause big sideways forces on the vacuum vessel which are difficult to confront in large tokamaks. For the purpose of WTKM modelling the surface current density $\mathbf{j}d_w$ in the conducting shell has been split into two components ($\mathbf{j}$ is the current density in the wall of thickness d_w): (a) one is a divergence free surface current $\mathbf{i}$ and (b) the second one is a current proportional to $\nabla\Phi^S$ with potentially finite divergence in order to describe the plasma sink/source of the wall current. If in a previous task, we have developed a methodology to calculate the plasma sink/source surface current, in the present task we have developed a Finite-Element matrix representation of the energy functional for inductively driven eddy currents by using the same approach as for the Sink/Source surface currents (SSC). Thus, it is possible the calculate the eddy surface currents in 3D thin wall with holes given the external time dependent magnetic flux.

For the purpose of WTKM modelling the surface current density $\mathbf{j}d_w$ in the conducting shell can be split into two components:

$$d_w\mathbf{j} = \mathbf{i} - \sigma\nabla\emptyset^S, \qquad \mathbf{i} \equiv \nabla I \times \mathbf{n}, \qquad (\nabla\cdot\mathbf{i}) = 0.$$

Here, I is the stream function of the divergence free component and $\mathbf{n}$ the unit normal vector to the wall. The second term, containing the gradient of a surface function Φ^S which we call here the plasma source potential, is the surface current originated from the shearing of the electric current between the plasma and the wall.

For the divergence-free part $\mathbf{i}$ of the surface current the energy principle looks like

$$W^I \equiv \frac{1}{2}\int\left\{\frac{\partial(\mathbf{i}\cdot\mathbf{A}^I)}{\partial t}+\frac{1}{d_w}|\nabla I|^2+2\left(\mathbf{i}\cdot\frac{\partial\mathbf{A}^{ext}}{\partial t}\right)\right\}ds - \oint(\emptyset^E-\emptyset^S)\frac{\partial I}{\partial l}dl.$$

The first inductive term in the surface integral represents the change of magnetic energy of the current $\mathbf{i}$. $\mathbf{A}^\mathbf{I}$ is its vector potential, the second term describes resistive losses, and the third one represents excitation of the current by the other sources. Φ^E is some electrical potential, while Φ^S, as already mentioned, is the potential of the source/sink surface current.

The divergence-free part of the surface current in the thin wall is described by the diffusion equation for the stream function $I(t,u,v)$ in a curvilinear coordinate system u,v

$$\nabla^2 I(t,u,v) = d_w\sigma\frac{\partial B_\perp(t,u,v)}{\partial t}$$

with $B\perp$ the normal to the wall component of the magnetic field, d_w the wall thickness and σ the electrical conductivity of the wall. The plasma perturbations are typically represented as a set of toroidal harmonics with a toroidal wave number n, each containing many coupled poloidal Fourier harmonics.
The equation to be solved looks like

$$\frac{\partial(\mathbf{n}\cdot\mathbf{B})}{\partial t} = d\frac{\partial(\frac{\mathbf{n}}{d_w}\cdot\mathbf{B})}{\partial t} = \frac{1}{D}\left\{\frac{\partial}{\partial u}\left[\frac{1}{\sigma d_w}\left(\frac{g_{vv}}{D}\frac{\partial I}{\partial u} - \frac{g_{uv}}{D}\frac{\partial I}{\partial v}\right)\right] + \frac{\partial}{\partial u}\left[\frac{1}{\sigma d_w}\left(\frac{g_{uu}}{D}\frac{\partial I}{\partial v} - \frac{g_{uv}}{D}\frac{\partial I}{\partial u}\right)\right]\right\}$$

g_{ik} are the metric coefficients, while D is the Jacobian of the coordinate transformation. This equation is solved iteratively, when the source term is considered as known in space and time at each iteration. Then, the contribution of the wall calculated currents is included to the source in the next iteration. To determine $I(u,v)$, appropriate boundary conditions have been determined.

Our numerical results are presented in Figure 1.

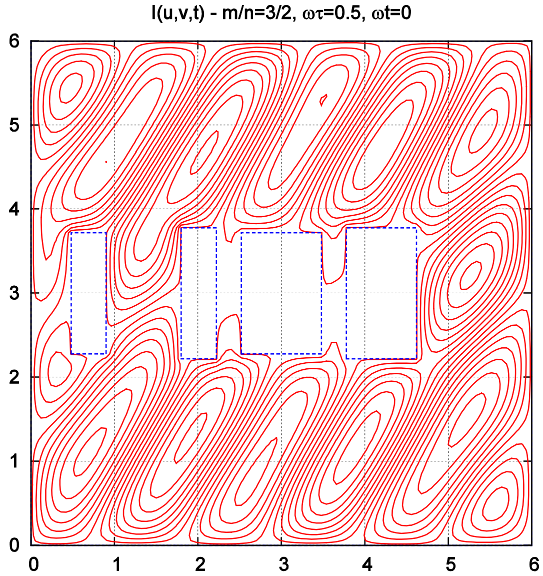

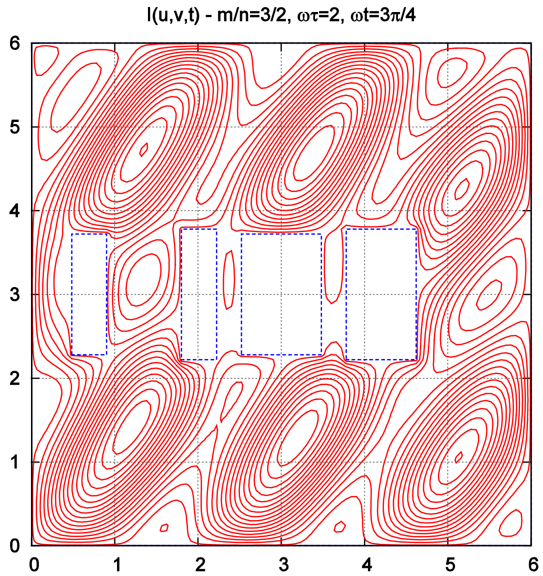

Figure 1 - Constant I lines (same incremental levels for figures with the same $\omega\tau$ value) in a toroidal wall with elliptical cross-section and holes, in the presence of a rotating plasma. The perturbed magnetic field of the plasma has been considered as $B^{pl}{}_{\perp}=B_0\exp[\gamma^r t]\sin(mu-nv+\omega t)$, with B_0=0.1 T, aspect ratio R_0/r=3, wall thickness d_w=0.001 m and $\sigma=10^6$ S/m. Different phases ωt, at constant $\omega\tau$ values have been considered, with τ the characteristic time of the wall $\tau=\mu_0 r d_w \sigma$. A vanishing growth rate γ^r has been considered.

Developing of Analytical Test Case to Check Our Code for Sink/Source Surface Currents Determination in a Tokamak Wall During a Wall Touching Kink Mode

C.V. Atanasiu

National Institute for Laser, Plasma and Radiation Physics, Romania

WP-CD-C

During plasma disruptions in tokamaks, electric currents are excited in the three-dimensional vessel structures by a plasma Wall Touching Kink Mode (WTKM). These modes are frequently excited during a Vertical Displacement Event (VDE) and cause big sideways forces on the vacuum vessel which are difficult to confront. To understand the plasma disruptions in tokamaks and to predict their effects, realistic simulations of these electric currents are required. A wall model and numerical code to describe the current shearing between the plasma and the wall in a thin wall has been developed. In the present work, a complex analytical example with pure homogeneous Neumann B.C., has been developed to check the accuracy of our source/sink code.

For the purpose of WTKM modeling the surface current density $\mathbf{j}d_w$ in the conducting shell can be split into two components ($\mathbf{j}$ is the current density in the wall of thickness d_w): (a) one is a divergence free surface current $\mathbf{i}$ and (b) the second one is a current proportional to $\nabla\Phi^S$ with potentially finite divergence in order to describe the plasma sink/source current:

$$d_w\mathbf{j} = \mathbf{i} - \sigma\nabla\emptyset^S,\ \ \mathbf{i} \equiv \nabla I \times \mathbf{n},\ \ (\nabla\cdot\mathbf{i}) = 0. \tag{1}$$

Here, I is the stream function of the divergence free component and $\mathbf{n}$ the unit normal vector to the wall. The second term containing the gradient of a surface function Φ^S which we call here the plasma source potential, is the surface current originated from the shearing of the electric current between the plasma and the wall. We include the electric conductivity σ, potentially non-constant, as a factor in order to decouple the equations for I and Φ^S. The current potential is determined from the equation

$$\big(\nabla\cdot(h\mathbf{j})\big) = -\big(\nabla\cdot(\sigma d_w\nabla\emptyset^S)\big) = -\mathbf{j}_{\mathrm{JOREK}}\cdot\mathbf{n} = -j_\perp, \tag{2}$$

where $j_\perp$ is the density of the current coming from/to the plasma and acting as a galvanic source for the surface currents on the wall. It should be determined by the physics of the plasma-wall contact, which is beyond the scope of the present task. The equation for Φ^S can be obtained by minimizing the functional W^S

$$W^S = \int\{\tfrac{\sigma d_w(\nabla\emptyset^S)^2}{2} + j_\perp\emptyset^S\}dS - \tfrac{1}{2}\oint\emptyset^S\,\sigma d_w[(\mathbf{n}\times\boldsymbol{\nabla}\emptyset^S)\cdot d\mathbf{l} \tag{3}$$

Here the surface integral dS is taken along the wall surface, while the contour integral $d\mathbf{l}$ is taken along the edges of the conducting surfaces with the integrand representing the surface current normal to the edges.

To check our numerical results, we have considered $d_w\sigma$ =1 in Eq. (2) and defined a particular thin wall geometries where we can draw an analytical solution for $\emptyset^S$, satisfying the 2D Poisson equation with pure homogeneous Neumann B.C.:

$$\nabla\cdot(\nabla\emptyset^S) = f(u,v) \tag{4}$$

(u,v) are the curvilinear coordinates describing the tokamak wall. u is the toroidal coordinate, while v represents the poloidal coordinate. The following existence condition has to be satisfied:

$$\int_\Omega j_\perp d\,\Omega = \int_{\partial\Omega}\nabla\emptyset^S\cdot\mathbf{n}dS$$
$$\Omega = \Omega_e\ \backslash\ \Omega_i;\quad \partial\Omega = \Gamma_e\cup\Gamma_i \tag{5}$$

where Ω_e is the domain of the wall, Ω_i is the domain of the hole, while Γ_e and Γ_i are the boundaries of the wall and hole respectively. We have considered the tokamak shell with elliptical cross-section and three holes given in Fig.1.1. The correspondent geometry in a curvilinear coordinate system *(u, v)* is given in Fig. 1.2.

The analytical solution of Eq. (4) is chosen in the form:

$$\Phi^S(u,v) = \int G_u(u)du\cdot\int G_v(v)dv \tag{6}$$

$$G_u(u) = \Pi(u-u_{ik});\ i = 0{,}3,\ k = 1{,}2 \tag{7}$$

and in a similar manner, $G_v(v)$. Different solutions $\Phi^S(u,v)$ of Eq. (4) satisfying pure Neumann boundary conditions on wall and hole boundaries (with the geometry given in Fig. 1.2) are presented in Figs.3. The correspondent constant $\Phi^S(u,v)$ lines are reported in Figs. 2.1, for the analytical solution and in Fig. 2.2. for the numerical one. The accuracy, presented in Fig. 2.3, is very good.

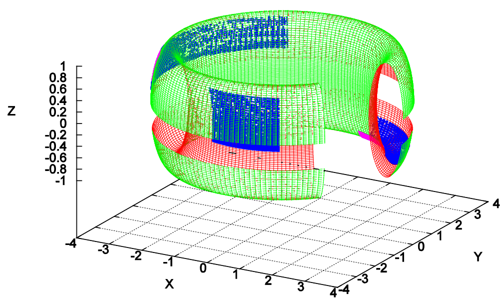

Figure 1.1 Tokamak wall with elliptical cross-section and three holes (in blue).

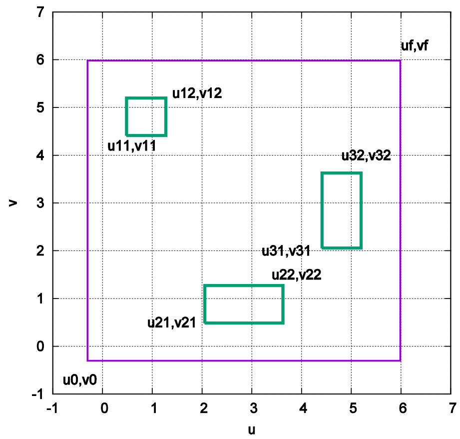

Figure 1.2 Multiply connected test domain D(u,v) between the four rectangles in a curvilinear coordinate system (u,v). It corresponds to a particular Cartesian wall representation like that given in Fig. 1.1.

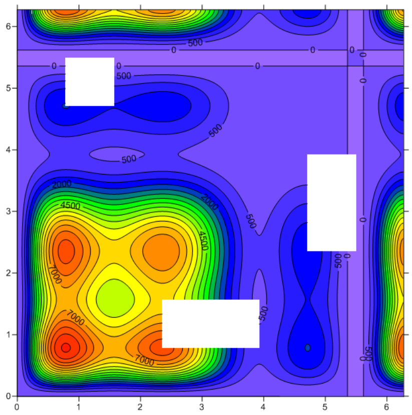

Figure 2.1 Constant analytical $\Phi^S(u,v)$, lines in the multiple connected domain (three holes – represented by white rectangles) given in Fig. 1.2

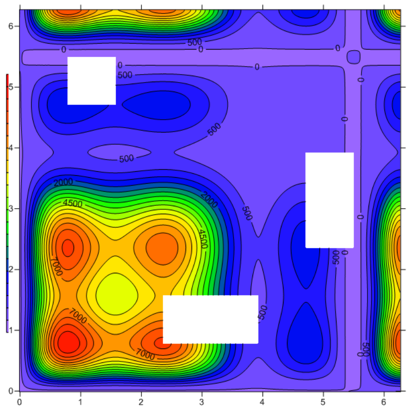

Figure 2.2 Constant numerical $\Phi^S(u,v)$, lines in the multiple connected domain (three holes– represented by white rectangles) given in Fig. 1.2.

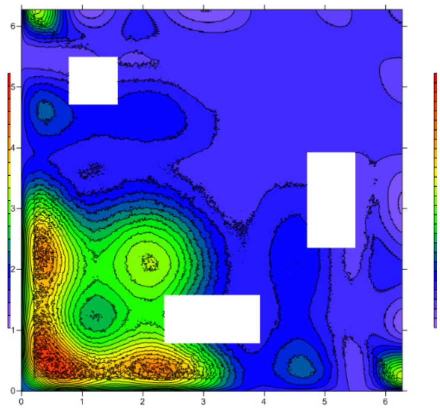

Figure 2.3 Relative error distribution between the analytical and numerical solutions.

Acknowledgement The reported work includes also contributions from the Theory Department of Princeton Plasma Physics Laboratory, USA (L.E. Zakharov) and the following people EUROfusion research unit: IPP Garching, Germany (K. Lackner, M. Hoelzl, E. Strumberger).

Numerical Stability in the Computation of the Reference Distribution Function for Charged Particles In Tokamak Plasma

Gyorgy Steinbrecher, Nicolae Pometescu

Faculty of Sciences, University of Craiova, Romania

WPCD-C

Reference distribution functions for the solution of the Fokker-Planck and gyrokinetic equations allows a first principle estimation of the performances of tokamak. In the previous works [1-4] it was established that it is possible to obtain reference distribution function by using the principle of maximal Shannon-Boltzmann-Gibbs entropy with scale invariant restrictions. In the work [5] we proved that there exists a generalization of the entropy introduced by A. Rényi. This new entropy (the Generalized Rényi Entropy) is extensive and has a H-theorem [5,6], so it is meaningful to extend the previous results by computing the distribution functions that maximizes the Generalized Rényi Entropy. The first problems that appears in this approach is related to the rigorous foundation of the corresponding approximation method. This problem was solved in the works [7,8, 9], that lead to the possibility to compute the solution of the following problem: find the particle distribution function in the space of invariants in the phase space, such that we have scale invariant linear restrictions and the generalized Rényi entropy is maximal. The class of solutions obtained [5,9,10] by this generalized maximal entropy problem contains in the simplest cases 11 free parameters [10]. These free parameters can be determined in the simplest approach by optimal fit with experimental or simulated data. The distribution functions from [1-4] appears as a limit case. While in the limiting case the distribution function has exponential decay, for the generic case the distribution function has polynomial decay at infinity, that better approximate the asymptotic domain in the turbulent plasmas [11]. The important fact is that there exists also a first principle approach, that reduces the problem of determination of the free parameters to the minimization of a nonlinear functional (called "objective function") constructed from family of reference distribution function and the underlying stationary Fokker-Planck equation. This is a particular case of the more general results on elliptic partial differential equations [12-13]. In both cases the main problem is the elaboration of numerically stable minimization of the objective function containing a large number of term. Previously, an improved version of the Marquardt algorithm was elaborated in FORTRAN90 programme and uploaded to the Gateway Garching Computing Centre: */pfs/home/gste/public/referencedistribution/wnlinleastsquare*

The following tests on the code was performed:

a) Because the algorithm require the computation of the numerical value of the objective function, its gradient and second derivative with respect to the free parameters in the optimal distribution function, we performed stability tests when the second derivatives are computed by numerical interpolation, using the analytic form of the gradient. The test was performed also under the condition that only 3 of the 11 free parameters are independent, because in this case it is possible to compute and to program the second derivatives by analytic methods. In this case the correctness of the test program with analytic form of the second derivative is easily verified. By this test the domain of the step size for finite difference calculations was studied. All of the test were performed on lattice of small dimension.

b) By using the previous results on the finite difference approximation of the second derivative, with analytic form of the gradients, numerical tests were performed for the case when also the gradient is approximated by finite difference interpolation. This test was performed also in small lattice. The domain of stability of the minimizing algorithm with respect to the finite difference step size was studied on synthetic data.

c) The stability of the numerical results was studied when the lattice spacing decreases. In the previous attempts to overcome the computational burden generated by this phenomenon, a stochastic optimization method was employed, in the spirit of the works [14, 15]. In the present test an efficient extrapolation method to the zero lattice spacing was successfully tested. It gives a better convergence compared to the previous stochastic optimization methods. Application of the mathematical methods elaborated in this work was applied to the study of to ITER scaling in [16].

References:

[1] G. Sonnino, G. Steinbrecher, A. Cardinali, A. Sonnino, and M. Tlidi, Family of probability distributions derived from maximal entropy principle with scale invariant restrictions, Phys. Rev. E 87 (2013) , 014104.

[2] G. Sonnino, A. Cardinali, G. Steinbrecher, P. Peeters, A. Sonnino, P. Nardone, Reference Distribution Functions for Magnetically Confined Plasmas from the Minimum Entropy Production Theorem and the MaxEnt Principle, subject to the Scale-Invariant Restrictions, Physics Letters A 377 (2013) 3061-3077.

[3] G. Sonnino, A. Cardinali, P. Peeters, and G. Steinbrecher, A. Sonnino, and P. Nardone, Derivation of reference distribution functions for Tokamak plasmas by statistical thermodynamics , Eur. Phys. J. D (2014) 68: 44.

[4] G. Sonnino, P. Peeters, A. Sonnino, P. Nardone and G. Steinbrecher, Stationary distribution functions for ohmic Tokamak-plasmas in the weak-collisional transport regime by MaxEnt principle. J. Plasma Physics (2015), 81(1), 905810116 .

[5] G. Sonnino, G. Steinbrecher, Generalized extensive entropies for studying dynamical systems in highly anisotropic phase space. Phys. Rev. E 89 (2014) 062106.

[6] G. Steinbrecher, G. Sonnino, Generalized Rényi Entropy and Structure Detection of Complex Dynamical Systems, arXiv:1512.06108v1 [physics.data-an](2015).

[7] G. Steinbrecher, A. Sonnino, G. Sonnino, Category theoretic properties of the A. Rényi and C.Tsallis entropies. Journal of Modern Physics, 7, 251-266, (2016), DOI: 10.4236/jmp.2016.72025, arXiv:1504.05552v3 [physics.data-an]

[8] G. Steinbrecher, G. Sonnino, Numerical Stability of Generalized Entropies, arXiv:1603.06240v3 [physics.data-an] (2016). Sent to publication.

[9] G. Sonnino, J. Evslin, A. Sonnino, G. Steinbrecher, and E. Tirapegui, Symmetry group and group representations associated with the thermodynamic covariance principle, Phys. Rev. E 94, 042103 – (2016)

[10] G. Steinbrecher, G. Sonnino, N. Pometescu, Maximal entropy distribution functions from generalized Rényi entropy, arXiv:1606.08730v3 [cond-mat.stat-mech] (2016). Sent to publication.

[11] G. Steinbrecher, B. Weyssow, "Generalized Randomly Amplified Linear System Driven by Gaussian Noise. Extreme Heavy Tail and Algebraic Correlation Decay in Plasma Turbulence", Physical Review Letters 92, 125003 (2004).

[12] A. Szilárd , A. R. Mészáros, Applied Mathematics and Computation, 229 (2014) 131–138.

[13] C. Mortici, T. M. Rassias, Soon-Mo Jung, Applied Mathematics Letters 40 (2015) 23–28.

[14] Kiefer, J. Wolfowitz, Annals of Math. Statistics 23, (1952), 462-466.

[15] J. N. Krejic, Z. Luzanin, I. Stojkovska, Appl. Num. Math. 70, (2013) 1-21.

[16] G. Sonnino, A. Sonnino, J. Evslin, G. Steinbrecher, Determination of the Dynamic ITER Energy Confinement Time Scalings, Journal of Modern Physics, vol. 7, No 12, (2016). DOI: 10.4236/jmp.2016.712130. arXiv:1412.5935v4 [physics.plasm-ph]

Dynamic Modelling of the Interaction Between External Perturbations and Neoclassical Toroidal Modes

Iulian Gabriel Miron

National Institute for Lasers, Plasma and Radiation Physics, Romania

WP-MST1-P

We have delivered a dynamic 3D quasi-analytic model to describe the neoclassical tearing modes (NTM) evolution under the effect of the external resonant magnetic perturbations (plasma column external coils generating RMPs) and/or adjacent non-resonant modes to the central perturbed NTM. Time dependent external magnetic perturbations (MP) are considered in order to measure its influence on NTMs evolution. The model is adapted to the ASDEX-Upgrade (AUG) case, considering the B-coils generating magnetic perturbations and having a sufficiently close realistic description of the experimental installation. A clear, analytic expression of the neoclassical perturbation calculated by solving the magnetic island resistive equations is delivered, linked by the matching conditions at the island-ideal plasma boundary with a general time dependent solution satisfying the perturbed equations outside the magnetic island, separately derived. The latter solution is compulsory to be derived because contains all information not only regarding the perturbed ideal plasma and the perturbed vacuum, but also concerning the plasma column AUG B-coils that basically provide the needed information about the MPs in discussion. Based on both solutions, the perturbation stability index is obtained to be used to solve the modified Rutherford equation of the magnetic island evolution. The stability index is also a measure of the influence of the RMPs on the NTM evolution, hence is has been point out the RMPs role as a trigger for the NTM onset and magnetic island seeding process. The RMPs effect on the mode increasing amplitude is shown along with the influence of the B-coils arrangements on the island width evolution. Despite the model limitations involving the consequences of being perturbative (therefore no saturation regime dynamic modelling is possible, due to the decaying normal plasma beta that is assumed constant in a perturbed model that requires static equilibrium quantities in order to be valid), good qualitative results are obtained regarding the RMPs/error fields effect on the NTMs during its linear and nonlinear regimes, even for experimental configurations difficult to be achieved. This work is part of the Working Programme Medium Sized Tokamaks (MST1) experimental campaigns we have participated in 2016: AUG15-1.4-3 "Interaction between resonant magnetic perturbations and NTM stability" and TCV15-1.4-4 "Advanced NTM physics".

Following the path of solving the magnetic island perturbed resistive equations shown in Hegna et al., *Phys. Plasmas* 6 (1999) 130, a 3D quasi-analytic *internal* solution has been found for NTM perturbations

$$\psi_s^{mn}(t) = -\frac{\mathrm{i}(m/q_s - n)}{\tau_{FKR}^{5/4}}\left\{\frac{A_s^{mn}}{\Gamma(9/4)}t^{5/4} - \frac{\mathrm{i}B_s^{mn}}{\Omega_{MP}}\left[\frac{t^{1/4}}{\Gamma(1/4)}\left(4+\exp(-\mathrm{i}\Omega_{MP}\mathrm{t})\,E_{3/4}(-\mathrm{i}\Omega_{MP}\mathrm{t})\right)\right.\right.$$
$$\left.\left. - \frac{\exp(-\mathrm{i}\Omega_{MP}\mathrm{t})}{(-\mathrm{i}\Omega_{MP})^{1/4}}\right] - \sum_{p=1}^{6L}\frac{C_{ps}^{mn}}{\tau_p}\left[\frac{t^{1/4}}{\Gamma(1/4)}\left(4+\exp(\tau_p t)\,E_{3/4}(\tau_p t)\right) - \frac{\exp(\tau_p t)}{\tau_p^{1/4}}\right]\right\} \quad (1)$$

that depends of the *external* solution of the perturbed equations in the ideal plasma/vacuum/resistive wall/AUG B-coils and/or generic feedback and detector coils, namely

$$\psi_{ext,s}^{mn}(t) = A_s^{mn} + B_s^{mn}\exp(-\mathrm{i}\Omega_{MP}\mathrm{t}) + \sum_{p=1}^{6L} C_{ps}^{mn}\exp(\tau_p t) \quad (2)$$

A_s^{mn}, B_s^{mn} and C_{ps}^{mn} are exactly derived coefficients involving the perturbative physics everywhere except the magnetic island, q_s is the safety factor at the magnetic surface of the radial coordinate r_s and Ω_{MP} is the toroidal angular velocity of the rotating magnetic perturbations spectrum generated by the ASDEX-Upgrade (AUG) tokamak B-coils. τ_{FKR} is the linear tearing mode diffusion time $\tau_{FKR} = (\tau_r^{3/5}\tau_a^{2/5}/m^{6/5})[\pi\Gamma(3/4)/\Gamma(1/4)]^{4/5}$ where τ_r and τ_a are the resistive and the Alfven time, respectively. Γ and $E_{3/4}$ are the gamma and the integral exponential functions. τ_p are the roots of $D_s(\tau_p) = 0$ equation, where $p = 1,..,6L$, with $L = (m_2 - m_1 + 1)(n_2 - n_1 + 1)$ (see Miron, Plasma Phys. Controlled Fusion 50 (2008) 095003), the poloidal m and toroidal mode n spanning $m_1 \le m \le m_2$ and $n_1 \le n \le n_2$. D_s is the quasi-analytically calculated determinant of the Fourier and Laplace transformed linearized system of *external* equations.

To estimate the influence of the neighbouring modes to the central NTM, in Fig.1 is drawn the evolution of the (2,1) NTM in the presence of more positive and more negative adjacent poloidal modes. It is clear that the coupling of the (2,1) mode with the more negative poloidal adjacent mode is stronger than the coupling with the more negative neighbouring mode. A similar behaviour is retrieved in the (3,2) NTM mode, shown in Fig. 2. Clearly the non-resonant coupling with a mode that develops deeper in the bulk of the plasma is more destabilizing for the NTM.

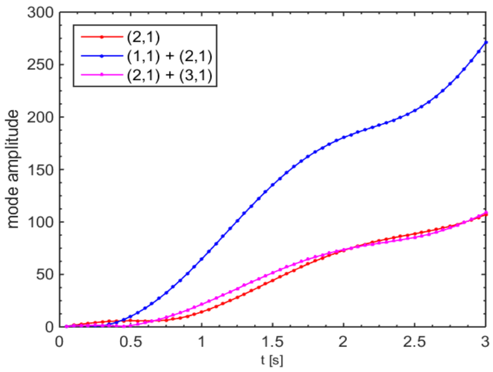

Figure 1: Evolution of *(2,1) central mode under the influence of the neighboring poloidal modes.*

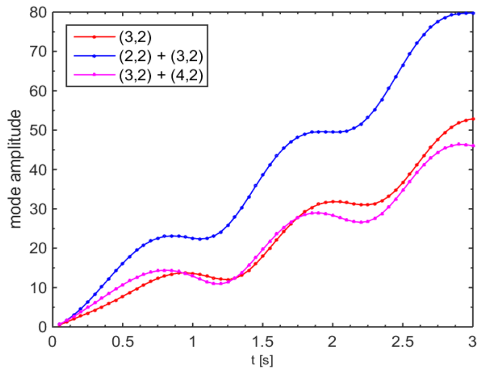

Figure 2: (3,2) NTM evolution in the presence of neighboring poloidal modes

On the other hand, for the resonant coupling case, the (2,1) NTM mode amplitude is plotted in Fig. 3 for various arrangements of the AUG B-coils. The NTM amplitude has a maximum for a toroidal phase difference between the upper and the lower B-coils rows of approx. $\Delta\phi \cong 110^o$. Remember that the effect of the amplitude of the perturbation excited by the resonant effect is not necessarily retrieved into the value of the width of the corresponding magnetic island. To evaluate the island width, the growth rate of the perturbation is a more significant quantity. A more or less different behaviour of the island is expected compared to the perturbation evolution - a conclusion also pointed out during the MST1 experimental campaigns. A similar dependence is drawn for the (3,2) mode in Fig. 4. The phase shift $\Delta\phi \cong 45^o$ maximizes the mode resonant amplitude. Adequate current distributions arrangements are used to make the resonance possible for each mode.

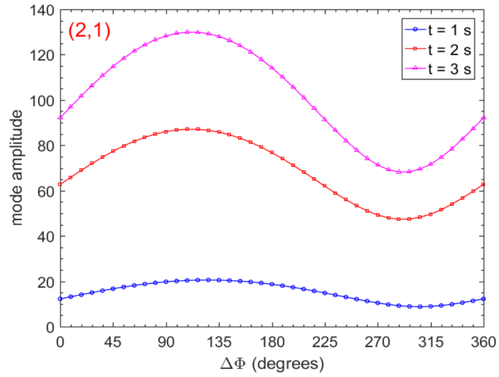

Figure 3: Calculated normalized (2,1) NTM amplitude vs toroidal phasing $\Delta\phi$ at t = 1s, 2s and 3s, respectively.

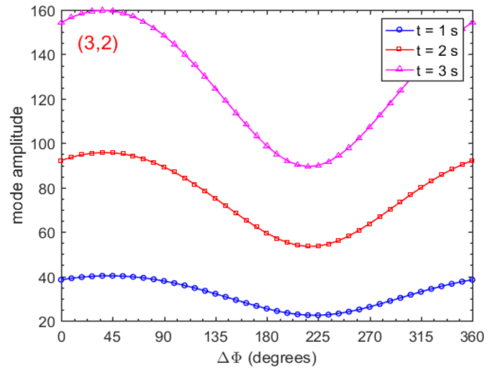

Figure 4: Normalized (3,2) NTM amplitude vs. $\Delta\phi$ of the coil currents at t = 1s, 2s and 3s.

To resume, a 3D model is developed in order to find a solution that simply depicts the information about the MP-NTM interaction in a quasi-analytic approach. Moreover, the approach is also time dependent, hence the dynamics of the mentioned interaction is explicitly shown.

The Magnetic Perturbations Effect on the Onset of the Neoclassical Tearing Modes

Iulian Gabriel Miron

National Institute for Lasers, Plasma and Radiation Physics, Romania

WP-MST1

The dynamics of the magnetic island is shown based on a quasi-analytic model that calculates the 3D perturbations spectrum inside and outside the magnetic island. The calculations are performed for the case of an ASDEX-Upgrade plasma surrounded by an inhomogeneous resistive wall in the presence of a spectrum of magnetic perturbations (MP) generated by a set of in-vessel saddle coils (B-coils). Flux coordinates of Hamada type are used. The obtained solution satisfying the perturbed resistive momentum equations and the generalized Ohm's law inside the magnetic island is found using the Laplace transform of the matching condition between the island and the ideal regions of plasma. The inner solution relies on the outer solution we have derived by solving the ideal plasma region perturbed momentum equations, the circuit equations in the plasma column external structures and the perturbed vacuum equations. The delta prime stability index measuring the perturbation jump across the island is analytically found. The modelling being a dynamic one, the evolution of the magnetic island is shown by solving the modified Rutherford equation. The analytic treatment considers a multimode approach in order to calculate the non-resonant contributions. The insertion of the AUG B-coils provides a resonant/non-resonant MP to interact with the neoclassical tearing mode (NTM). The influence of the former on the island evolution is calculated and accurately drawn. Moreover, regarding the resonant case, the phase shift between the upper and lower B-coils rows is derived in order to find the maximum possible resonance between NTM and corresponding MP to be avoided for different coils current arrangements. This aspect seems to be of a specific importance according to last AUG MST1 experimental campaign.

According to our notations, the tearing stability index for the magnetic island disposed at a radial flux coordinate r_s is given by $\Delta_s{}'(t) = -(2m)/r_s \left(\psi_{ext,s}^{mn}/\psi_s^{mn}\right)$, where ψ_s^{mn} is the 3D quasi-analytic calculated *internal* solution (basically the NTM) and $\psi_{ext,s}^{mn}$ the *external* solution of the perturbed equations in the ideal plasma/vacuum/resistive wall/AUG B-coils and/or generic feedback and detector coils (see the principal project). By solving the modified Rutherford equation, Figure 1 shows the (2,1) island width evolution drawn in the presence and absence of the bootstrap term. $\Delta_s{}'(t)$ exhibits an explicit sensitivity to RMPs and its effect is especially felt at the NTM onset stage, as it is clearly shown in figure. Although the influence of $\Delta_s{}'$ seems to be low compare to the bootstrap term, at least until $t \approx 2\ s$, the Δ_s' effect prevails, indicating that RMPs could play the role of a trigger for the NTMs onset. The $\Delta_s' + BS$ plot has an inflexion point at 2 s, the starting time for a robust growth of the island width.

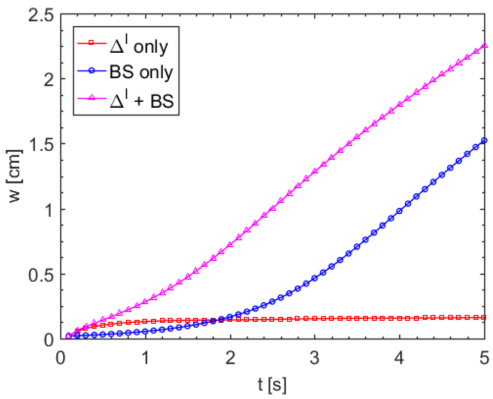

Figure 1 – Island evolution considering the stability index or bootstrap term only and in the presence of both terms.

The island evolution for different phase differences $\Delta\phi$ between the upper and the lower B-coils rows is drawn in Fig. 2. In order the RMP effect to be more visible, term stability index has been considered only. The upper and lower B-coils operates with AC currents having the frequency of 0.5 Hz and a maximum of coil current of $I_{MP,peak} = 1\ kA$. The current scheme for every coil of both rows is shown above the island evolution plots in the figure. The $\Delta\phi \cong 0$ phasing seems to correspond to the more sensible (2,1) NTM island width to the RMP influence. A higher B-coils current corresponds to a more significant NTM destabilization for the $\Delta\phi \cong 0$ case, as usually expected. But for different phasing values from the optimal one, a higher RMP does not necessarily leads to a more unstable NTM.

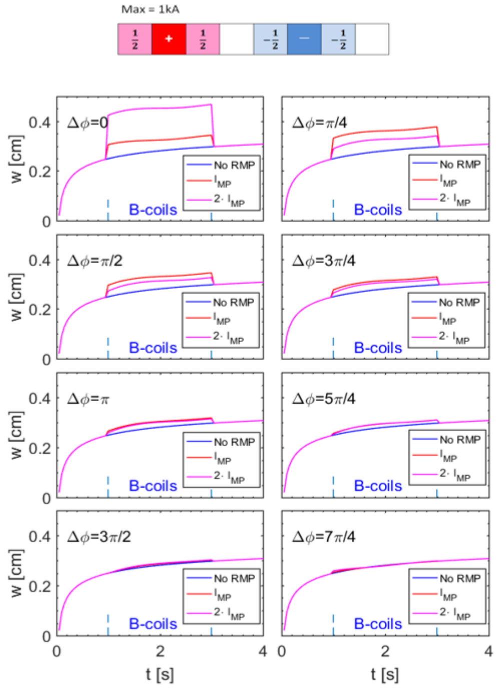

Figure 2 – Island evolution for different phase differences $\Delta\phi$ at zero, I_{MP} and $2I_{MP}$ B-coils currents. RMP is switched on for $1.5\ s \leq t \leq 2.5\ s$. $I_{MP,peak} = 1\ kA$. (no bootstrap term considered)

It appears that when the resonance conditions are not optimal, a higher RMP amplitude could be less destabilizing. Figures 3 and 4 show the island evolution in the single mode case along with the cases when non-resonant adjacent poloidal modes are considered. Whereas for the (2,1) island the both more negative and more positive neighbouring modes destabilize the central mode (Fig. 2), for the (3,2) island the more negative neighbouring mode has a more destabilizing effect (Fig. 3).

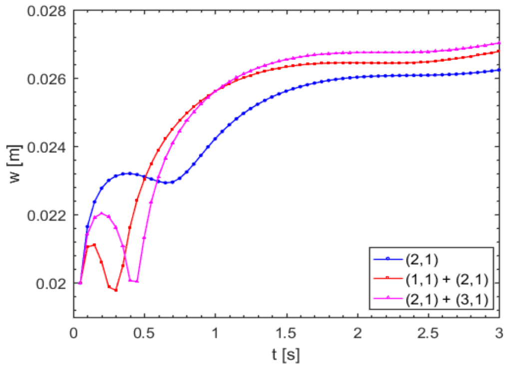

Figure 3 - The effect of the neighboring poloidal modes to the (2,1) island width dynamics.

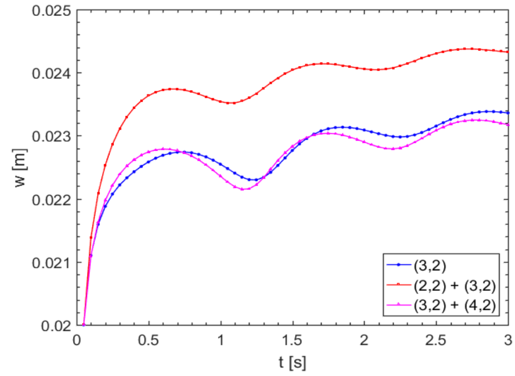

Figure 4 - (3,2) island evolution in the presence of neighboring poloidal modes.

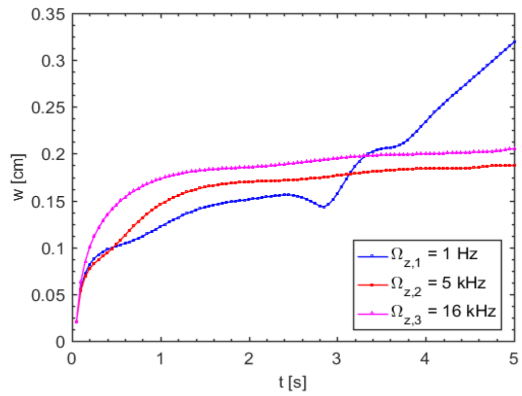

Figure 5 – Island width vs. time at different plasma toroidal angular rotation rates.

A significant island width damping could be seen at early times for the case of the (2,1) mode when the neighboring perturbations are considered. It seems that the adjacent modes abruptly decreases the central mode growth rate and subsequently the tearing stability index to negative values within the mentioned early period of time. Afterwards the island retrieves its constant increase indicating that the corresponding mode growth rate becomes at least constant, if not positive.

A similar analysis performed in the toroidal case proves that the adjacent toroidal modes have a significantly lower influence on the central unstable mode compared to the poloidal neighboring modes. The more positive neighboring mode seems to have almost no influence. The fact that the B-coils are evenly spaced in the toroidal direction (8 coils) couples the (m, n) with the $(m, n + 8 \cdot \propto)$ only, for any integer $\propto$, in the absence of any other toroidal inhomogeneity (see R. Fitzpatrick and E.P. Yu, *Phys. Plasmas* 5 (1998) 2340).

The validity of the perturbative model (from a static equilibrium state) assumes a constant local plasma toroidal rotation to be kept. However different evolutions corresponding to different toroidal rotation rates can be compared. Usually high toroidal rotations play a stabilizing role by not allowing an abrupt increase of the island width. In Fig. 5 a low plasma toroidal rotation becomes insufficient in order to maintain a reasonable growth of the island: from a specific moment of time, the island grows in an abrupt way – the dynamic plot matches the model: the exponential term of the derived solutions ψ_s^{mn} and $\psi_{ext,s}^{mn}$, whose argument is linearly dependent of time, becomes early asymptotic.

Electromagnetic Torques Calculations in the Presence of the Resonant External Magnetic Perturbations

Iulian Gabriel Miron

National Institute for Lasers, Plasma and Radiation Physics, Romania

WP-MST1-C

The assessment of whether the electromagnetic (EM) torque or the neoclassical toroidal viscosity torque (NTV) mechanism prevails regarding the destabilizing effect on the NTM stability is another subject of the project. The former torque is induced by the resonant coupling between NTM and the external AUG B-coils generating resonant magnetic perturbations (RMP), whereas the latter is due to the non-resonant external perturbations effect on the plasma as a consequence of the magnetic field symmetry breaking induced by the presence of the NTM itself. A clarification is required regarding the prevalence among the above mentioned two effects on the NTM stability and dynamics because of recent measurements performed at AUG (S. Fietz et al., *Nucl. Fusion* 55 (2015) 013018) showing that the main responsible for the global plasma toroidal rotation damping are the EM torques developing at levels of multiple magnetic surfaces as a result of the resonant coupling mechanism. On the other hand, previous theoretical studies (such as W. Zhu et al., *Phys. Rev. Letters* 96 (2006) 225002) claim the opposite, i.e. the NTV torque is the main drive factor for the damping of the plasma rotation and the NTM stability degradation. A way to discern each torque peculiar contribution is to accurately calculate both torques quantities within the frame of a common model (unlike using different modelling approaches, as usually happens) in order to finally compare the measured results of their collected contributions. At least the same (fluid and kinetic) modelling using a commonly derived NTM amplitude and phase to calculate both braking torques seems to be a condition to obtain results in an appropriate manner. The kinetically derived divergence of the traceless pressure tensor is used into the equations (a perturbed particles distribution function is previously obtained) in order to obtain the NTV contribution.

The EM torque developing at a specific (m, n) magnetic island location is calculated as the imaginary part of the expression below, in $O(\varepsilon)$ approximation

$$T_{EM,z} = -\frac{4\pi m r_s^2}{\mu_0 R_0^4}\, Im\{\, \mathrm{i}[\, 1 + \log r_s + O(\varepsilon)]\psi_s^{mn*}\psi_{ext,s}^{mn}\}$$

a and R_0 are the minor and the major radius of the plasma, respectively (ε is the inverse aspect ratio). r_s is the radial coordinate where the (m, n) magnetic island is located at. $\psi_{ext,s}^{mn}$ is the *external* flux perturbation, namely the solution of the perturbed equations everywhere outside the magnetic island, i.e. ideal plasma/vacuum/resistive wall/AUG B-coils and/or generic feedback and detector coils (used strategy: Fourier development, Laplace transformation, Laplace transformed equations solving via the partial fraction decomposition, inverse Laplace transformation). In terms of perturbed quantities calculated *outside* the magnetic island, the EM torque is proportional to the imaginary part of the scalar product between the conjugate of the flux perturbation and the above mentioned radial jump of the perturbation. This *external* approach has been widely used within the scientific literature to calculate the EM torque developed at the level of any type of inertial layer in the plasma. But this kind of treatment does not provide an EM torque that experiences the magnetic island or the NTM physics itself. Therefore, we have calculated the stability index (i.e. the jump of the radial derivative across the island) using the *internal* perturbation ψ_s^{mn} by solving the perturbed resistive magnetic island equations. But whereas in Hegna et al., (Phys. Plasmas 6 (1999) 130) the *internal* solution matches an *external* test function at the magnetic island-ideal plasma boundary, in our case the *external* solution is a robustly calculated perturbation that satisfies the outside magnetic island equations, thus enclosing all the information regarding the ideal plasma and the plasma column resistive external structures. The symbols * and ' mean complex conjugation and radial derivative, respectively.

In the Figs. 1-2 the above EM torque evolution is tested, based on the calculated perturbed solutions $\psi_{ext,s}^{mn}$ and ψ_s^{mn} for the ASDEX-Upgrade case. The torque is calculated at the level of the magnetic island where a (2,1) NTM develops, described by the perturbed flux function ψ_s^{mn}. The B-coils have a maximum current of $I_{MP,peak} = 1\ kA$ for 0.5 Hz frequency. The current scheme for every coil of both rows is shown above the torque evolution plots in the figure. The normalized EM torque (to the highest value of all the calculated torques in the figure) evolution is drawn for different phase differences $\Delta\phi$ between the upper and the lower row of coils. By varying $\Delta\phi$, the alignment of the external magnetic field with the plasma varies, and hence the resonance degree between the RMP and NTM. An expected behaviour is obtained as the coil current is increased, although for certain values of $\Delta\phi$ the current intensity seems to only slightly augment the torque magnitude. There are obviously the same values corresponding to the weakest resonance among the plasma and external perturbations. A higher RMP coils current corresponds to a more robust and oscillatory EM torque.

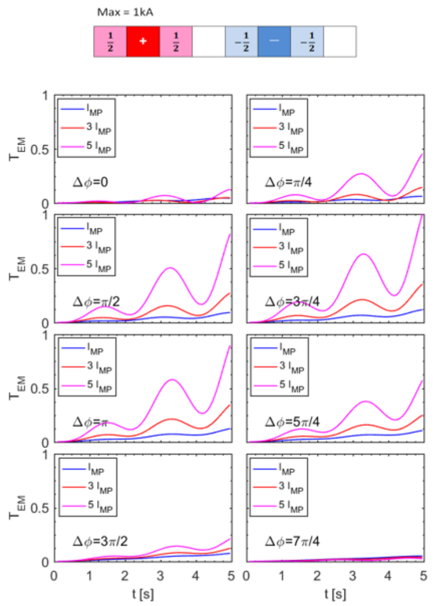

Figure 1 – Normalized (2,1) EM torque evolution for different phase differences $\Delta\phi$ at I_{MP}, $3I_{MP}$ and $5I_{MP}$ B-coils currents.

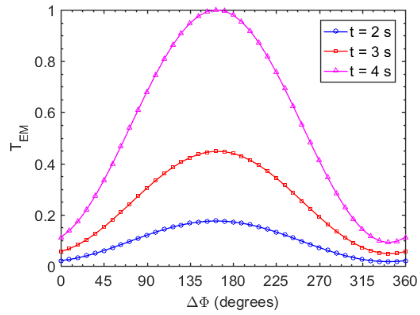

Figure 2 - Calculated normalized (2,1) EM torque vs. the toroidal phasing $\Delta\phi$ of the coil currents at t = 2s, 3s and 4s, respectively. $I_{MP,peak} = 1\ kA$.

At least for our parametric choice, a toroidal shift of $\Delta\phi$ between $3\pi/4$ and π corresponds to maximum resonance. More precisely, Figure 2 drawn at different moments of time shows that $\Delta\phi$ of about 160 degrees corresponds to the highest resonance. There is no direct link among the RMP influence on the NTM amplitude vs corresponding EM torque due to the additional influence of the external solution $\psi_{ext,s}^{mn}$ (see the principal project phase shift dependence). A similar analysis has been made for the (3,2) NTM. The current scheme is different compared to the (2,1) case, in order the corresponding RMP to resonate with the (3,2) mode.

This time a toroidal shift $\Delta\phi$ between $\pi/2$ and $3\pi/4$ maximizes the resonance and hence the EM torque amplitude. However, the B-coils phase shift induces a more complicated dependence between the B-coils current amplitude and the resonance strength. As in the (2,1) case, despite the maximum possible resonance occurring at a common phase shift, the relation between EM torque and the B-coils perturbed current amplitude is not proportional: for particular values of $\Delta\phi$, a higher perturbed current could be a more stabilizing choice, as unexpected ($\Delta\phi = 0, 5\pi/4, 3\pi/2, 7\pi/4$ for the (3,2) case, for instance). A higher oscillatory behaviour remains attached to a higher current, even the latter is less destabilizing. But the maximum possible resonance corresponds to a phase shift for which a highest perturbed coils current is a more destabilizing one.

We have delivered a clear, quasi-analytic expression for the electromagnetic torque developing as a magnetic island forms and the NTM and external RMPs interact. The EM torque magnitude evolution could be followed due to the time dependent calculations. A whole spectrum of parametric situations could be tested in order to find the optimal stability scheme. Our model could be a handy tool to test the resonance effect on plasma perturbations. This is a first step in order to further clarify whether the EM or the NTV effect on NTMs prevails. The second type of braking torque to be calculated is the subject of a further approach.

Romanian Participation at JET Experimental Campaigns

T. Craciunescu[1], M. Vlad[1], F. Spineanu[1]

[1]*National Institute for Lasers, Plasma and Radiation Physics, Bucharest-Magurele, Romania*

WP-JET1-P

The JET campaigns in 2016 had the essential task of providing a clear understanding of the plasma behavior in regimes that preced the future Tritium-Deuterium experiments.

The deuterium campaign C36 and C36b focus have been centred on ITER scenario development with the ITER like Wall with up to 34 MW of NBI power (deuterium) and 10 MW of ICRH. The development of operational scenarios based on the conventional and hybrid ELMy H-mode aimed at maximum fusion power in a D-T experiment in stationary conditions (≈5s). Together with the scenario development, a strong focus addressed urgent ITER needs as highlighted in the ITER research plan, and for developing a sound physics basis for the extrapolation through first principles and integrated modelling of JET results to ITER and DEMO. In addition to the deuterium campaign a hydrogen campaign (C37) has been scheduled before the start of the 2016 shutdown. The main aim of this campaign was to provide unique data with the ITER-Like Wall of the isotope effects on transport, confinement L-H transition and pedestal physics by a full exploration of the future H, T and DT-campaigns.

The participation of the Romanian group of experts to the experiments and analysis of JET C36, C36b and C37 experimental campaigns is related to the following experiments: M15-01: Baseline scenario for DT, M15-02: Hybrid scenario for DT, M15-19 - Mitigation of runaway with high Z, M15-24 - Target discharge for TAEs in DTE2 and fast particle physics in all scenarios, B15-12: H D He3 ICRH scenario test and H16-12 - Three-ion ICRF scenario development.

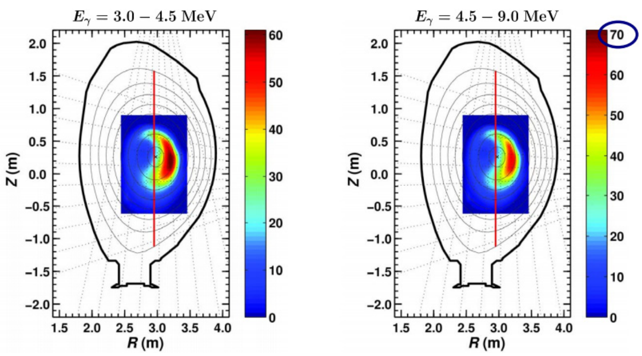

Figure 1 – Gamma-ray emissivity profile for the JET pulse #90752 (PRF = 4.2MW (dipole), H/H+D ~ 0.83-0.74, X[3He] ~ 0.2-0.3%) with a very good steady-state and with dipole phasing [Khazakov et al, submitted to Physical Review Letters].

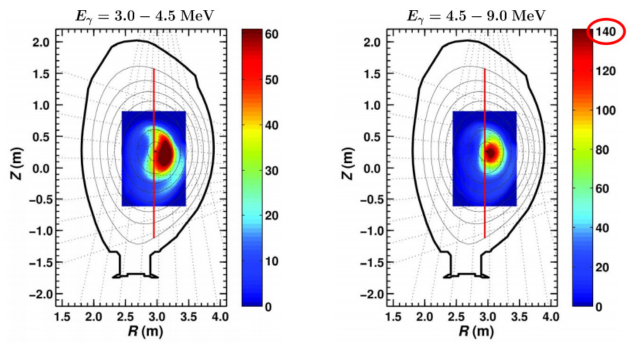

Figure 2 – Gamma-ray emissivity profile for the JET pulse #90753 (PRF = 4.2MW (mixed phasing), H/H+D ~ 0.83-0.76, X[3He] ~ 0.2-0.3%) with the largest rate of high-energy gammas (mixed ICRF phasing, but the optimal H-D mixture) [Khazakov et al, submitted to Physical Review Letters].

Tomography analysis, based on the Maximum Likelihod (ML) method developed for the JET neutron camera (KN3) has been provided for different experiments. Gamma emission tomography has been provided for the experiment B15-12 and H16-12 in order to retrieve the spatial distribution of fast ions population. An illustrative example is presented in Figs. 1-2.

Neutron tomography has been applied for analysing different interesting cases from the M15-24 experiment. A typical example is presented in Fig. 3.

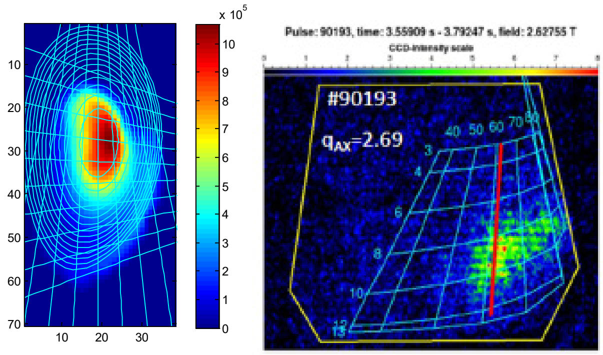

Figure 3 – The 2D neutron distribution for JET pulse #90193 (left) has been reconstructed for the time interval when the KA3 scintillator foot prints, during the NBI phase, shows a broader FP losses at elevated q0 (right).

Hard X-ray tomographic analysis has been performed for the study of the runaway electrons "in flight" before their interaction with the plasma facing components using time, spatial and energy resolved measurements of bremsstrahlung originated in interaction of fast electrons with bulk plasma, gas puff or injected pellet.

The tomographic reconstruction of the measured HXR emissions provides detailed data on temporal evolution and spatial structure of RE beams during disruptions.

The main difficulty of this kind of tomography is related to the necessity of performing the analysis for data acquired close to disruption.

The tomographic reconstruction method uses the magnetic profiles as an additional term in the objective function in order to supply the ill-posed character of the tomographic problem in case of JET KN3 system. In the vicinity of the disruption the magnetic profiles vary abruptly during a very short time interval (of the order of a few tens of ms). Therefore the use of standard magnetic data would lead to distorted reconstructions and to wrong physical interpretation. Therefore it was necessary to couple the tomographic software with the EFIT++ equilibrium code which can provide a temporal resolution of 10 ms.

The study of the correlation between the oscillations of D-alpha emission and the neutral atom influx at the edge

We advance a hypothesis on the physical mechanism which is behind the oscillation of the D-alpha emmission. In our perspective, the oscillation is due to a periodic improvement of the rotation in the edge layer, reducing the recycling fluxes. The short time events consisting of massive ionization frequently have a positive effect on the quality of confinement. This is because every new ion created by ionization (at gas puff, pellet or impurity seeding) produces a radial current and the ensemble of these currents (for the large number of ionizations of neutrals) is a radial current able to create a torque and sustain poloidal and toroidal rotation. We have calculated the radial current for an assumed influx of neutrals that corresponds to a pellet. It resulted that the torque is higher than the Transit Time Magnetic Pumping (TTMP) damping rate, calculated according to neoclassical kinetic equation.

The set of computer codes we have written to study quantitatively this effect is able to calculate the radial current generated over a mesh of points covering the region of ionization. The exact particle orbits are used in every cell, ensuring that we dispose of the accurate contribution. Two formulas (derived analytically) are compared with the direct numerical calculation and the values are very close. We have proven that the radial current associated to the elementary ionization event is a geometrical effect and cannot be suppressed by collisions. It happens that if not the initial ion, then there will be another ion that, due to collisions, will carry out the radial displacement, since this connects two states of statistical equilibrium.

The mechansim for the oscillations of the D-alpha emmision may be connected with the radial current, torque and poloidal rotation that are produced by ionization of the neutrals penetrating from the edge. An influx of neutrals penetrate into plasma (from SOL) as part of a usual recycling of density at the edge. The neutrals are ionized (with D-alpha emission) and heated but, simultaneously, they are moving to neoclassical orbits. The first transient part of this motion, just after ionization, is an effective radial current leading (for all the ensemble of new ions) to poloidal torque and rotation. This effect is short and of substantial amplitude, as we have found in numerical simulation described above. The edge plasma begins to rotate and this will necessarily be a sheared rotation. The consequence of the sheared rotation should be placed in parallel with the H-mode rotation in the this edge layer. There is a barrier of transport which is formed. Then the density loss will be reduced, as happens in the pure H-mode case. The decrease of the loss of ions is a corresponding reduction of D-alpha. Now, however, the radial current of the new ions is transient and takes a very short period of time if the flux is spontaneous (i.e. not pellet, etc.). Then the torque is exhausted and the rotation is damped by TTMP. The decay of rotation makes possible a new outflux of ions from plasma, followed by a recycling from SOL, neutrals' ionization and rise of D-alpha, rotation and drop of edge loss (and of D-alpha emission), etc. This is a cyclic process.

W transport and accumulation

M. Vlad[1], F. Spineanu[1]

[1]*National Institute for Lasers, Plasma and Radiation Physics, Bucharest-Magurele, Romania*

WP-JET1-C

The first stage of the study consists of the evaluation of the effects of the polarization drift. This is expected to provide an important contribution to heavy ion transport since it is proportional with the mass of the particle. A complex model was developed for the study of the polarization drift effects. It includes the ExB drift, the polarization drift, the parallel motion, the diamagnetic velocity and the magnetic drifts. The turbulence is described as a Gaussian field with a spectrum that is similar to the experimental results. We have developed a Fortran code based on the semi-analytical method, the fast-DTM [Vlad, Spineanu, Phys. Plasmas 22 112305 (2015)]. It determines the transport properties of the heavy impurity ions.

The transport essentially depends on three dimensionless parameters

$$K_*^{'} \equiv \frac{e\Phi}{T_i}\frac{a}{\rho_i}, \;\; C_A = \frac{A}{2Q}\frac{\rho_i}{a}, \;\; V_m = \frac{2}{3Q}.$$

The measure of turbulence amplitude φ is $K_*^{'}$, the parameter of the polarization drift is C_A and V_m is the normalized magnetic drift. The notations are T_i for the temperature of the plasma ions, Q for the ionization rate of the impurities, A for their mass number, ρ_i for the Larmor radius of the protons and a for the minor radius of the plasma. The characteristic values of C_A for W impurities are two orders of magnitude larger than for plasma ions. They are in the range $[0.1,\ 0.4]$, depending on plasma size a.

The time dependent diffusion coefficient $D_x(t)$ was determined for these dimensionless parameters, also considering a decorrelation mechanism that can be produced by the time variation of the potential or by the parallel motion. The latter leads to the saturation of $D_x(t)$ at times of the order of the decorrelation time τ_d.

We have found that in the quasi-linear regime (with $K_*^{'} < 1$), the polarization drift has negligible influence on the transport of the W impurities. As seen in the example presented in Figure 1, the blue curve for C_A=0.2 is superposed on the black curve obtained with zero polarization velocity. The magnetic drift, which enhances the average velocity, determine a significant decrease of the asymptotic diffusion coefficient (see the red curve in Figure 1). The reason is the displacement of the maximum of $D_x(t)$ toward smaller time, which contributes to the increase of the interval between the decorrelation time and the maximum. The asymptotic diffusion coefficient is a decreasing function of this interval.

The polarization drift influences the transport only in the nonlinear regime characterised by trajectory trapping. Figure 2 presents the radial diffusion coefficient for the same parameters as in Figure 1, except the value of $K_*^{'}$, which is 5. The increase of the asymptotic diffusion coefficient can be seen comparing the black curve for C_A=0 and the blue curve for C_A=0.2. The diffusion increases as C_A increases, it reaches a maximum for C_A=0.3 and eventually decays. The maximum increase of D_x is by a factor of the order 2. The magnetic drift has a much smaller effect in this case compared to the quasi-linear regime. As seen in Figure 2, the change of V_m from zero (blue curve) to 0.5 (red curve) determines only a small decrease of the diffusion coefficient.

Besides the significant increase of the diffusion coefficient, the polarization drift generates an average radial velocity. The effect appears only in the presence of trapping. As seen in Figure 3, the radial velocity depends on the decorrelation time τ_d. It increases with the increase of the polarization drift parameter and saturates at CA>0.4.

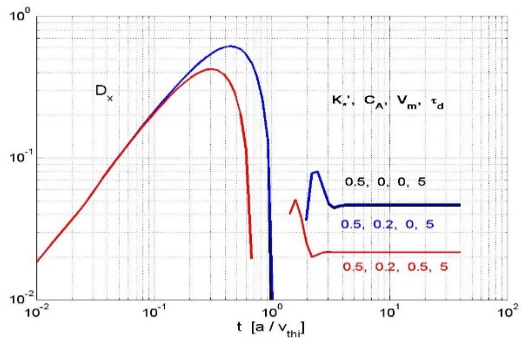

Figure 1 – Effects of the polarization drift and of the magnetic drift in the quasi-linear transport. The time dependent diffusion coefficient $D_x(t)$ for the values of the parameters $K_*^{'}$, C_A, V_m and τ_d that label the curves

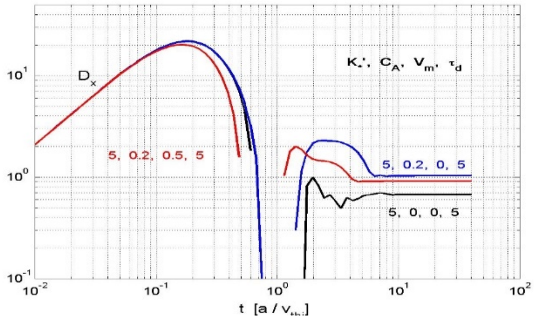

Figure 2 – Effects of the polarization drift and of the magnetic drift in the nonlinear transport. The time dependent diffusion coefficient $D_x(t)$ for the values of the parameters $K_*^{'}$, C_A, V_m and τ_d that label the curves.

We have shown that the polarization drift determines complex nonlinear effects that consist of significant increase of the diffusion coefficient (up to factors of the order 2) and in the generation of an average radial drift. The condition for the occurrence of these effect is the presence of trajectory trapping or eddying that correspond to nonlinear transport. In the quasi-linear transport, the influence of the polarization drift velocity is negligible even at the very large mass of the W ions.

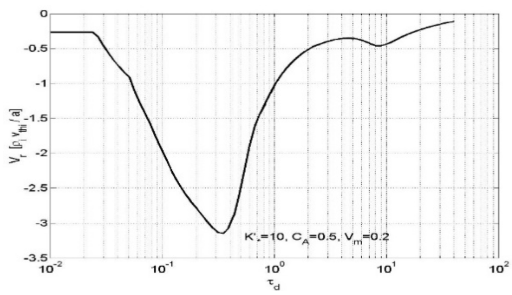

Figure 3 – The average radial velocity generated by the polarization drift as function of the decorrelation time

The assessment of the importance of the polarization drift for W ions is related to the type of transport. We have developed a complex study with the aim of understanding this fundamental problem [2]. The first results show that drift turbulence evolution can lead both to quasi-linear and nonlinear transport regimes, depending essentially on the drive parameter. The heavy impurity transport will be analysed in the next period in non-Gaussian turbulence using the model developed in [3].

Asessment of the Efficiency of Synchronization Experiments in Tokamaks by Time Series Syncronization and Causality

T. Craciunescu[1], A. Murari[2,3], E. Peluso[4], M. Gelfusa[4]

[1] *National Institute for Laser, Plasma and Radiation Physics, Magurele-Bucharest, Romania*

[2]*Consorzio RFX (CNR, ENEA, INFN, Universita' di Padova, Acciaierie Venete SpA), Corso Stati Uniti 4, 35127 Padova, Italy*

[3]*EUROfusion Programme Management Unit*

[4]*University of Rome "Tor Vergata", Via del Politecnico 1, 00133 Rome, Italy*

WP-JET1-C

Control of instabilities such as ELMs and sawteeth is considered an important ingredient in the development of reactor relevant scenarios. Various forms of ELM pacing have been tried in the past to influence their behaviour using external perturbations. One of the main issues of these synchronization experiments resides in the fact that ELMs are quasi periodic in nature and therefore, after any pulsed perturbation, if enough time is allowed to elapse, an ELM always occurs. To evaluate the effectiveness of ELM pacing techniques, it is therefore essential to determine an appropriate interval over which they can really have a triggering capability.

ELMs are instabilities that almost invariantly affect H mode plasmas, causing a reduction of the energy confinement through deterioration of the edge transport barrier. This sudden degradation of the confinement at the edge induces an expulsion of energy and matter from the plasma on a sub millisecond time scale, which can result in unacceptable erosion of the plasma facing components in the divertor. Irrespective of their dynamic nature, in the perspective of ITER and DEMO it is imperative to control ELMs carefully, to alleviate their detrimental effects on the plasma facing components in the divertor. Indeed, DEMO will probably have to be operated in ELM-free scenarios. On ITER, some form active ELM control is also considered essential. Therefore, to support the development of reactor relevant scenarios, in many machines various forms of ELM pacing techniques have been tested. This subject assumes a particular relevant role in the present programme of JET with an ITER Like Wall (ILW) on the route to the next full DT campaign. One of the most promising applications is pacing of ELMs with pellets. The long term aim of this approach would consist of being able to trigger ELMs with pellets, whose frequency could be adjusted so that the gradients at the edge would not increase, between two subsequent ELMs, to the point of causing excessive expulsion of energy and matter, capable of damaging the plasma facing components. These pacing experiments are typical cases of synchronization techniques.

One of the main difficulties in developing such experimental solutions reside in the interpretation of the experimental results. This is due to the fact that ELMs are quasi periodic in nature and therefore, after any sudden perturbation such a pellet, if enough time is allowed to elapse, an ELM always occurs. To evaluate the effectiveness of the triggering, it is therefore essential to determine a reasonable time over which pellets can really have a triggering capability. This is equivalent to determining the time interval over which pellets can have a causal influence on the ELM dynamics. The difficulty of the problem can be appreciated by inspection of Figure 1, which reports the D_{α} for ELMs and pellets in a JET discharge with the ITER Like Wall (ILW). It is evident how the task of determining how many pellets have triggered an ELM is quite challenging, given the limited diagnostic information and the high level of noise in the measurements. This is the typical problem of assessing causality relations between different events in a probabilistic framework.

In this work a method to determine causality between external perturbations and ELMs is introduced. The method is a typical one for nonlinear dynamical studies and it is based on Recurrence Plots (RP). Indeed, the recurrence behaviour is a fundamental characteristic of dynamical systems. RPs are very powerful tools for the descriptive studies of the statistical properties of dynamical systems - RP is a plot showing the times at which a phase space trajectory visits roughly the same area in the phase space. Joint Recurrence Plots (JRP) can be used to relate the behaviour of one signal with the one of another. By quantifying the properties of JRP through Recurrence Quantification Analysis (RQA), it is possible to determine the maximum interval of information transfer between two time series. Of particular relevance for the subject of this work is the fact that RQA provides several measures, which can be related to the causal relation between signals: i) Average of Diagonal Lengths, which is an indicator of the *predictability time* of the dynamical system, ii) The *determinism (predictability) which can be* can be interpreted as the probability that two closely evolving segments of the phase space trajectory will remain close for the next time step and iii) The recurrence time which is proportional to the time for a trajectory to come back to the neighbourhood of any former point. The evolution of the RQA measures with the lag time has been calculated Events (=peaks) have been searched in the trends of these parameters with the lag time. Once an event is detected in the evolution of multiple parameters, the peak position is determined using the most distinctive peak.

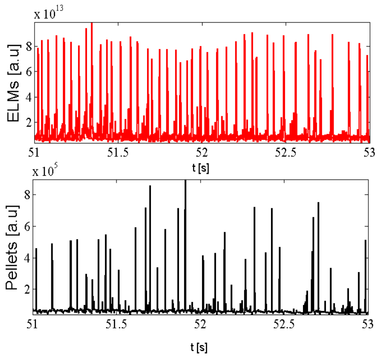

Figure 1 - Top: Dα signals identifying the occurrence of ELMs Bottom: Dα signal indicating the arrival of the pellets into the plasma.

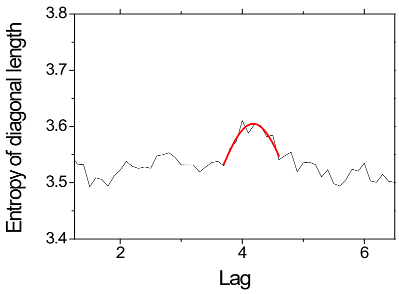

Figure 2 - Discharge 82855. A peak is very evident in the entropy of diagonal length. The entropy of diagonal length has been fitted with a spline to identify the maximum (red curve)

This peak defines the period of maximum correlation between the dynamics of the two systems and therefore it is assumed to identify an appropriate range over which the causal relation is effective. An example is shown in Figure 2.

On JET, from basic physical reasons, it has always been assumed that a pellet can trigger an ELM only if the time between the two events is less or equal to 2 ms. In order to test this working hypothesis, the three techniques introduced in the previous sections have been applied to a set of 8 JET pulses, devoted explicitly to pellet pacing: 82885, 82886, 82887, 82889, 84688, 84690, 84693, 84696.

The analysis has been performed using the D_{α} emission to determine both the occurrence of the ELMs and the arrival time of the pellets in the plasma. For these discharges, sufficient statistics and signals of adequate quality are available to allow robust estimates. In particular these plasmas are sufficiently stationary, an implicit assumption for the application of the proposed criteria.

The obtained results (Table 1) indicate that the traditional criterion use to estimate the efficiency of pellets underestimates on average the capability of this system to trigger ELMs. On the other hand, every discharge is a different case and must be studied independently. Indeed the appropriate lag time to calculate the number of ELMs triggered by pellets ranges between1.5 and 4.5 ms. The proposed criteria therefore allows assessing the properties of pellets on a shot to shot basis, paving the way for a much better understanding and optimization of this important tool in the perspective of ITER.

Table 1 - Percentage of triggering for the lag times calculated with GC, TE, JRP and with the usually assumed of 2 ms. The percentages are calculated from the ratio of the number of ELMs triggered by pellets, divided by the total number of pellets reaching the plasma for each shot.

Pulse	82886	82887	82889	84688	84690	84693	84696
Δt JRP [ms]	3.8	4.1	4.5	1.3	3.2	3.5	3.5
JRP % triggering	15	24	21	9	25	25	9
2 ms % triggering	6	11	4	9	14	17	10

Post-Mortem Analyses of Selected Samples Cut from Tiles Exposed to JET Plasma

E. Grigore, C.P. Lungu, C. Porosnicu, C. Ruset, M. Gherendi, I. Tiseanu, M. Lungu, I. Jepu, O. G. Pompilian, P. Dinca

IAP - National Institute for Lasers, Plasma and Radiation Physics, INFLPR

WP-JET2_P

The activities carried out by IAP in the framework of WPJET2 project are in accordance with the Project Management Plan (PMP). The main results corresponding to project deliverables are synthesized below.

1. Sectioning of selected Be tiles from the JET wall (WPL, IWGL and dump plate) into pieces for surface analyses (IBA, TDS, SIMS and metallography)

Marker Be tiles removed from JET by remote handling during the 2015 shutdown were disassembled in the BeHF (beryllium handling facility) at JET and were sent in Romania for cutting into small samples. A band saw device with hardened saw tooth, 2.5 m long was used for cutting. The operation was performed in the Beryllium Coating Laboratory in dry conditions. The sample temperature during the cutting operation did not exceed 70^{o}C. For temperature monitoring in real time a FLIR thermovision camera (+/- 1 ^{o}C ; 20-900 ^{o}C) was used. A number of 154 samples (12 x 12 x 10 mm^3 and 12 x 12 x 2.5 mm^3) from the WPL, IWGL and dump plate were sectioned and sent to CCFE to be distributed to EUROfusion laboratories for analyses.

2. Sectioning of W lamellas from Tile 5 retrieved from JET divertor

Sectioning of W lamellas was performed with a milling machine using special cutting discs containing more than 21% diamond powder embedded in a copper alloy. The temperature of the W lamella during the cutting operation did not exceed 70 °C. Before cutting the real bulk W lamellas the cutting technology was qualified by JET on three test lamellas. A number of 7 W lamellae (A15-A23, C02-C3, C05-C13, C02-C14, C02-C22, C02-C23, D14-D14) retrieved form JET divertor (Tile 5) after exposure in 2011-2012 were sent to IAP for sectioning. The detailed cutting plan was issued by JET. A total number of 28 samples with dimensions: 9x6x10 mm^2, 10x6x2.5 mm^2, and 2.5x6x15 mm^2 were obtained, packed in special boxes and sent back to CCFE, UK.

3. TDS and XRD analyses of the Be samples sectioned from JET tiles

The TDS analyses were performed at a heating rate of 10 K/min with a maximum temperature of 1323 K. The samples (5x5 mm) were placed in nickel holders in order to reduce the beryllium contamination of the measurement chamber due to material evaporation at high temperatures. The main desorption of deuterium occurred between 600K-1000 K reaching its maximum in most cases around the temperature of 800 K. These high temperatures of release for deuterium indicate that all samples have traps with high binding energy. These defects were produced most likely due to irradiation damage. In some cases a release of D was observed after 1200 K. This might be associated with defects into the bulk structure. The lack of low temperature peaks (below 625K) proves that the deuterium removal procedure (heating the chamber walls) is quite efficient preventing deuterium trapping and accumulation in low energy binding states. By integrating the desorption spectra the total amount of deuterium retained in Be samples was obtained. These values are in the range of (4.6-15.9)$\cdot 10^{17}$ D/cm^2.

For a full characterization of D desorption the release of heavy water (D_2O) and HDO was investigated. These compounds are usually formed in significant quantities during long time exposure of the sample to air.

It was observed that for samples with low D inventory the release of HDO and D_2O is significantly higher in comparison with that from samples with higher D content. This is typical for the case of small deuterium amount in the sample and long time exposure in the air.

A number of twenty one Be samples were analysed by XRD. The spectra emphasized the formation of beryllide compounds such as BeNi and Be_2Cr. In addition, formation of oxides such as BeO, CrO and Fe_3O_4 was also detected on particular samples.

4. GDOES analysis from selected sectioned tiles

A number of more than 20 samples cored from divertor tiles exposed to JET plasma in the first campaigns (2011-2012) were analyzed by GDOES (Glow Discharge Optical Emission Spectrometry). The results are already published.

Now GDOES has been pushed to a new challenge. This is determination of the deuterium depth profile together with the other elements into the W coatings deposited on CFC after plasma exposure. In order to do this the D channel of the GDOES machine has to be calibrated. Since there is no reference samples available on the market these samples have to be produced by ourself. We have produced Ti coatings with a D concentration of 4.0 at.% and W coatings with 1.5 at.%, but these are not enough. The work is focused now on Zr coatings with high D content. At the moment there is a preliminary calibration of the D channel that is useful in determination of D depth profiles into the Zr coatings. Since GDOES is a destructive technique, only one analysis can be done on each sample. The analyses of the last samples received from JET will be performed after final calibration of the GDOES machine. However, in order to estimate the D and Be concentrations in the W coatings exposed to JET plasma and to evaluate the capability of the GDOES method with the preliminary calibration of D one analysis was carried out using this method on the sample 2ONG8B-8d. This was cored from the Tile 8 exposed in JET during the period 2011-2012. By comparison with the initial GDOES depth profile one can say that there is no significant erosion of the outer W layer. A thin deposition of Be (1-2 μm) can be seen at the surface. It is important to notice the peaks of D concentration at all W/Mo and Mo/C interfaces.

5. X-Ray Laminography of W coated tiles retrieved from JET

X-ray micro-laminography (μXCL) was used as complementary solution for the X-ray computed tomography (XCT) method. Applying this method, 3D microstructural analysis was conducted on tungsten coated carbon fibre composite (W-CFC) samples retrieved from JET ITER-Like Wall. A number of 19 samples, exposed to JET plasma in 2012-2014 and 2011-2014 cored from Tiles 1, 3, 4, 6, 7, 8 and HFGC were analysed. It was revealed that five samples are severely damaged and can not be used for GDOES analysis. Six selected samples were inspected by μXCL with a spatial resolution of ~3 μm. Microstructural analysis shows that the W coating deposited parallel to the bundles of carbon fibers of PAN type can tolerate exposure to plasma in tokamak with no significant changes in microstructure. However, the W coating deposited perpendicular to the fiber bundles (on the ends of the fibers) is slightly affected.

The thickness of the W layer was mesured by High-Energy X-ray Fluorescence (HEXRF) on all core samples. No significant erosion was detected on these specific samples. The acquired spectra were analyzed in the W Kα and W Kβ peak region of interest based on the fact that tungsten's L characteristic lines have a saturation threshold lower than 10 μm.

6. Emissivity of W coatings deposited on CFC tiles

The emissivity value is a key parameter for determination of the real temperature and heat loads with the IR cameras. The emissivity of tungsten is rather well known, but all the literature data refer to bulk tungsten or tungsten foils with different polishing degrees of surfaces. To the best of our knowledge there is no literature data concerning the emissivity of the W coatings deposited on CFC or fine grain graphite.

In the present experiments the W coating with a thickness of 10 μm or 20 μm was applied on a CFC tube or a tube made from fine grain graphite (FGG) (Φ16 x 0.8 x 85 mm). A hole of Φ2.0 mm was drilled in the middle of the tube to play the role of black body. A K type thermocouple was introduced into the tube through an end and the welding is in contact with the wall. This arrangement ensures the same temperature for the W coating and black body and this temperature is measured by the thermocouple. The emissivity is the ratio between radiation intensity measured on the surface of interest and the radiation intensity produced by black body after subtracting the background measured near to the heated zone. The emissivity of 10 μm and 20 μm W coatings deposited on CFC tiles was measured at the wavelengths of 1.064 μm, 1.75 μm, 3.75 μm and 4.0 μm in the temperature range of 500-1200 °C. The emissivities of four samples (Φ5.2x15 mm) cored from tiles G3, G4, G6 and G7 tiles exposed to JET plasma in the first campaigns with ILW (2011-2012) were measured in comparison with a 20 μm W coating not exposed to plasma, at the wavelength of 4.0±0.5 μm. The change of emissivity was in the error limits. This means that the thin Be layer deposited on W coated tiles does not affect significantly the emissivity. This might not be true for HFGC where the Be deposition is quite thick (~ 20 μm).

Methods and Techniques Used for Assesment of Samples Exposed to JET Plasma

E. Grigore, C. Ruset, M. Gherendi, C. P. Lungu, C. Porosnicu, I. Tiseanu, P. Dinca, B. Butoi, O. G. Pompilian, C. Dobrea, M. Lungu, A. Sima

National Institute for Lasers, Plasma and Radiation Physics, INFLPR

WP-JET2C

The present project aims to address the following objectives:

- **A.** To extend the capabilities of *GDOES* (Glow Discharge Optical Emission Spectrometry) equipment in order to include D in the list of elements available for quantification,
- **B.** To provide a method to measure the tritium content within samples sectioned from tiles exposed in *JET*
- **C.** To implement *μXRF* (micro X-ray fluorescence) technique as a method for measure marker samples exposed to *JET* plasma.

A. The calibration of *GDOES* equipment for D quantification involves few steps:

a) Production of samples with D content

b) Measurement of D content by using different methods

c) Setting up the *GDOES* method for D measurement

During the deposition experiments it was observed that Zr seems to be an appropriate element able to obtain coating with suitable D content. Consequently at this stage of the project Zr+D coatings have been obtained by using *CMSII (Combined Magnetron Sputtering and Ion Implantation)* method. The deposition parameters were selected in such a manner that a nanoporous structure of the coatings to be produced. This nanostructure can accommodate a large quantity of D within nanopores formed during deposition process. As substrate material Mo and Fe samples have been used. These materials have been selected as preliminary deposition runs performed on Ti substrates showed that the Ti substrate traps D during deposition. This trapped D in substrate is released with D trapped within the coatings during the *TDS* (*Thermal Desorption Spectrometry*) investigations and thus affecting the measurement. This type of coating has been produced just for *GDOES* calibration purpose.

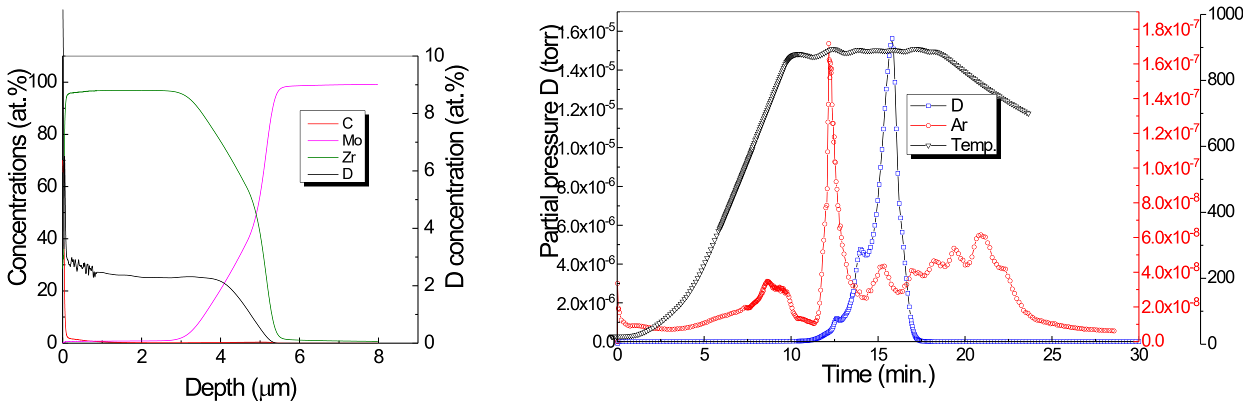

Figure 1-GDOES depth profile for Zr+D coating (top) and TDS spectrum for Zr+D coating (bottom)

In selecting Zr, as a coating suitable for project goals, an important role was determined by the fact that the Zr emission line are not superposing with the D line, whereas the D line can be clearly identified. The deposition has been performed in an Ar+D mixture. A *GDOES* depth profile of the Zr+D coating deposited on Mo substrate is presented in *Fig. 1a.*

The Zr depth profile is smooth and quite uniform across the coating and has a concentration of ~97 at.%. However for the moment the D profile had just a qualitative character. In order to get a quantitative assessment of the D, we have to get the D values measured by other investigation techniques (*NRA*. *TOF-ERDA* etc.).

TDS measurements played an important role in optimize the deposition parameters required to obtain a maximum of D content within the coatings. The *TDS* measurement was performed on coated Mo substrates (12x15x1 mm). In *Fig.1b* is presented the *TDS* spectrum for a Zr+D coating. It can be observed that the D starts to be released at ~700^{0}C and the maximum partial pressure of the D released is with two orders of magnitude higher than Ar. One the other hand the profile of D released is well defined compared with Ar released profile and from the shape of the profile it seems that all trapped D is released during *TDS* measurement.

A second type of experiments were focused on the production of W+D coating, but for the moment the results obtained by *TDS* showed a lower D release from the coating, compared with Zr+D coating.

B. The measurement of tritium content of samples sectioned from tiles exposed in *JET*

A tritium surface monitor LB 1230UMo with a LB 1230 open window gas flow proportional counter detector, Berthold type (*USA*) was used to measure the tritium content within the samples sectioned from tiles exposed to *JET* plasma. Before measurement a calibration procedure of the tritium monitor was performed. The procedure consisted of the following steps:

i. A Virgin Polyethylene/Li_2CO_3 composite was contaminated in a controlled manner with a known activity of ^{3}H (testosteron-1, 2-T);
ii. Samples were heated at 750^{0}C with a particular thermal regime (750^{0}C catalytic bed), combustion compounds trapping, measuring the activity of ^{3}H and comparing with real conventional activity initially deposed onto virgin samples.

During the experiments performed, the tritium activity was determined for 134 sectioned samples retrieved from the first wall of the *JET* reactor. The T activity at the surface of the sectioned samples was between 100 and 600 Bq/cm^2, while the number of T atoms/cm^2 were estimated between 0.7 and 2.46 $*10^{11}$

C. The implementation of *µXRF* (micro X-ray fluorescence) technique for measurement of marker samples exposed to *JET* plasma

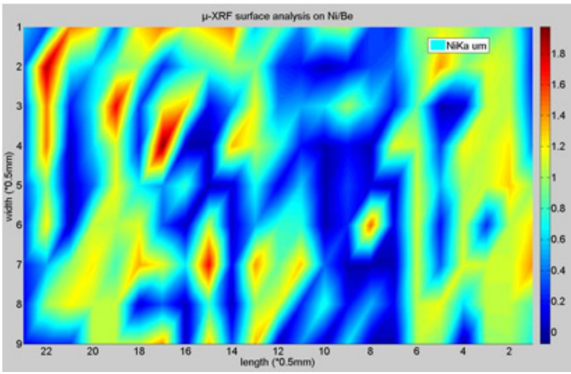

Figure 2-The 2D map of Ni thickness distribution on the upper part of 368 samples.

X-ray fluorescence (*µXRF*) technique, a non invasive analysis method, has been used to study the erosion pattern of the physical sputtering effect on the samples exposed to fusion plasma. As a particularity, the "micro-" abbreviation term stands for the spatial resolution of ~25µm determined by using a so called polycapillary focusing X-ray lens. The calibration of the *µXRF* technique was performed by using Ni deposited samples on Si substrate with the following coating thicknesses: 10, 500 and 2200 nanometers. The calibration samples were deposited by thermionic vacuum arc (*TVA*) method, and measured prior by a quartz crystal microbalance (*QCM*). After calibration *XRF* measurements were performed on 3 marker samples exposed at *JET* plasma (sample code: 367, 368, 369) deposited with Ni on Be substrate. By *µXRF* measurement was highlighted the erosion in the middle part of the analyzed samples (367, 368 and 369). A representative 2D map was obtained by moving the micro *XRF* detector with a step of 0,5 mm. In Fig.2 a 2D map with the distribution of the thickness across the sample 368 is presented.

Cutting of Be tiles and W lamellae exposed to JET plasma for analysis

C. Porosnicu[1], C. P. Lungu[1], P. Dinca[1,2], B. Butoi[1,2], O. G. Pompilian[1], I. Jepu[1]

[1]*National Institute for Lasers, Plasma and Radiation Physics, NILPRP*

[2]*Faculty of Physics, Univeristy of Bucharest*

WP-JET 3

In the framework of WPJET3 were performed the following activities: i) Cutting of Be tiles exposed to JET plasma in experimental campaigns and retrieved from ILW for analysis, ii) Cutting of W lamellae retrieved from JET.

For Be cutting, a special designed and engineered jigging device was realized. The cutting blade (The Morse Achiever bi-metal saw blade, USA) for cutting in dry condition was a dedicated one and made on special material in order to ensure the low temperature of the sample during the process. For real time temperature monitoring a FLIR® E-Series Advanced Thermal Imaging Camera, (+/- 1 °C; 20-900 °C) was used. During cutting procedure, the sample temperature did not exceed 50°C, a temperature lower than that requested in PMP (70°C). A typical cutting record is shown in Fig. 1.

Number: F70100061_H_070314_211	
1) CUT TILE IN HALF FROM REAR	**between C5 and C6**
Tile holder for first cut with band-saw ready	x
Remove Be tile piece from packaging	x
Secure tile to mount	x
Take photograph showing tile number	x
Dust collector switched on	x
First cut completed	
Maximum temperature reached (deg C)	
SAMPLES CUT AND BOXED	

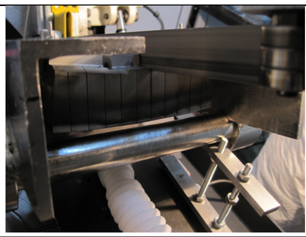

2) CUT ROW OF 12 mm SAMPLES	**C 11**
Number all castellations on exposed side	x
Record numbers in log	
Photograph showing castellation numbers	x
Prepare a box for each of the castellations	x
Secure tile to mount	x
Tile holder ready	x
Dust collector switched on	x
Cut off all samples from the side (band saw)	x
* to castellation depth of 12 mm where possible	x
Box each cut castellation	x
Record maximum temperature reached (deg C)	52
Cut completed	25'32"
Record IR file	
205, 204, 203, 202, 201, 200, 199, 198	

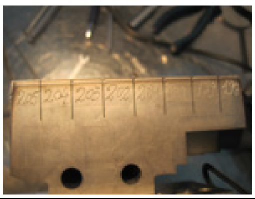

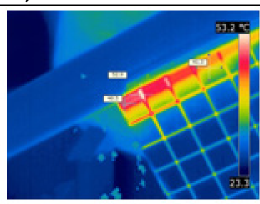

Figure 1 - Typical cutting record document.

A number of 36 samples from the IWGL plate were sectioned using the cutting machine of the Beryllium processing facility. The size of the samples were: a) 16 thick samples: 10 mm x 10 mm x 10-12 mm and b) 15 thin samples: 10 mm x 10 mm x 2.5 mm. The samples were packed (See Fig. 3) using 1" x 1" x 1" polyethylene boxes and stainless steel screws. The samples were sent to CCFE

For W lamellae cutting a detailed cutting plan and cutting draw was elaborated at JET – CCFE and sent in Romania. The cutting draw is presented in Fig. 2.

The trial cuttings were performed using a milling machine using special ordered cutting discs containing more than 21% diamond powder embedded in a copper alloy, as shown in Fig.3. During cutting procedure, the lamella temperature did not exceed 70^{o}C. For real time temperature monitoring a FLIR® E-Series Advanced Thermal Imaging Camera, (+/- 1 ^{o}C ; 20-900 ^{o}C) was used. Fig.4 shows a typical thermovision image during cutting process.

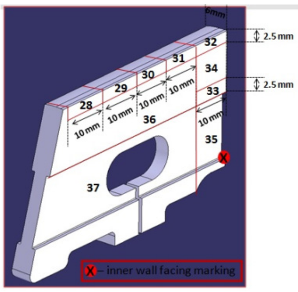

Figure 2: Cutting draw

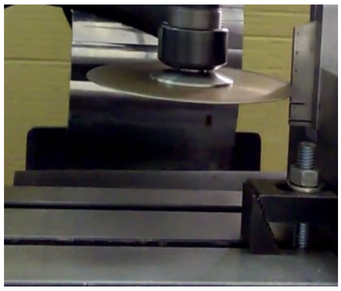

Figure 3: Diamond milling disc in action

Figure 4: Sample temperature monitored by a thermo-vision camera

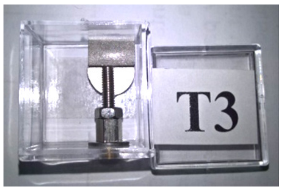

Figure 5: Trial sample T3, packed in a special box.

The trial samples were packed in special polyethylene boxes, as shown in Fig. 6, sent to CCFE and accepted. We are waiting to cut the D14 Standard – exposed lamella, A02 Clean unexposed lamella, 5 pieces from the top of each lamellae, Length = 10mm, Width = 6mm, Thickness = 2.5 mm.

Conclusion

Using Be cutting facility, 36 components of the 2XR10 tile were cut: a) 16 thick samples: 10 mm x 10 mm x 10-12 mm and b) 15 thin samples: 10 mm x 10 mm x 2.5 mm. The 36 cut samples were packed using 1" x 1" x 1" polyethylene boxes and stainless steel screw. The samples were sent to CCFE.

W lamella trial samples were produced, sent to CCFE and accepted. We received and cut the D14 Standard – exposed lamella, A02 Clean unexposed lamella, 5 pieces from the top of each lamellae, Length = 10mm, Width = 6mm, Thickness = 2.5 mm. The samples were sent to CCFE.

JET Gamma-Ray Spectrometer Upgrade (GSU)

T. Craciunescu[1], V. Braic[1], R. Costa Pereira[2], A. Čufar[6], D. Croft[3], M. Curuia[1], A. Fernandes[2], V. Goloborod'ko[4], G. Gorini[5], N. Gupta[3], A. Hagger[3], V. Kiptily[3], I. Kodeli[6], R.Kwiatkowski[7,] I. Lengar[6], R. Naish[3], M. Nocente[5], K. Schoepf[4], B. Santos[2], L. Snoj[6], S. Soare[1], M. Tardocchi5, V. Yavorskij[4], V.L. Zoita[1], I. Zychor[7]

[1]Institute of Atomic Physics, Bucharest, Romania

[2]Instituto de Plasmas e Fusão Nuclear, Instituto Superior Técnico, Universidade de Lisboa

[3]CCFE, Culham Science Centre, Abingdon, United Kingdom

[4]University of Innsbruck, Fusion@Österreichische Akademie der Wissenschaften, Austria

[5]Instituto di Fisica del Plasma "Piero Caldirola«, Consiglio Nazionale delle Ricerche, Milano, Italy

[6]Slovenian Fusion Association (SFA), Jozef Stefan Institute, Reactor Physics Department, Ljubljana, Slovenia

[7]Institute of Plasma Physics and Laser Microfusion, Warsaw, Poland

WP-JET4

As stated by the documents governing the European fusion research in the frame of Horizon 2020 ITER is the key facility. JET experiments are devoted to validate the ITER design choices and prepare ITER operations. Special attention will be dedicated also to the characterization of the ITER regimes up to full performance of JET operation with the same combination of plasma facing material as ITER (the ITER Like-Wall in JET). In this context a DT campaign is intended, which provides the final demonstration of the compatibility of high performance inductive regimes of operation with the ITER wall materials. Future deuterium-tritium experiments on JET are expected to produce a significant population of alpha-particles at plasma parameters approaching the ITER values as closely as possible. Therefore these shots will be a good opportunity for examining confined and lost fusion alphas. The confinement of fast particles produced in fusion reactions is of crucial importance for future fusion devices like ITER and DEMO.

A number of diagnostic upgrades are necessary for fusion α-particle measurements. Among them the upgrade of the KM6T spectrometric system in order to bring it at the desired level of compatibility with the future DT campaign. The main objectives are:

- Design, manufacturing and installation of an assembly of components (the Radiation Field Components Assembly, RFCA) for the definition and control of the radiation fields (both neutron and ?-ray)
- ii) Replacement of the existent BGO-detector with new detector modules based on LaBr3/CeBr3 scintillators and an associated digital data acquisition system
- Modelling of the time-dependent fusion alpha-particle distribution for the development of a procedure for generating synthetic gamma-ray spectra with the final aim of consolidating alpha-particle modelling with experimental data.

IAP Romania is coordinating the project consoritum which includes the following partners: CCFE UK, ÖAW Austria, CNR Italy, IPPLM Poland, IST Portugal, SFA Slovenia.

The RFCA is composed of two neutron and gamma tandem collimators, a fixed gamma ray shield, a movable gamma ray shield and three neutron attenuators. One neutron attenuator is placed inside the movable gamma ray shield and the other two attenuators are fixed, placed in front of the KM6T detector inside the detector tunnel. The movable gamma ray shield is moved vertically by means of a synchronous system for two jack screws driven by an electric motor and has three predefined working positions (Fig 1): bottom, for DT discharges; middle, to act as a gamma-ray shutter; top, for DD discharges. The movable gamma ray shield positions are detected by means of optoelectronic sensors. Based on information received from them a programmable logic controller (PLC) controls motor operation and direction of movement.

Following the identification of a series of clashes with the adjacent diagnostics (the KX1 X-ray spectrometer), a substantial revision of the RFCA detailed design was carried out during 2016. By the end of the year, the revised drawings have been completed and submitted to the JET operator in order to be checked against to British standards and the JET internal documents. The Technical Control Documents – Request (TCD-R) and Interfaces (TCD-I) were issued and approved for both the mechanical and the command and control components of the RFCA.

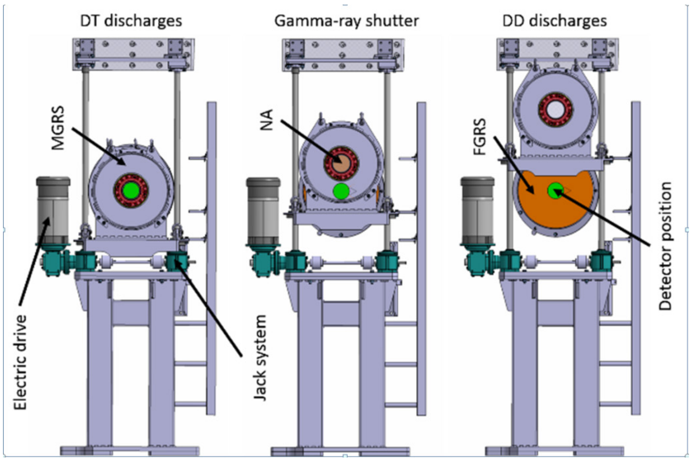

Figure 1 - : Movable Gamma-Ray Shield (MGRS) working positions. DT discharges: lower position. Gamma-ray shutter: middle position. DD discharges: top position. (NA: Neutron Attenuator. FGRS: Fixed Gamma-Ray Shield).

For the TCD-I JET has requested some additional information regarding the operation of the movable gamma-ray shield. The requested information was obtained by applying the finite element analysis (FEA) to the components of the movable gamma-ray shield. The results have shown that the device can operate within safe limits. The additional work requested by JET together with some changes on the operation of the JET installation have resulted in a delay in the manufacture of the RFCA. This is now planned for the first quarter of 2017, while installation at JET is planned for the second quarter.

In order to enable the gamma-ray spectroscopy diagnostic for -particle diagnostic during the DT campaigns it is necessary to maximize the signal-to-background ratio at the spectrometer detector (this ratio is defined by terms of the plasma-emitted gamma radiation and the gamma-ray background) and to ensure a high count rate signal processing and energy-resolved gamma-ray detection. Therefore new detectors and a new data acquisition system (DAQ) have been developed. The construction of new detectors based on LaBr3 (CNR) and CeBr3 (IPPLM) crystals and also of the new data acquisition system (IST) has been accomplished together with experiments regarding the calibration and characterization measurements. The integration of both detectors with data acquisition system has been successfully achieved. Several algorithms real-time pulse processing algorithms have been developed (IST) in order to handle the high count acquisition rate characteristic for the DT campaign.

The assessment of different features of the GSU system has been performed by means of Monte Carlo numerical simulations. In 2016 the CeBr3 detector response function has been evaluated by simulations performed using Geant4 (IPPLM). An estimation of uncertainty of transport calculations (neutron and gamma fluxes and spectra) has been performed using the MCNP and ADVANTG codes. An attempt to characterize the different sources of uncertainty has been also developed.

In what it concerns the alpha-particle modeling, OEAW and CCFE have worked during 2016 on the developing and verification of the Fokker-Planck code FIDIT, including the submodules SNBI (Source of NBI ions) and SEDORP (Space and Energy Distributions of Reaction Products) for modelling time-dependent distributions of confined alpha particles. The code takes into account convective transport as well as the diffusive transport associated with collisions and magnetic perturbations due to TF ripples and EFCC. In the course of code development a radial diffusion coefficient caused by RMP was derived for energetic ions. The time dependent calculations of the evolving distribution function of fusion alphas were carried out for specific JET shots. The obtained distributions were used for the interpretation of gamma-ray measurements on JET.

Quality Control Monitoring of Demo Magnets by Fully 3D X-Ray Microtomography

I. Tiseanu, D. Dumitru, T. Craciunescu, C. Dobrea, M. Lungu, A. Sima

National Institute for Lasers, Plasma and Radiation Physics, INFLPR

WP-MAG-P

The Microtomography group of INFLPR participates at the Magnet System Work Program (WPMAG) to provide the non-invasive examination of DEMO TF conductor structure by X-ray Computed Tomography (XCT). Till now only one of the proposed conductor prototypes was successfully manufactured i.e. the Wind & React rectangular conductor solution.

XCT on DEMO cables generate a large amount of images to be analysed for tasks as: strand detection, twisting pattern assessment, structural integrity etc. Obviously, these tasks make it very hard for the human eye to be carrying out an absolute measurement which makes it inefficient or rather slow. Hence, an automatization program is imposed, however, building an algorithm is also hard because of the following issues encounter on each tomogram: high isotropy in background noise, difficulty to separate the pixels that belongs to the strands and the pixels from the background, variations in size and intensities of strands sections, unclear boundaries for various strands (because of some clustery distribution or of a faded strand section) , and a bad distribution of strands (individual or clusters). Each tomogram is a grey-scale image which even the, human eye and brain are not capable of carrying out any of these tasks with absolute reliability.

Because that strands sections looks like an almost circular shape with high pixels' values, viewed as source points, we can build an algorithm from a simply and efficient approach of analysis and detection of these source points photometrical techniques. Hence, we can apply the fitting functions tools over these source points, known as point spread function (or PSF).

The photometric method is based roughly on seeking the local density maxima and fitting the point spread function in a Gaussian profile, within Full-Width-Half-Maximum (FWHM) interval and a threshold peak value. The object centroid (X,Y) is identified, using marginal xi and yi distributions of the Gaussian kernel.

The main steps of the photometric specific algorithms are the following:

1. Searching and localize high density pixel values (source points), with positive brightness
2. Apply rejection criteria in order to distinguish the strand section with the background noise
3. Apply a subroutine capable to distinguish a class of non-strand detections, including the jacket of the CiCC cable or the inside pipes of He flow.

The best candidate, tested so far for the fitting profile, is the Gaussian kernel :

$$G(\Delta i, \Delta j; \sigma) = e^{-(\Delta i^2 + \Delta j^2)/2\sigma^2} \tag{1}$$

where σ denotes the image standard deviation and (i,j) are the pixel coordinates. Basically, the image tomogram is converted in a 3D matrix, where at each position (i,j), we will have the pixel value. This matrix is convolved using a Gaussian kernel defined in equation 1. The fitting is done by using a linearized least square method. In the first step, a globally searched is performed to identify the local density maxima, then on each pixel is applied the analytic Gaussian profile. The fit is good, after it is achieved the maximum central height of the Gaussian profile. A rejection criteria is than apply, in order to avoid any false detection. This criterion is based on a given threshold value for width of the Gaussian profile (the value of FWHM) and its height.

After the fitting procedure, the object's centroid (X,Y) is estimated, using marginal x_i and y_i distributions of the Gaussian kernel. Hence the coordinates of the strand section is identified by the following formula:

$$X = \bar{x} = \frac{\sum I_i x_i}{I_i}, \quad Y = \bar{y} = \frac{\sum I_i y x_i}{I_i} \tag{2}$$

The radius of the strand can determine from the FWHM using the following relation:

$$radius = FWHM/2.355 \tag{3}$$

This methodology can work very well on crowded field of strands and was successful applied on the tomograms of different types of CiCC cable (TFQL, JTF) where over 95% rate of strands detection has been achieved. This method was tested now on a DEMO cable of CiCC type (Figure 1a):

a)

b)

Figure 1 - DEMO cable subjected to X-ray tomography

Using the raw picture from Figure 1a and convert it to grey scale, the fitting algorithm for strand detection has been successfully applied, leading to the recognition of all the strands inside the jacket (Figure 1b).

However, after X-ray tomography application on the DEMO cable, the analysis of the strand detection is considering to be not optimal. The rate of strand detection was rather low, for around 20% (Figure 2)

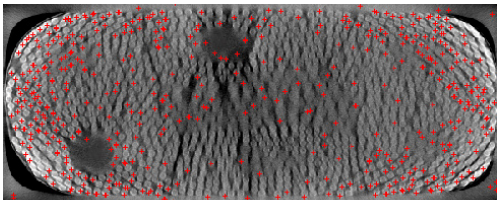

Figure 2. Detection on a DEMO tomogram

Several issues make the detectability to be very low because of the rejection criteria which automatically disprove the true strands. These results are mainly because of the high background noise, low pixel's value and low standard deviation which make almost impossible or inaccurate the strand detection (the detection parameter is under the threshold value).

Further on, it will be continued with improving the rate of detection and centroid positions, by implementing more advanced method for fitting tools, such as: non-linear fitting (i.e. non-linear Gauss fit, with noisy data), fit multiple Gauss, in a functional formulation or cumulative distribution function (i.e. Voight profile).

The photometrical analysis can be used for strand detection, however, different difficulties that rise from the DEMO tomogram, impose serious limitations on our algorithm and rise several constructive questions, in order to improve our methodology. High rate of detection and centroid positions, is achievable and it will be further on tested if several correction or improvement will be performed: by implementing a more advanced method for fitting tools, such as non-linear fitting (i.e. non-linear Gauss fit, with noisy data), fit multiple Gauss, in a functional formulation or cumulative distribution function (i.e. Voight profile).

Microtomography analysis of DEMO magnet Nb_3Sn superconductor strands

I. Tiseanu, T. Craciunescu, C. Dobrea, M. Lungu, A. Sima, D. Dumitru

National Institute for Lasers, Plasma and Radiation Physics, INFLPR

WP-MAG-C

The main objective of the project is to develop a high accuracy micro-tomography examination process with a micron-sized pixel to be able to diagnose deformation of strands in contact zone and to detect cracks in Nb3Sn under mechanical / electrical cycling.

In order to get the proposed results, one uses an optimized cone-beam tomographic setup using an open type nanofocus X-ray source with the maximum high voltage at 225 kVp and with a maximum power of 15 – 30 W. The X-rays are detected by means of an amorphous silicon flat panel sensor with a pixel size of 74.8 μm. This setup relies on the micron size resolution of the X-ray tube in order to get high space resolution images by relatively large geometrical magnifications. The challenge is that when working with such high magnification, the focal spot of the X-ray source needs to be extremely stable over a long period of time. In practice, because of different factors such as temperature variations and high voltage generator instabilities, the focal spot migrates during the acquisition period of time. We minimize this occurrence by controlling the temperature in the experiment room.

The 3D tomographic reconstructions are obtained by Oblique View Cone Beam CT (OVCB-CT) a proprietary highly optimized computer code, based on a modified Feldkamp algorithm. Beam hardening artefacts are reduced by a correction method based on X-ray spectrum filtering and the linearization of the transmission curve. Further reduction of artefacts was achieved by specially designed pre- and post-filters.

Practical superconducting cables used in large scale applications (e.g. magnets for fusion reactor) consist in superconducting

filaments embedded in a normal-conducting matrix. matrix. The common technique to reduce the eddy-current losses is to twist the wire and the filaments during the manufacture. This also reduces the time-independent proximity effect between the filaments and its associated loss. Currently, the only method for measuring the twist-pitch consists in evidencing the twisted structure by etching techniques. This method is destructive and does not permit the visualization of the filaments. X-ray micro-tomography permits the non-destructive reconstruction of the 3D image of the fusion relevant multifilamentary wire enabling the determination of the number of inter-filament contacts on unite lengths well as the twist-pitch parameter. This can be used to develop a more complex model of the multifilamentary superconducting wire in order to explain the role of the internal wire structure on the superconducting transport properties.

Determination of twist-pitch factor

In the reporting period, we realized an examination of a selection of Nb3Sn superconductor strands of ITER/DEMO type.

For the non-invasive evaluation of the twist-pitch factor estimated at around 15 mm we developed two methods: A) the first method uses a set of several highly-resolved tomography images collected equidistantly on a 20-mm long strand in order to determine the average twist-pitch factor; B) the second method is based on a global reconstruction of the strand fragment of 20 mm.

A) High resolution (voxel resolution 0.9 μm) and sharp images of the Nb3Sn filaments were acquired with low noise threshold. Based on these results, the dimensions of each filament and of each cover jacked could be measured and also the manufacture faults could be easily observed (Figure 1).

Due to the high resolution and magnification X-ray scanning investigation, only few mm on the z axis could be measured in one experiment cycle (360-degree rotation of the sample). Each X-ray scanning experiment cycle provides information for only 1.2 mm on the z axis of the superconducting wire. In order to investigate the entire length of the superconducting cable (20 mm) and also for the determination of the twist pitch factor, many successive experiment cycles had to be conducted. A total of 10 measurements on the length of the superconductor were conducted in order to interpolate the total acquired information. Each ring of Nb3Sn filaments was analysed separately. For each slice and each filament, the relative position in pixels, related to the image coordinates was determined. The origin of the coordinate system is attached to the image center. Every reconstruction slice was passed through some processing steps such as image alignment, filtering and segmentation. The last step of the procedure consists in the labelling of each filament and calculating their exact spatial position (x, y) in every section of the reconstructed superconductive wire.

Using the information regarding the spatial position of every filament in each section of ~1.2 mm we estimated that each Nb3Sn bundle needs approximately 13.75 mm of strand length to achieve a full 360-degree twist.

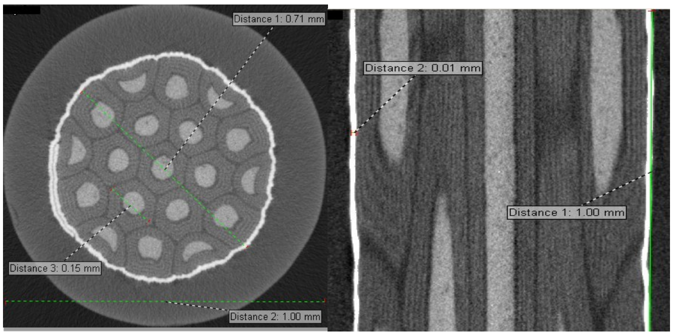

Figure 3 Micro-tomography cross-sections of an Nb_3Sn strand (left figure). Strand components as Nb_3Sn bundles, Nb barrier and Cu matrix are very well resolved (right figure)

B) In order to validate the twist pitch factor, we conducted a tomography scan that analyses in only one cycle the entire strand fragment of 20 mm. Even if this method obviously provides poorer resolution images (voxel resolution 10.85 μm) we still have the possibility to distinguish each individual filament for the entire strand (*Fig.*).

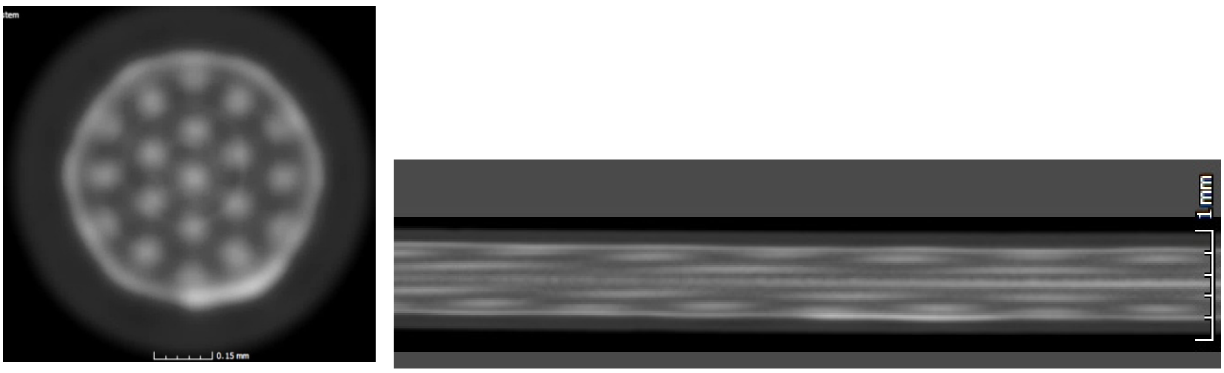

Figure 2: Micro-tomography cross-sections of an Nb_3Sn strand: left - axial, right - frontal

Appling the micro-tomography examination method we were able to determine the structure and also to point out any manufacturing defects on the Nb3Sn filament bundles and also on the resistive barrier.

The twist-pitch factor was estimated in a non-invasive manner by two methods: i) using a set of several highly-resolved tomography images collected equidistantly on a 20-mm long strand in order to determine the average twist-pitch factor and ii) image processing of a global reconstruction of the whole strand fragment of 20 mm.

In the next phase of this project we will use an innovative tomography setup based on a newly developed high energy TDI type of X-ray detector.

Development of multi-metal laminates and thermal barrier materials, thermo-physical characterization of HHF materials produced in WPMAT

A. Galatanu, M. Galatanu, M. Enculescu, G. Ruiu, B. Popescu

National Institute of Materials Physics, Romania

WP-MAT-P

W laminates are considered as possible heat sink materials for DEMO divertor. In this frame, our work in 2016 was focused on the fabrication of W laminates with different metals using a FAST route and also investigating their structural and thermal properties. FAST joining of metallic materials is a technology which combines diffusion bonding and electrical point welding (due to discharges across contact surfaces on micrometric scale) on the whole contact surface at once, while the whole sample is heated by Joule effect. The obvious advantage of this route resides in the short processing time, with lower recrystallization detrimental effects, meanwhile allowing for temperatures up to the metal melting points and making the joining process similar to brazing. In the case of multi metal W laminates, the deposited layers can tune the Joule heating at the interfaces during processing time and consequently improving the interface microstructure. More important the multi-metal approach creates a promising route to improve the performance of materials during high temperature exposure. Multi-layered composites (W-multi-metal metal laminates with Ti and V) with different rectangular shapes have been produced for microstructural and thermal properties investigations. Before joining, a thin layer of ~100 nm Cu or Cr was deposited by RF magnetron sputtering on both sides of the W foils. Since the previous work was performed with rather old W foils (produced in ~1980 by Plansee) we have now reproduced the experiments with new W foils, with 0.1 and 0.05 mm thickness produced be Plansee (2015). A comparison of micro-structural results and thermo-physical properties shows better interfaces and lower thermal contact resistance in the case of new foils, respectively, for both as produced and 1000°C -1000 hours annealed W-V samples.

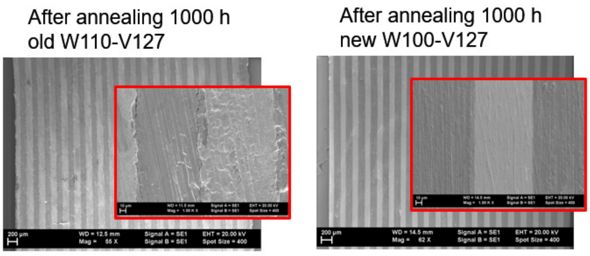

Figure 1 - Comparison of W-V laminates produced with different batches of W.
A clear improvement can be seen for the materials produced with new W foils.

For W-Ti laminates, the prolonged high temperature exposure has a dramatic effect due to the W-Ti inter-difussion. However, as the present results show, by using a thin deposited Cr or Cu layer the interface quality was preserved even after prolonged high temperature exposure. This provides a way to use the W-Ti laminates at higher temperatures (even above 1000 °C), when Cr is used as interface layer.

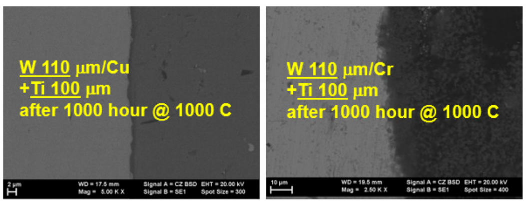

Figure 2 - W-Ti multi-metal laminates produced with deposited Cu or Cr thin layers.
The interface quality is preserved event after prolonged high temperature exposure.

To analyse the effects generated by the additional buffer layer on thermal properties of the laminates, the thermal contact resistance has been measured for different Ti foil thickness. The results for Cr deposited W-Ti laminates show small values, typical for joined materials, i.e. of the order of 10^{-5} m^2K/W. In the case of Cu deposited W-Ti laminates, the values are even lower. Thus we can conclude that this procedure does not affect the overall thermal conductivity of the composites.

Thermal barrier materials might be used to protect the structural materials in the DEMO reactor, controlling the heat flow through various heatsink components. Since such materials are also interface materials between armour and structure, matching the thermal expansion coefficients of these different parts is important. The main objective of the task is to find and characterize suitable materials for various possible DEMO divertor designs, and then to include such materials in relevant 3 layers system for further mechanical and HHF tests. Cu based composites with oxides (Y, Al, Zr), SiC and C additions in a large concentrations range (up to 80 % for ZrO_2) have been produced using spark plasma sintering at temperatures around 900°C for 5 minutes in different shapes. The most stable composites are produced using micrometric Cu powders with micrometric C powder or nanometric oxides and SiC powders. Since in the case of DEMO divertor a typical heat flux of 10 MW/m^2 is expected, and taking into account that the optimal operating temperature window for W is between 800 °C and 1200 °C, while for CuCrZr heat sink materials the operating temperature should not exceed 300-350 °C we have defined a selection criteria for the produced thermal barrier materials, as depicted in the left panel of Fig. 3.

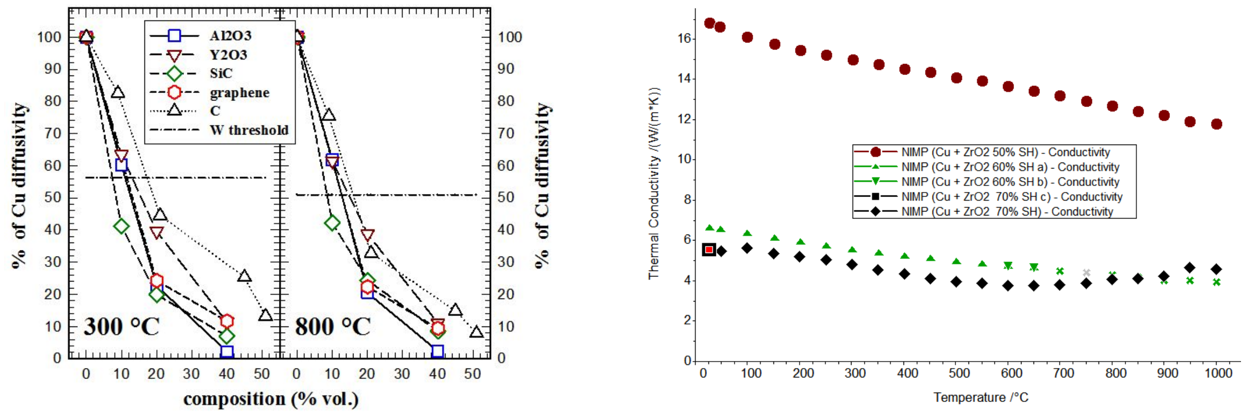

Figure 3 - Selection of suitable thermal barrier materials (left) and ultra-low thermal conductivity Cu-ZrO_2 materials suited for thin layers in the W monoblock divertor design (right).

While all materials can be implemented in different design systems, for W monoblock design an additional requirement was imposed related to the TB dimensions which should not exceed a 1 mm thickness. In this case, much lower thermal conductivities are needed (around 10 W/m/K) and therefore we have focussed our work on Cu-ZrO_2 composites, taking into account that Zr-oxides has itself a very low conductivity. For zirconia concentrations above ~55 % volume the thermal conductivity fulfil the requirement in whole investigated temperature range. The selected materials have been implemented in 3 layers systems with W and Cu or CuCrZr. The specimens have been joined using the FAST technology already developed in our institute. These samples will be further joined to special stages (provided by JFZ) and sent back to JFZ for HHF tests in relevant DEMO conditions.

Thermo-physical properties evaluation of the DEMO materials is especially important for plasma facing components and heat sink materials, since they have to absorb and transfer a high heat flux, respectively. In our research unit we can perform such investigations from RT up to 1100 °C (thermal transport properties, LFA), from RT up to 1600 °C (dilatometry), from RT up to 600 °C (DSC) and from RT up to 800 °C (electrical conductivity and Seebeck coefficient). In 2016 we have evaluated thermal properties (thermal diffusivity, thermal conductivity and thermal expansion coefficient) of different materials produced in NIMP and by other groups from Eurofusion (e.g. JSI, IPP, KIT, CEA). More than 150 measurements have been performed, about half of them on materials provided by other research units.

Development of experimental techniques for improved interfaces and nondistructive investigations of High Heat Flux Materials

A. Galatanu[1], M. Galatanu[1], G. Ruiu[1], I. Tiseanu[2], T. Craciunescu[2]

[1]National Institute of Materials Physics, Romania

[2]National Institute for Laser, Plasma and Radiation Physics, Romania

WP-MAT-C

To achieve realistic conditions for HHF tests (to be performed in FZJ by partners in Eurofusion consortium) as well as for irradiation and plasma jets test to be performed by NILPRP partners, the samples must fulfil adequate conditions, related to shape, composition and properties. Here the most important aspect is related to the joints between different materials, because their failure or low performance might produce erroneous results for the materials investigated. In this stage the main work of NIMP was devoted to detrmine the optimal joining parameters for multilayered samples containing W-based armor materials and CuCrZr-X alloys. The samples have been produced using SPS (W-materials) with the already established procedure. The SPS-ed W-based pellets were further joined to commercial CuCrZr-X alloys at 890 C using the FAST joining procedure developed in NIMP. The resulting 30 x 10 x (3-8) mm^3 samples (see figure 1) were then further cut for different investigations.

Figure 1 - Joined W-CuCrZr specimens.

This processing route was used also to produce 3-layers systems for testing the W-thermal barrier-CuCrZr mock-ups by HHF, thus offering an uniformized image about the materials properties in all tests.

One of the possible cooling solutions for DEMO reactor involves the use of a liquid Pb-Li eutectic. In this case, some of the components of the blanket will be in contact with the molten metal. The interaction with liquid metals has adverse effects on the exposed materials (corrosion, liquid metal embritelment). A risk mitigation solution is to coat the exposed metals with a special (usually oxide) thin layer. Such a layer might affect the thermal transfer between the components and the cooling fluid. Therefore we have investigated the thermal transport at the metal (T91) liquid lead interface using our LFA equipment.

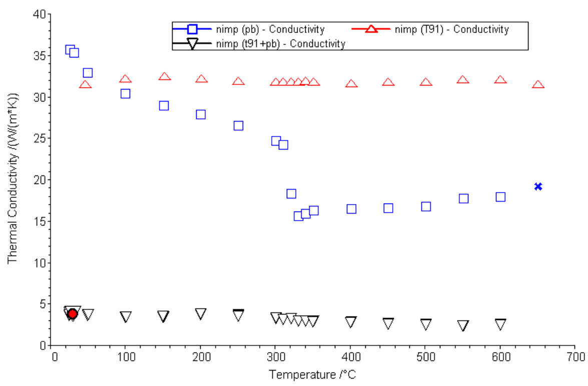

Figure 2 - Thermal conductivity of steel, Pb and steel+lead.

As a test a T91 steel with different coatings (provided by KIT) was used. T91 has similar properties with Eurofer, one of the basic candidates for structural materials in DEMO. Figure 2 shows thermal properties of the basic materials and their combination, where a strong decrease of thermal conductivity can be observed.

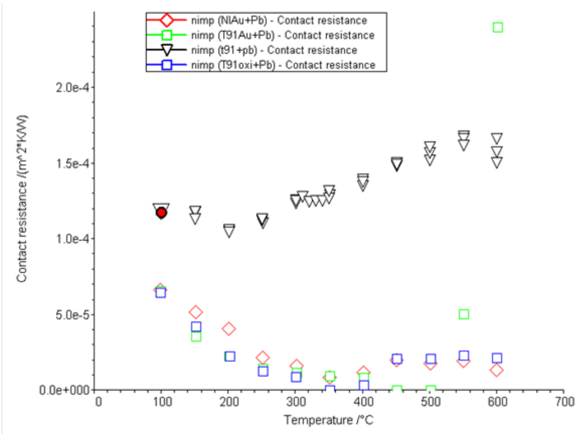

Figure 3 - Thermal condtact resistance for the liquid lead - metal (coated with different materials) interface.

The calculated thermal contact resistance has indeed high values (as ploted in figure 3), showing a weak wetting of the steel by liquid Pb. Note that the values are comparable with those of the simply pressed steel-Pb sandwich. To further verify the wetting role in the thermal transport we have tested other materials and coatings (e.g. Au coating, know to consistently improve the Ni wetting by liquid Pb). As shown in figure 3, Au coating of steel also contributes to a reduced thermal contact resistance. An import point is that the usual oxide coating of steel also reduces the thermal contact resistance, implying that such treatments will not have detrimental effects from the heat transfer point of view.

One of the best way to investigate the microstructure of larger components is offered by X-Ray computer micro-tomography. Microtomography studies with a space resolution of ~1.5 µm can be carried out in NILPRP using a newly developed high resolution X-ray target made of 1.2 micron tungsten layer deposited on a 0.25 mm thick diamond window.

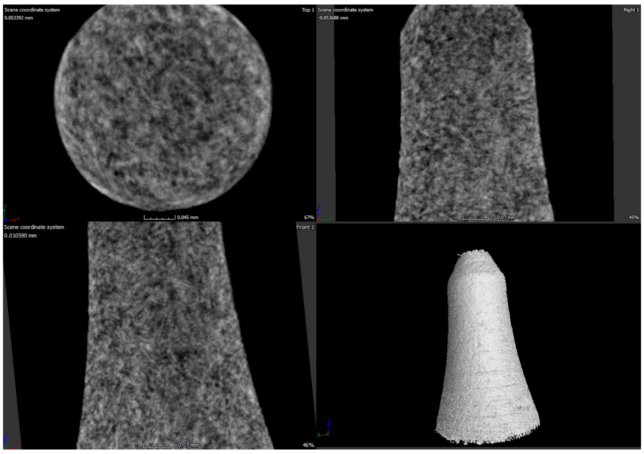

Figure 4 - Reduced artevacts in XRCT image reconstruction of W-Cu dense composites (Cu melt infiltrated W preforms, provided by IPP Garching)

However, the microtomography of W/Cu bulk materials is very challenging due to the very strong reconstruction artefacts caused by the very high X-ray absorption coefficients of the constituent materials. The reduction of the reconstruction artefacts of beam hardening type was attempted by a new Iterative Artefact Reduction algorithm implemented in our reconstruction software. Several experiments have been dedicated to the calibration of the focal spot migration and technical solutions have been implemented in order to reduce the focal spot drift. The global artefacts from tomographic sections have been correlated with the shapes and dimensions of the sample section.

Improvement of Irradiation Set-Up and Tests on Materials

C.M. Ticos, M.D.D. Grivei, D. Ticos, N. Udrea, A. Scurtu, N. Iacob

National Institute for Laser, Plasma, and Radiation Physics

WP-MAT-C

Testing of materials developed for fusion technology is essential for validation of the relevant fabrication technologies. At our electron accelerator facility ALID 7 we irradiated samples made of different metals with a high energy electron beam (6 MeV). An improvement of the testing conditions has been achieved by upgrading the experimental setup and placing the samples in vacuum (4×10^{-2} torr) during irradiation. A picture of the setup is shown in Fig. 1.

Fig. 1 Improved irradiation setup; the electron beam is incident from the top.

The beam exiting the accelerator enters the vacuum chamber through a dedicated port provided with a 5 cm diameter opening which consists of an Al foil with a thickness of only 40 µm. The energy loss of the electron beam incident on the samples is below 1% of the 6 MeV, measured previously with a magnetic spectrometer. The samples were positioned right underneath the thin Al foil in vacuum, and centred before each irradiation with the axis of the electron beam.

The beam current has been measured with a calibrated Faraday Cup (FC) FARC-04-2M made by Radiabeam. The ALID7 is a traveling-wave electron accelerator which delivers pulses of 4 µs duration at a frequency of 50 Hz with an average peak current in the several 10's mA. The beam current can be slightly varied by modifying the filament current of the electron gun and tuning the magnetron for the maximum dose output. The pulsed electron beam measured by the FC is shown in Fig. 2. The main parameters are: total charge per pulse 150 nC, peak current per pulse 60 mA resulting in a current density of about 7mA/cm^2 per pulse. The fluence per pulse is about 1.7×10^{11} e/cm^2. For an irradiation time of 60 s the total incident fluence on a sample is 5.1×10^{14} e/cm^2.

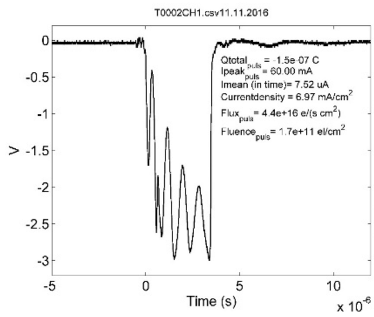

Fig. 2. A single electron beam pulse measured with the FC and captured by the oscilloscope.

Many types of samples were irradiated in this setup configuration. Four types of samples are presented in the following: alloys such as Ni-Cr, Mo-Re, stainless steel (SS) AISI 316 and a high purity metal such as Mo. The samples were small chips of approximately 1.5 cm × 1.5 cm polished with very fine grit (1200) consisting of diamond powder. The irradiation time was 60 s for all samples.

Ni is a corrosion resistant element extensively used in alloys. It has the melting point at 1455 ^{0}C, a density 8.91 g/cm3, a hardness on the Mohs scale of 4.0, and structure fcc. Cr is largely used in stainless steels alloys due to its resistance to corrosion. It has a melting point at 1907 ^{0}C, a density of 7.19 g/cm3, a high hardness of 8.5, and a structure bcc. The sample made of Ni(80)-Cr(20) has a thickness of 0.5 mm. It is visibly affected by the EB irradiation. Its exposed surface becomes free of crevasses, cracks or holes with an apparent smoothness of under 1 μm.

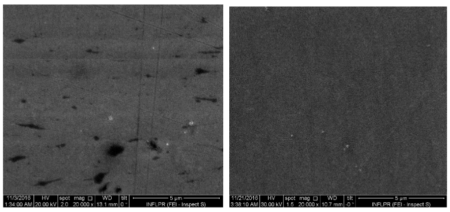

Fig. 3 Ni-Cr at ×20000 before (left) and after (right) 60 s irradiation with EB.

Mo is a metal with a high melting temperature (2623 ^{0}C) and high density (10.28 g/cm3) with a bcc structure and a hardness on the Mohs scale of 5.5. The Mo sample is made of pure metal (99.9%) and is 1.5 mm thick. Small crevasses with diameters of a few microns and lengths up to 10 um are clearly smoothed out after a 60 s irradiation, as shown in Fig. 4. The only apparent modification induced by the EB is therefore on the surface layer 1 to 2 micron thick.

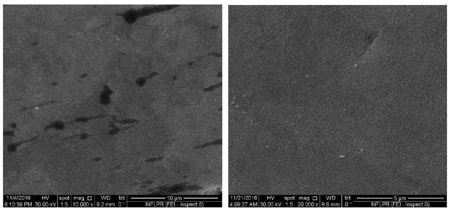

Fig.4 Pure Mo at ×10000 left and ×20000 right before (left) and after (right) 60 s irradiation with EB.

Re is high melting point element with a temperature of 3186 ^{0}C. It has a density of 21.02 g/cm3, more than double that of Mo, a hardness 7.0 and a hcp structure. The sample made of Mo(52.5)-Re(47.5) has a thickness of 0.125 mm. Apparently it does not suffer any surface morphological changes as shown in Fig. 5

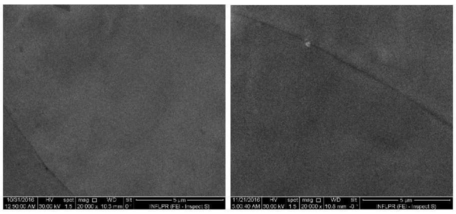

Fig. 5 Mo-Re at ×20000 before (left) and after (right) 60 s irradiation with EB.

Stainless Steel AISI 316 (Fe/Cr18/Ni10/Mo 10) has been used with a thickness of 1 mm. It is visibly affected by the EB, its surface full of holes and scratches left after the polishing process being completely smoothed out, as shown in Fig. 6. A few defects however are still seen in the SEM images after irradiation.

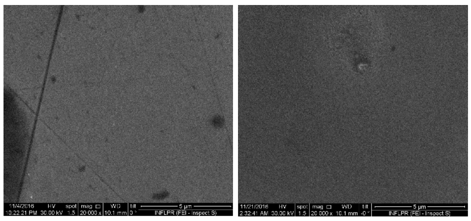

Fig. 6 Stainless Steel at ×20000 before (left) and after (right) 60s irradiation with EB.

Developing and Producing Reference Coatings for PFC.SP2, PFC.SP3 and PFC.SP5

C. P. Lungu[1], E. Grigore[1], C. Ruset[1], C. Porosnicu[1], P. Dinca[1,2], B. Butoi[1,2], O. G. Pompilian[1], I. Jepu[1], M. Gherendi[1]

[1]*National Institute for Lasers, Plasma and Radiation Physics, NILPRP*

[2]*Faculty of Physics, University of Bucharest*

WP-PFC-P

Within the framework of the PFC SP5.4 project the following activities have been performed at *IAP*: i) Production and characterization of Be and Be-W coatings with high D and N thicker than 5 µm; Be, W, and different Be-W composite films with and without gaseous content (D, He, N, O); ii) Thick Be-C, Be-O layers for comparative studies; iii) Different roughness W, Be and W-Be layers production for implantation studies; iv) Production and characterization of W+He coatings with He content (thickness >5 µm); v) Production and characterization of W-Al+He coatings (thickness >5 µm, He 5 at.%); vi) Production and characterization of W-N+He coatings (He content of 5 at.% and N content of 5 at.%); vii) Production and characterization of W+D coatings (thickness >5 µm); viii) Production and characterization of W-N+D coatings (thickness >1µm,N content of 5 at.%).

Be-C layers with O and D gas inclusions were obtained by a combination of High Power Impulse Magnetron Sputtering (*HiPIMS*) and Direct Current Magnetron Sputtering (*DCMS*) techniques co-deposited in a reactive gas of Ar, D, O. Structural and compositional studies on these layers were performed after the depositions. The structural characterization of the films was performed using X-ray diffraction (*XRD*) method.

The homogeneity and composition of the films was verified. Fig.1 presents the elemental depth profile of Be-C structures obtained at the same plasma parameters but different D/O ratio. The depth profiles show a homogenous distribution of Be, C and O along the film depth. The depth scale measured by the *RBS* is given in unit of atoms/cm^2.

Deuterium retention and release from trapping sites for Be-C layers as well as the evaluation of deuterium content was performed using *TDS*. The D desorption charts for Be-C structure show a minor desorption peak between 425K and 470K which corresponds with the one found in literature for a supersaturated Be:D trapping state, also all samples present a desorption shoulder between 500K and 600K associated with the deuterium release attributed to decomposition of beryllium deuteride BeD_2. A major peak observed around 680K-730K is associated with desorption from BeOD related traps. The release peak at 925 K can be related to the carbon/carbide trapping sites. Fig. 2 shows this dependence and the deuterium retention is decreasing with the increase of C/Be ratio.

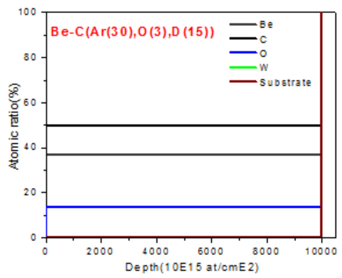

Figure 1 – Calculated atomic ratios vs. thickness (elemental depth profile)from RBS spectra for Be-C samples with different D/O ratio

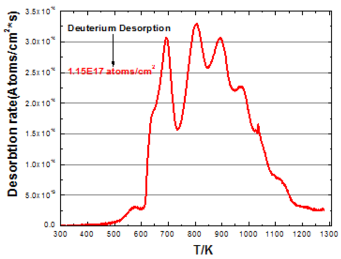

Figure 2 Deuterium desorption spectra obtained for Be-C with D and O gas inclusions layers co-deposited on silicon substrates

W based coatings with gas inclusions have been obtained by using *CMSII* (Combined Magnetron Sputtering and Ion Implantation) method. Two types of coating have been obtained:

- coatings with He inclusions (W+He, W-Al+He and W-N+He)
- coatings with D inclusions (W+D and W-N+D)

The specifications asked for different thicknesses of the coatings and different percentage of the gas inclusions. The deposition parameters have been adjusted in order that a nanoporous structure of the coatings to be produced. This strategy has been adopted as most of the gases required to be included within the W coatings forms no compounds with W. This nanoporous structure produced is able to trap gas inclusion like D and He within the structure of the coating. After deposition a preliminary characterization of the coating has been performed. This preliminary characterization helped also in optimize the deposition parameters. The characterization of the coatings included *GDOES* (Glow Discharge Optical Emission Spectrometry) investigations for chemical composition and coating thickness measurements, *TDS* measurements for assessment of He and D content. In Fig. 3 a *GDOES* depth profile performed on a W+He coating of 6 µm is presented. The gas content within the coatings have been measured by *ToF-ERDA* at *RBI* Croatia, however a preliminary He and D content measurements has been performed at *IAP* by using *TDS* investigation. A *TDS* spectrum for a W+He coating is presented in Fig. 4. The assessment of the capabilities of the W based coatings with gas inclusions (He or D) to withstand thermal stress has been also performed.

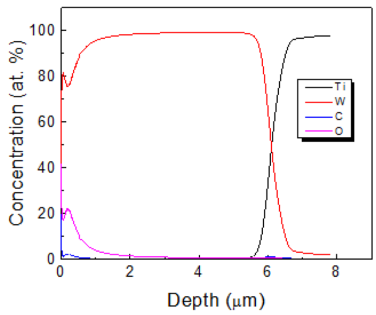

Figure 3 - GDOES depth profile for W+He coating

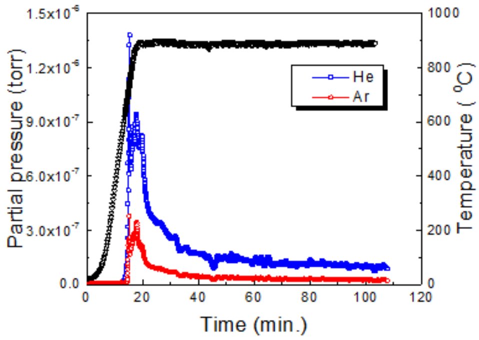

Figure 4 - TDS spectrum for W+He coating deposited on Mo

After the deposition and the preliminary characterization, all the produced samples have been forwarded to different labs from research units across Europe for additional investigations or to be used within different tasks within *WPPFC*.

Besides these types of coating 3 Mo discs (30mm in diameter) coated with W with thickness >5 µm have been required to be produced in order to be used for subsequent D implantation at Differ.

Conclusions

Within the framework of the PFC SP5.4 project the following activities have been performed at *IAP*: production and characterization of Be and Be-W coatings with high D and N thicker than 5 µm, Be, W, and different Be-W composite films with and without gaseous content (D, He, N, Ne, Ar, O); Thick Be-C, Be-O, W-O layers for comparative studies; different roughness W, Be, si W-Be layers production for implantation studies; Production and characterization of W+He coatings with He content of 10.7 at.% (determined by *TOF-ERDA*); Production and characterization of W-Al+He coatings with He content of 9.3 at.% and Al content of 12.9 at.% (determined by *TOF-ERDA*); Production and characterization of W-N+He coatings with He content of 4.6 at.% and N content of 7.6 at.% (determined by TOF-ERDA); Production and characterization of W+D coatings of 3.2 µm; Production and characterization of W-N+D coatings of 3 µm (N content measured by GDOES was ~8 at.%).

The preliminary characterization of the coatings performed at *IAP* included *GDOES* investigations for chemical composition measurements and *TDS* measurements for assessment of He and D content and for optimization of the deposition parameters in order to comply the produced samples with specifications.

Optimization of the HiPIMS and TVA methods for obtaining Be and Be-W coatings with high D and N contents. Characterization for Be, C, D, N containing plasma / W-coated FGG samples for GDOES analysis

C. P. Lungu, C. Porosnicu, P. Dinca, B. Butoi, O. G. Pompilian, C. Ruset, E. Grigore, I. Tiseanu, M. Lungu, A.Sima

National Institute for Lasers, Plasma and Radiation Physics, NILPRP

WP-PFC-C

1. Complex Be based coatings deposited by magnetron and TVA techniques

Magnetron deposition parameters using the HiPIMS (High Power Impulse Magnetron Sputtering) technique were optimized. The TVA method for Be coating was improved as well. Structural and compositional studies on the layers prepared using these techniques were performed after the deposition. The structural characterization of the films was performed using X-ray diffraction method. Elemental depth profiles, respectively elemental area densities were determined by means of Rutherford Backscattering Spectrometry. Experimental deuterium desorption spectra were obtained with a thermal desorption spectroscopy system. It was observed that the deuterium retention in the sample was highly dependent of C/Be ratio. The deuterium retention is decreasing with the increase of C/Be ratio.

For the following experiments, Be-C mixed material layers were obtained using a combination of HiPIMS/DCMS techniques in a circular chamber with a diameter of 60 cm operated in ultrahigh vacuum conditions of 10^{-6} mbar with a turbo-molecular pump. Silicon (12 mm x 15 mm) and mirror finished graphite (12 mm x 15 mm) were used as substrates for these coatings. The substrates were placed on a fixed sample holder placed inside the reaction chamber and positioned between the two sputtering sources at a distance of 10 cm. The water cooled magnetron heads were equipped with high purity (99.95%) graphite, respectively beryllium circular targets (two inches in diameter/3 mm thickness). The graphite cathode was operated in HiPIMS mode driven by a high power pulse generator which was triggered from a signal generator. The target current and voltage were measured and the waveforms were monitored using an oscilloscope. The beryllium cathode was operated in DCMS mode with the total power input value situated at 91 W for all depositions.

For Be-C mixed layers with D and O seeding deposition, the chamber was pumped down to a base pressure lower than 10^{-5} mbar. Argon (Ar) gas was feed inside the reaction chamber and Be and C magnetron plasma was initiated. This standard cleaning procedure was used for the removal of target impurities. The substrate holder was covered with a shutter until the plasma was stable. After this stage the reactive D and O gases were introduced through two separate mass flow controllers (MFCs) into the chamber to be co-deposited with Be and C. During all depositions the total working pressure was maintained at $2*10^{-2}$ mbar by adjusting the rotation speed of the turbo-molecular pump and the Ar flow rate was maintained at 30 sccm.

Structural analysis was carried out by performing X-Ray diffraction measurements on the Be-C layers co-sputtered with HiPIMS/DCMS techniques in a reactive gas mixture Ar-D-O. In order to obtain accurate results a sample deposited on silicon substrate was measured. The analysis was performed using a diffractometer provided with CuKα X-ray source, with the wavelength 0.154 nm in the 2θ range from 20^{o}-110^{o}. X-ray diffraction pattern obtained for Be-C layers deposited in an Ar-D-O gas mixture reveals two peaks which were later identified as corresponding to polycrystalline silicon (substrate). Although the RBS measurements identified Be and C as major components for the samples, no XRD peaks corresponding to a Be-C or oxide phase was identified. This leads to the conclusion that Be and C are present in the samples in an amorphous phase. The cause of this amorphization is possible to be related with the gaseous inclusion from the layers or to the deposition conditions.

Deuterium retention and release from trapping sites for Be-C layers as well as the evaluation of deuterium content was performed using TDS. The investigated samples were loaded in a quartz tube which was in direct link with a Pfeiffer Vacuum Quadrupole Mass Spectrometer (QMS). This system was pumped down with a turbo-molecular pump in order to reach the ultrahigh vacuum measurement conditions at a base pressure of 10^{-8} mbar. The heating rate was controlled with a thermocouple placed in the centre of the oven in the vicinity of the sample. The temperature was automatically adjusted through the power supply to maintain a stable heating rate of 10 K/min until the final programmed temperature of 1273 K is reached. The sample temperature, though not directly measured, was extrapolated based on previous calibrations for different types of substrates. During the entire heating process, the amount of deuterium released from the film was measured.

Table 1 Elemental atomic ratio of Be-C samples

Sample index	Atomic ratio (%) Beryllium	Atomic ratio (%) Carbon	Atomic ratio (%) Oxygen	Atomic ratio (%) Deuterium
50160418_2	39.97	29.20	28.91	1.85
50160419_2	36.49	48.83	13.31	1.35
50160420_2	29.48	20.29	48.45	1.76
50160427_2	27.27	32.57	38.67	1.48

2. W erosion in WEST divertor (preparatory phase)

For a tokamak, as a nuclear fusion reactor, the divertor is a crucial component, handling the highest heat and particle loads in the vessel, and allowing access to high plasma confinement regimes (H mode).

In order to minimize the risks for the ITER divertor procurement (in terms of cost, delays, performance) and gaining time for its operation, the WEST project was launched at CEA Cadarache. It consists of implementing a divertor configuration and installing an ITER like actively cooled tungsten divertor in the Tore Supra tokamak, taking full benefit of its unique long pulse capability. The implementation occurs in two phases. In its first phase of operation the WEST divertor contains more than 900 tungsten-coated FGG tiles with inertial cooling. The W-coating was performed at INFLPR, Bucharest using Combined Magnetron Sputtering and Ion Implantation (CMSII) technology. A Mo interlayer of 2-3 μm was introduced between the W layer and the FGG substrate. This configuration allows the determination of the W erosion by comparing the results obtained before and after plasma exposure in tokamak. Two methods (X-ray Computed Laminography/Fluorecence – XCLF and Glow Discharge Optical Emission Spectrometry – GDOES) will be developed and applied in the framework of this project for this specific application. In the second phase of WEST project the W-coated graphite tiles will be replaced by actively cooled ITER like divertor elements.

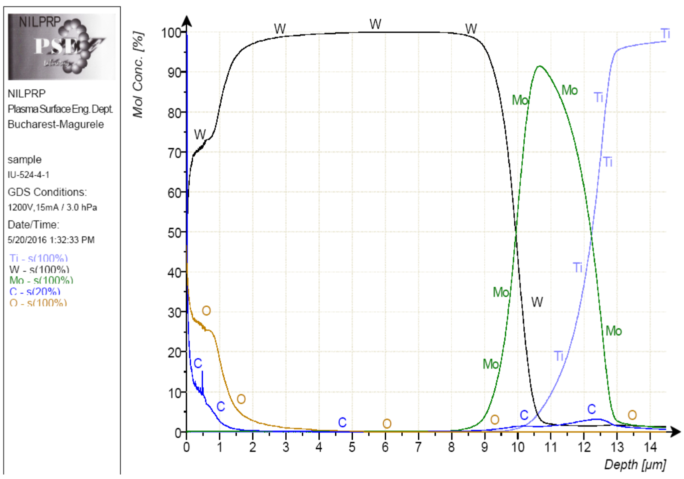

Figure.1 GDOES depth profiles for the coating run IU-524 (sample IU-524-4)

Measurement of W erosion using GDOES technique requires W-coated FGG samples produced in the same coating run, exposed and not exposed to the tokamak plasma. The samples exposed to the plasma will be cored from specific tiles after about one year of operation in WEST. On the other hand it is very important to have witness samples made from FGG and coated in the same run with the real tiles, not-exposed to plasma. In this respect a number of 30 cylindrical samples (Φ7x10 mm) were manufactured from FGG and coated together with the divertor tiles in 5 coating runs. The samples were positioned in such a way that they give the characteristics of the W coating in 6 different regions along the tile. There are short tiles with a length of 256 mm and long tiles of 326 mm. Besides tiles in each run four standard Ti samples (30x23x2.5 mm) and six FGG samples were coated. The tiles are rotated in the coating chamber in front of the magnetrons and consequently the witness samples reproduce exactly the characteristics of the coating deposited on the tiles in a certain position.

At the moment, there are W-coated FGG witness samples for a number of 73 tiles both long and short. After plasma exposure in WEST a number of these tiles will be removed from divertor and analysed. Small samples (Φ7 mm x10 mm) will be cored from the areas corresponding to the positions of the witness samples. Then the GDOES depth profiles will be analysed comparatively. A typical GDOES depth profile is shown in Fig. 1. The GDOES analysis gives the depth profiles for the concentrations of the elements from the surface layer. The results are correlated with the SEM analysis performed on the flank of the GDOES crater. In this way the structure of the surface layer is associated with its composition. The same FGG witness samples can be used as reference samples for XCLF measurements.

Multi-Probe System for Linear Plasma Devices Diagnostic

C. Costin, V. Tiron, V. Anita, G. Popa

Alexandru Ioan Cuza University, Faculty of Physics,

Iasi, Romania

WP-PFC-P

Plasma diagnostic of a linear magnetized plasma device using time-dependent measurements of a multi-probe system

Experimental data obtained with a multi-probe system on Magnum-PSI were used to establish a diagnostic method and a data processing protocol meant to obtain most of information with a minimum number of measurements during future experiments with multi-probe systems in linear magnetized plasma devices. Time-dependent measurements have been performed in Magnum-PSI on both current and voltage of 8 probes situated on a diagonal of the multi-probe system (Figure 1a). Each probe was connected to its own measuring circuit (Figure 1b). The operation of the circuit and the experimental procedure were described in ref. [1-2].

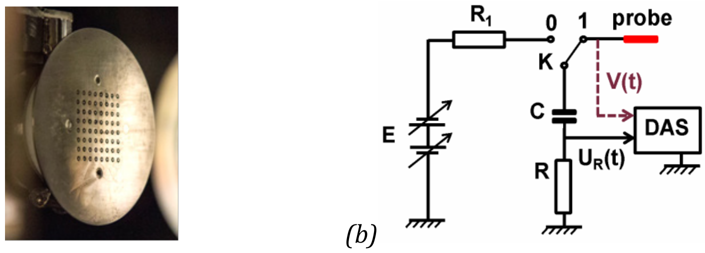

(a) *(b)*

Figure 1 - (a) The multi-probe system; (b) the measuring circuit.

The charging state of the capacitor C (initially charged to V_0) is changed in time by the probe current drawn from the plasma. The probe potential $V = V(t)$ and the probe current $I = I(t)$ are registered. This process is on till the current intensity goes to zero and the probe potential becomes the floating one (V_f). The current-voltage characteristic of the probe, $I = I(V)$, can be obtained by eliminating the time from the two temporal functions. Two measurements are required to obtain the entire I-V characteristic of the probe. When $V_0 < V_f$, the so-called *ion branch* of the characteristic, $I_i = I_i(V)$, can be obtained. When $V_0 > V_f$, the so-called *electron branch* of the characteristic, $I_e = I_e(V)$, can be obtained. The entire current-voltage characteristic of the probe is the combination of the two branches [1].

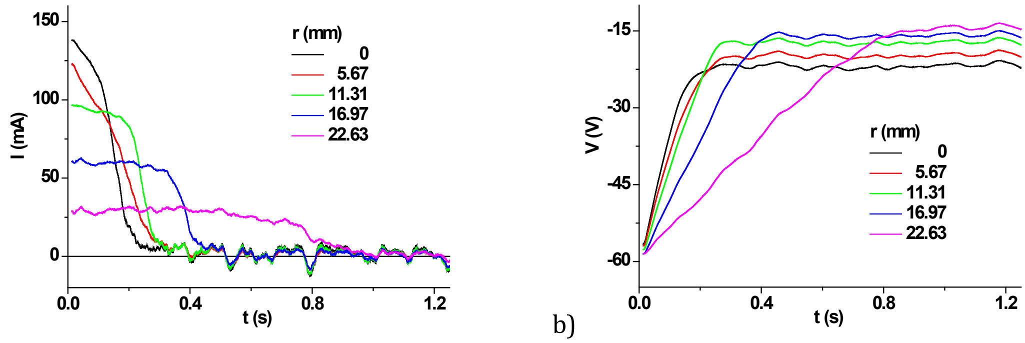

Figure 2 - Temporal evolution of the ion current (a) and the corresponding probe potential (b) registered at different radial positions in the plasma column (smoothed data).

Figure 2 shows an example of smoothed (time-averaged) temporal evolutions of the probe current $I = I(t)$ and potential $V = V(t)$. The different radial positions in the plasma column are expressed with respect to the centre of the plasma column. Discharge conditions: H_2 gas, flowing at 5.8 Pa×m^3/s, 175 A discharge current, 0.95 T magnetic field in the middle of the coils, which corresponds to 0.07 T at the measuring point (target position) [2].

In the case of lack of data acquisition channels, the so-called *integral approach* [1] can be used in order to obtain the current-voltage characteristic of a probe. The method consists of measuring, in time, only the current intensity $I(t)$ flowing from the plasma through the probe while the corresponding probe potential $V(t)$ can be calculated using an integral relation.

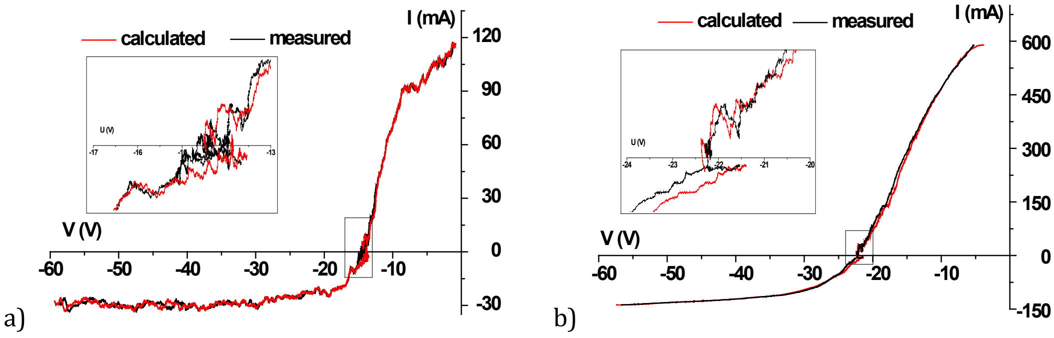

Figure 3 - Comparison of the measured and calculated probe current-voltage characteristic at (a) r = 22.63 mm and (b) r = 0 mm (smoothed data). Floating potential zone in insert.

Figure 3 shows two examples of measured and calculated probe characteristics, obtained for two radial positions in the plasma column: r = 22.63 mm and r = 0 mm (the same discharge conditions as Figure 2). Please note that the current-voltage characteristics in Figure 3 preserve the conventional representation. Both examples show a very good agreement of the measured and calculated characteristics. The sensitive part of the characteristic is the region of the floating potential, where the two branches connect to each other. The match of the two braches is not always perfect, and that depends either on the precision of the data acquisition system, or on the standard measuring error when the fluctuations of plasma parameters exceed the precision of the system.

Once the current-voltage characteristic of the probe is obtained, some local plasma parameters such as ion saturation current I_{i_sat}, electron temperature T_e, floating potential V_f and plasma potential V_p, can be estimated.

Design of a new measuring circuit

A new electrical circuit (Figure 4) was designed for diagnostic of non-stationary plasmas. It is based on the same idea of using an initially charged capacitor which can be discharged in time by the probe current drawn from the plasma [1]. The new concept allows repeating the sequence charging-discharging the capacitor for several times.

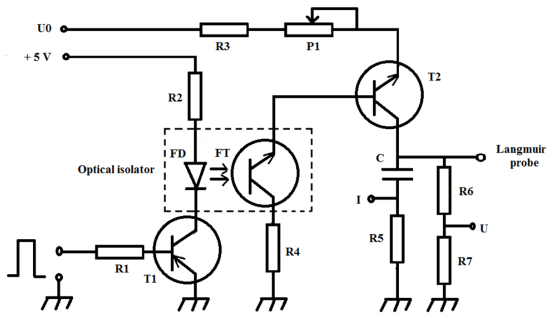

Figure 4 – Electrical scheme of the new measuring circuit.

On the base of transistor T1 we apply a rectangular signal with variable t_{on}/t_{off} ratios and variable frequency. This signal allows controlling the on/off mode of charging the capacitor C. During the time t_{on} the capacitor is charged to the voltage U_0 (U_0 is negative with respect to the ground in the present design) and during the time t_{off} the capacitor is discharged by the probe current. The ratio t_{on}/t_{off} of the rectangular signal is chosen so that the capacitor charging time (t_{on}) is much shorter than the capacitor discharging time (t_{off}). When the capacitor is discharged, the probe current I can be measured as the voltage drop on the resistor R5 and the probe voltage U can be measured with the voltage divider R6-R7. The current-voltage characteristics of the probe can be obtained with a repetition frequency set by the signal generator. The measuring circuit can be synchronized with the discharge. Each probe of the multi-probe system must have its own measuring circuit. Figure 4 shows the circuit for a single probe. The electrical circuit was tested for a single probe measurement.

References

[1] C. Costin, G. Popa, V. Anita, Rev. Sci. Instrum. 87 (2016) 033506 (7 pp).

[2] C. Costin, V. Anita, F. Ghiorghiu, G. Popa, G. De Temmerman, M.A. van den Berg, J. Scholten, S. Brons, *Plasma Sources Sci. Technol.* 24 (2015) 015014 (10 pp).

Assessment of W erosion at high temperature under exposure to H containing plasmas. Experimental treatment setup with integrated plasma diagnostics

C. Stancu, V. Marascu, E.R. Ionita, S.D. Stoica, M. Teodorescu, G. Dinescu

National Institute for Laser, Plasma and Radiation Physics, Romania

WPPFC-C

1. General objective of the project

The project focuses on assessment of W erosion and surface modification at high temperature under exposure to helium/hydrogen containing plasmas.

2. The objectives of the activities in the present stage of the project

In this stage of the project we focused on study of the hollow cathode discharge and the plasma stability. Design and development of an experimental tungsten treatment setup with integrated plasma diagnostics, allowing determination of plasma species and parameters, was realized. Also, preliminary investigation on the tungsten exposed surfaces, by profilometry, was realized.

3. Results

Experimental conditions

Plasma was generated in RF (13.56 MHz) in a vacuum chamber pumped by a rotary pump and a Roots pump. A hollow cathode configuration for the discharge was used. The electrode consists in two tungsten leaves (15x15x0.1 mm) placed face to face separated by a gap of 3 mm. The discharge was generated in helium which was admitted in the chamber by a mass flow controller. The parameters used for plasma investigation were: RF power = 300 W, He flow rate = 300 sccm, pressure = 40 mbar. 40 mbar was selected in order to have a stable discharge inside the gap. This pressure was continuously maintained by a valve positioned between vacuum chamber and pump.

For diagnostics, two experimental setups were used: i) experimental setup used for optical emission spectroscopy (OES) investigation, and ii) experimental setup used for Langmuir probes and mass spectrometry investigations.

Electrical characterization of the discharge

We made voltage-current (V-I) measurements using a SOLAYL vigilant sensor connected very close to the discharge. With Tektronix MSO5104B oscilloscope were collected the waveforms for voltage and current. The work forward power value was 300 W (13.56 MHz). The V-I waveforms were acquired with hollow-cathode discharge and in the absence of hollow-cathode discharge (non-localized glow discharge). For both discharges we observe strong harmonic distortions, also for both current and voltage. We performed Fast Fourier Transformation (FFT) on acquired waveforms.

Using the relation (1) was calculated the active average power taking into account first 6 harmonics from waveforms.

$$P_a = \frac{1}{2}\sum_{n=1}^{m} U_n I_n \cos\Delta\varphi_n \tag{1}$$

where, P_a - active average power, $m = 6$ - the number of first harmonics taken into account, U - voltage amplitude values, I - current amplitude values and $\Delta\varphi$ - phase difference values.

The active average power with hallow-cathode discharge was 291 W and in case of glow discharge was 262 W.

Spectra recording

OES investigations were realized using a Horiba Jobin Yvon FHR1000 spectrograph coupled with an ICCD Andor iDus DV420A-OE camera. Due to the configuration of the vacuum chamber the distance between optical fiber and hollow cathode electrode was 56 cm and the collected light was from entire plasma (gap and close to the electrode). From the OES spectrum, we observed that the most important lines correspond to He. However, we observe the following W lines: 361.75 nm ($5d^5(^6S)6s$), 376.84 nm ($5d^4 6s^2$), 378.07 nm ($5d^5(^6S)6s$), 400.87 nm ($5d^5(^6S)6s$), 407.43 nm ($5d^5(^6S)6s$) and 429.46 nm ($5d^5(^6S)6s$).

Langmuir probes investigation

Langmuir probes investigations were realized using a Hiden Analytical probe system. Due to the configuration of the used vacuum chamber, and the narrow interelectrodic gap, the collecting head of probe was inserted in the chamber at 10 cm distance from the hollow cathode electrode. Therefore, the information obtained is not specific to the hollow cathode region. The collected electrons were therefore from plasma margin. The obtained values were: floating potential (V_f) = 36.8 ± 2.8 V, plasma potential (V_p) = 38.9 ± 2.17 V, electron temperature (T_e) = 0.44 ± 0.13 eV, electronic density (ne) = $9.5 \times 10^{15} \pm 1.4 \times 10^{14}$ m^{-3}, ionic density (ni) = $6.3 \times 10^{15} \pm 5.5 \times 10^{14}$ m^{-3}. It is expected that the values in the center of the hollow cathode electrode are higher.

Mass spectrometry investigation

For the mass spectrometry investigation, the Hiden Analytical EQP 100 mass spectrometer was used. The distance between hollow cathode electrode and mass spectrometer head was 10 cm. The mass spectra of plasma neutrals were obtained using the spectrometer ionizer, in presence and absence of plasma, in the same conditions of pressure and mass flow rate. The most important observed species were: He_x^+, H_2O, C_2H_2, O_2^-, Ar^+. Some impurities like hydrocarbon traces from vacuum chamber are included. Due to the helium ionization, a decrease of the neutral helium mass intensity is observed when the plasma is On. Neutral W atoms were not detected. We have looked also for the energy distribution of the plasma ions. Important to mention that are specific energies, at which the ions reach a maximum in numbers, specifically 9 eV for the W^+ ions and 58 eV for the He^+. This difference in the most probable energy relates to the electron energy distributions and the different ionization potentials of the two atom types ($E_{i,W}$= 7.8 eV, and $E_{i,He}$= 24.6 eV). Also, the zone where ionization occurs may have influence.

Surface investigation by profilometry

The modification of the surface of the tungsten samples was investigated by KLA Tencor P7 profilometer. Investigation of the tungsten surfaces were realized using following parameters: x=50 µm, y=50 µm, speed = 2 µm/s, y spacing = 500 nm, applied force = 2 mg, RMS = 733 nm. These parameters were used in order to have the maximum resolution of the profilometer. The measurements were realized in contact mode and the results are conforming to ISO25178. From profilometry investigation we observed that the surfaces roughness decrease with the temperature increasing and increase with the exposure time increasing.

4. Conclusions

Tests with the new hollow cathode electrode plasma operation and plasma characterization were realized. Electrical characterization of the discharge, OES, Langmuir probes and mass spectrometry investigations were performed. Electrical measurements showed that the largest part of the forwarded power is transferred to the hollow-cathode part of discharge. From the OES spectra we observed that most intense lines correspond to He. We also found lines, with smaller intensity, which correspond to tungsten. From the ion mass spectra, we observed tungsten isotopes (between masses 160 and 190) and gas and impurity species. Detection of W species points out to an electrode erosion effect, accompanied by the release of W atoms in plasma. From profilometry investigation we observed that the surfaces roughness increases with the time of exposure to plasma.

Development of Catalogue Query tool

V. Pais, V. Stancalie, C. Iorga

National Institute for Laser, Plasma and Radiation Physics,
Atomistilor 409, P.O.Box MG36, Magurele-Ilfov, 077125 Romania

WPISA-P

Development of modeling codes for ITER, requires a complex computation infrastructure. The current infrastructure is composed of a server cluster, having a large number of processing nodes, two parallel file systems and advanced mechanisms for access to resources. In this context, the European project WPISA (Infrastructure Support Activities) aims at improving the existing infrastructure by developing and integrating new modules and applications in order to better use existing hardware resources and to create a collaborative environment for creating complex simulation codes. In previous projects, a "portal" system was developed to allow the users to access resources offered by the computing cluster through a web interface.

The current project aims at improving the existing functionalities available through the "portal" and development of new applications that will be integrated in the "portal" as well. One of the envisaged applications is a simulation catalogue that will keep a track of the simulations executed on the computing infrastructure. This application will index in real time the data files produced by running simulations and will offer a portal based interface for advanced queries to be performed on the collected data. The purpose of this queries is to identify possible patterns of interest appearing in data or files that can be used as inputs in new simulations. Considering the large number of simulations taking place on the computing infrastructure, it is foreseen the need to use advanced indexing and search features, specific to "Big Data" applications. Furthermore, the developed interface for querying the system must allow users to express queries in a human-like form, easy to express and understand. The system will then process such queries and transform them, allowing execution against the internal database.

The catalogue querying tool allows formulating queries from a user-friendly interface, hiding the complexity of SQL requests.

There are two types of pages:

- A main page for query formulation and to display the list of entries matching the query
- Pages displaying the content of a given entry, created when clicking on an entry in a list of the main page.

An elementary query is of type <variable_name><operator><value>. The searched variable can be of three types:

- Entry definition (shot, user, machine, data_version, run)
- Time interval definition (time_min, time_max)
- Summary CPO variable
- PUT_DATE (date at which the entry was put in the catalog)
- Existence of a CPO/occurrence in the data entry

The GUI provides a user-friendly way of formulating the queries, from drop-down menus filled with available values for <variable_name> and <operator>. Variable categories could be defined to ease the choice of variables (avoid too long flat list in a drop-down menu).

Clicking on a line of the result list generates a new widget with the entry definition + annotations, the list of available time intervals (content of the interval table for that entry_id), as well as (at the bottom) the list of variables names, definitions and values (content of entry_data table for that entry_id), for a given time slice of the entry (given interval_id, by default the first one in case of coming from an ENTRY list or the one on which the user has clicked in case of coming from a TIME INTERVAL list).

Clicking on a given time interval allows displaying the variable values for that time_interval, refreshing the bottom of the page.

The catalog tools populate the SQL DB from the Summary CPO/IDS (or an array of structure of it), and sends back data in the same form, while the preparation of the Summary CPO/IDS is the responsibility of the data provider.

The general architecture and integration for the entire catalog system is presented in Fig. 1.

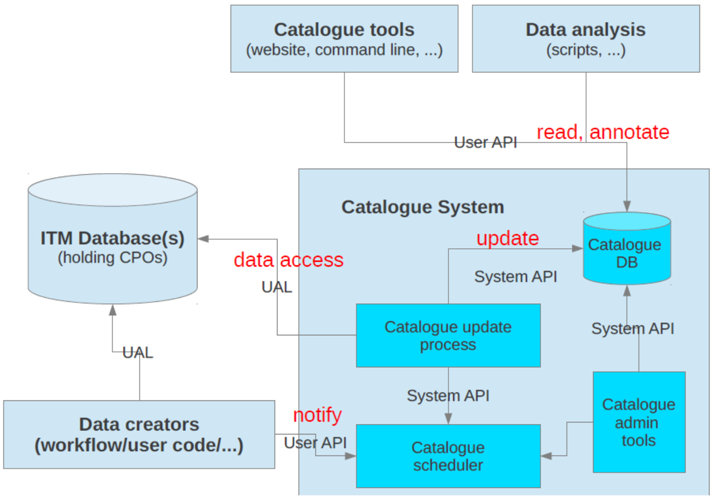

Figure 1 – General Architecture

Regarding the web technology used for the web interface, it was decided to use the current state of the art technologies. Therefore, the web interface is developed using HTML 5 functionality. Additional modern libraries were used including JQuery and Bootstrap in order to give a nice user experience.

Investigation of noSQL databases for fusion research

V. Pais, V. Stancalie, C. Iorga , A. Stancalie

National Institute for Laser, Plasma and Radiation Physics, Romania

WPISA-C

The present project aims to investigate the usage of noSQL databases for portal and data applications used in fusion research. These are new and innovative technologies for high performance databases, easily scalable for both storage and high speed requirements. Currently, a growing number of activities are investigating the use of such databases for their purposes. However, fusion related applications have specific characteristics, which may or may not fit with the specifics of this kind of databases. In this context, this project aims at investigating on various aspects related to fusion research and see how well noSQL databases can be used to increase performance of codes or to improve the user experience.

One of the key aspects of WPISA work package is to maintain a user interface for users to access the computing platform. This interface is presented in the form of a web Portal that integrates various tools running on the computing cluster available to users. Currently, this portal is using standard, proven, technologies, relying on traditional SQL databases, namely Postgres databases, and other storage systems developed within the community. One of the specific goals of this project is to investigate how this portal will behave if the underlying data storage system is moved to a noSQL database.

Fusion applications make use of large volumes of atomic data. This data is either directly acquired from experiments, via data acquisition systems, or computed by running atomic physics simulation codes.

There are two cases when access to atomic data is required:

- User interfaces: may involve functions like search and retrieval, pattern identification, plotting
- Simulation codes: usually make use of previously stored atomic data as input and produce new sets of data as output.

Structuring atomic data into traditional database features, like tables, can be easily accomplished for user related tasks. However, for simulation codes it's usually better to have complete files (either text or binary). Especially in the case of binary files, these can be accessed efficiently in high performance computing (HPC) environments, using specific functionality, such as the one offered by MPI implementations.

NoSQL databases represent a special kind of databases, that do not allow for SQL queries. Apart from this distinction, they also implement a different philosophy in the way data is stored and retrieved. There are 4 main types of noSQL databases:

- Key-values Stores: The main idea here is using a hash table where there is a unique key and a pointer to a particular item of data. The Key/value model is the simplest and easiest to implement. But it is inefficient when you are only interested in querying or updating part of a value, among other disadvantages. Examples: Tokyo Cabinet/Tyrant, Redis, Voldemort, Oracle BDB, Amazon SimpleDB, Riak
- Column Family Stores: These were created to store and process very large amounts of data distributed over many machines. There are still keys but they point to multiple columns. The columns are arranged by column family. Examples: Cassandra, HBase
- Document Databases: These were inspired by Lotus Notes and are similar to key-value stores. The model is basically versioned documents that are collections of other key-value collections. The semi-structured documents are stored in formats like JSON. Document databases are essentially the next level of Key/value, allowing nested values associated with each key. Document databases support querying more efficiently. Examples: CouchDB, MongoDb
- Graph Databases: Instead of tables of rows and columns and the rigid structure of SQL, a flexible graph model is used which, again, can scale across multiple machines.

From the available document databases, MongoDB was considered, as being the most deployed open source database system.

A record in MongoDB is a document, which is a data structure composed of field and value pairs. MongoDB documents are similar to JSON objects. The values of fields may include other documents, arrays, and arrays of documents.

The advantages of using documents are:

- Documents (i.e. objects) correspond to native data types in many programming languages.
- Embedded documents and arrays reduce need for expensive joins.
- Dynamic schema supports fluent polymorphism.

MongoDB provides high performance data persistence. In particular:

- Support for embedded data models reduces I/O activity on database system.
- Indexes support faster queries and can include keys from embedded documents and arrays.

MongoDB supports a rich query language to support read and write operations (CRUD) as well as data aggregation, text search and geospatial queries.

MongoDB's replication facility, called replica set, provides automatic failover and data redundancy. A replica set is a group of MongoDB servers that maintain the same data set, providing redundancy and increasing data availability.

MongoDB provides horizontal scalability as part of its core functionality:

- Sharding distributes data across a cluster of machines.
- Tag aware sharding allows for directing data to specific shards, such as to take into consideration geographic distribution of the shards.

After deciding to adopt MongoDB for this project, the main interest was to identify a proper setup that could be used for storing atomic data. In this context, it was considered that atomic data is very expensive to produce (it either takes a lot of time to run simulation codes, or it is actually expensive to run experiments in order to obtain experimental data). Therefore, the main concern was with data redundancy.

The second concern was with scalability for both size and speed. Simulation codes can produce terabytes of data, which could quickly consume all the available storage capacity of a database. Also, large volumes of data imply performance issues if there are bottlenecks at storage level. Therefore, the database should be able to scale and distribute the workload efficiently between nodes.

For data redundancy, MongoDB offers replication features. A replica set is a group of mongod instances that maintain the same data set. A replica set contains several data bearing nodes and optionally one arbiter node. Of the data bearing nodes, one and only one member is deemed the primary node, while the other nodes are deemed secondary nodes. The secondaries replicate the primary's oplog and apply the operations to their data sets such that the secondaries' data sets reflect the primary's data set. If the primary is unavailable, an eligible secondary will hold an election to elect itself the new primary. At this time however, for the purpose of the current project, only the actual replication will be used as part of the replica set configuration in MongoDB. Nevertheless, it is important to note that MongoDB also offers features that can aid in performing backups and it also opens the possibility to have multiple datacenters.

Sharding is a method for distributing data across multiple machines. MongoDB uses sharding to support deployments with very large data sets and high throughput operations.

For the purpose of this project, several noSQL databases and concepts were investigated. After careful consideration, due to the available set of features, MongoDB was chosen as the main database to be used for the rest of the project. An initial deployment was realized, containing 12 MongoDB instances, configured in a cluster and one stand alone instance, for quick development and testing. Various specific features were considered and several optimisations to the default installation have been performed. Since MongoDB has a specific query language, different from SQL, it was necessary to investigate how generic database tasks can be performed in MongoDB. During the next stages of the project, it is foreseen to use the gathered knowledge in order to implement a small application handling atomic data stored inside MongoDB.

Preparation of exploitation of JT-60SA (I)

Sorin Soare

National Institute for Cryogenics and Isotopic Technologies, ICIT

WP- WPSA

The polarimeter system development started few years ago and has the unique capability to provide information on plasma magnetic structure of plasma using INTERNAL measurements. The operation principle is based on:

- the Faraday Rotation Effect; it is the only technique that can provide the magnetic field information using internal measurements during the entire plasma cycle (start-up, flat-top and ramp-down).
- the Cotton-Mouton phase shift; the plasma is birefringent so a laser beam passing through plasma become elliptically polarised due to the interaction of the laser beam with the perpendicular components to the propagation direction. So the two orthogonal components of the polarisations have a phase shift called Cotton-Mouton angle.

Due to these two techniques the polarimeter diagnostic could be evolve at the status of basic machine control (protection and density feedback control). The vertical channels can provide absolute electron line-integrated measurements fringe jumps free similarly as is already used on JET fusion experiment[1].

The results obtained during 2015 refer to obtaining the required CAD information from JAEA team with the constraints (part of them) for polarimeter optics from JAEA. The remaining constraints were identified / received as part of the contract associated to the present one and detailed accordingly.

2. CAD requirements for in vessel components locations (Corner Cubes)

The JAEA provided to the WPSA team the full design of the JT60SA vacuum vessel including the in-vessel first wall as well as the design constraints[1] of polarimeter on JT60SA in May 2016. The installation of any plasma facing components has an impact on the overall design of the inner wall inside the vacuum vessel of the JT60SA machine and this has to be agreed at a very early stage in the design.

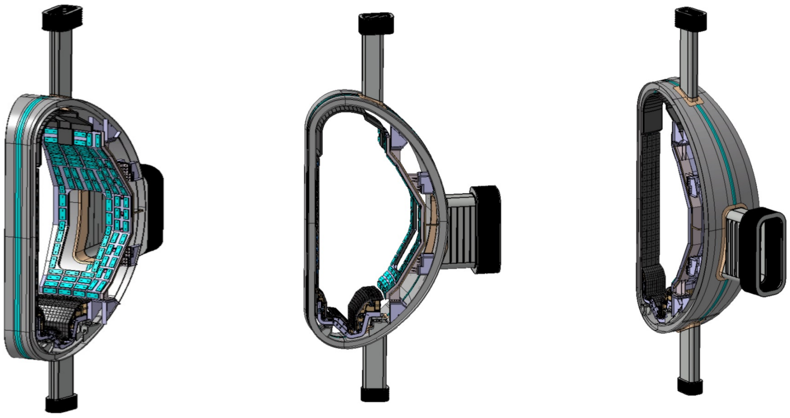

Figure 1 Overview of JT60SA vacuum vessel and first wall CAD that JAEA provided

2.1 Constraints

Constraints #1

The first constraints are related with the maximum volume of the corner cube-reflectors (CC) inside the first wall (FW), fig.1:

- Profile of the corner cube is maximum 80x80x80mm
- We have to request the alteration of the inner FW tiles and associated cooling as specified by JAEA
- Retro-reflector should be attached to FW Heatsink for the sake of both fixation and cooling.

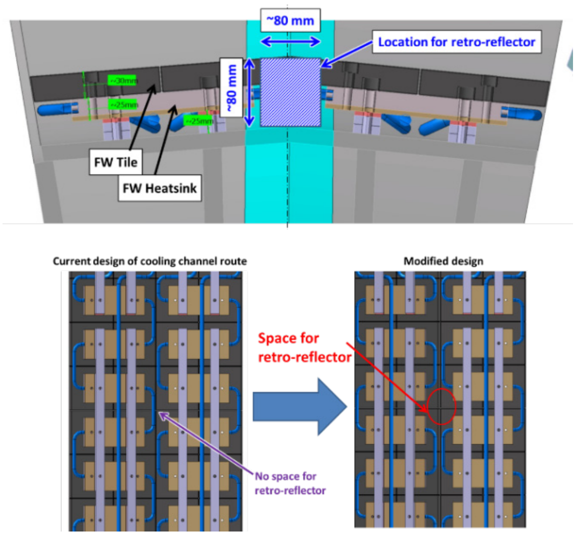

Figure 4 Centre of upper/equatorial port

Constraints #2

The second set of constraints is related with the heatsink and stabilising plate of the FW, fig. 2:

Retro-reflector can be attached to the heatsink on the stabilizing plate

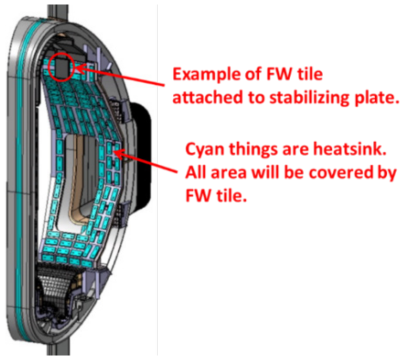

Figure 5 Divertor area

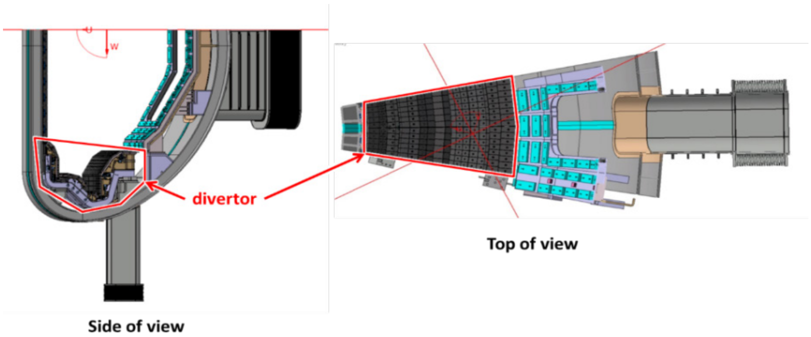

Figure 6 FW Stabilising plate area

Constraints #3

The third set of constraints refers with the divertor, fig. 3:

- No plan of making slits on divertor in order to enable a laser beam to pass through.
- No channels & corner cubes allowed in the divertor area

As it can be noticed we had very stringent constraints regarding the positions of CC and this impacted severely on the design choices reflected onto the Field of Views.

Preparation of exploitation of JT-60SA (II)

Sorin Soare

National Institute for Cryogenics and Isotopic Technologies, ICIT

WP- WPSA

The polarimeter system development started few years ago and has the unique capability to provide information on plasma magnetic structure of plasma using INTERNAL measurements. The operation principle is based on the Faraday Rotation Effect: a magnetised plasma is optically active and a linear polarised laser beam sent through a plasma suffer a rotation of the polarisation plane due to the interaction of the field component along the propagation direction and the angle of rotation is called Faraday Rotation angle. These measurements are the only ones that can provide the magnetic field information using internal measurements during the entire plasma cycle (start-up, flat-top and ramp-down).

A secondary measurement is, for relatively strong magnetic fields, the Cotton-Mouton phase shift. This is based on the Cotton-Mouton effect: the plasma is birefringent so a laser beam passing through plasma become elliptically polarised due to the interaction of the laser beam with the perpendicular components to the propagation direction. In technical term, the two orthogonal components of the polarisations that are measured have a phase shift called Cotton-Mouton angle. In certain circumstances, from these measurements, one can obtain absolute measurements of electron plasma density.

Due to these alone, the polarimeter diagnostic has a great potential to be elevated to diagnostic for basic machine control (machine protection and density feedback control) as with the vertical channels it can provide absolute electron line-integrated measurements fringe jumps free similarly as is already used on JET fusion experiment[1].

2. CAD requirements

The polarimeter diagnostic will require in-vessel reflector components (corner cubes retro-reflectors). These in-vessel components (CC) have to be located in the space envelope defined by the heat sink and First Wall tile with rigid fixture and cooling possibilities.

The installation of any plasma facing components has an impact on the overall design of the inner wall inside the vacuum vessel of the JT60SA machine and this has to be agreed at a very early stage in the design.

2.2 Fields of View Constraints

Constraints #1 and #2

Similar with divertor is the First Wall upper area and the space behind the stabilising plate

- No polarimeter channels allowed in the FW upper area
- No polarimeter channels allowed behind stabilising plate as this area will be occupied by coils

Constraints #3

JAEA given us some directives with respect the vacuum windows

- There is no generic design of a vacuum window
- Vacuum window with conventional ICF flange is applicable.
- We need to prepare “cover window” to protect the vacuum window. The cover window is not a vacuum boundary and has no function of vacuum confinement.

Constraints #4

This later refers to the additional engineering complications[2] due to vacuum vessel and port geometry:

- Poloidal port is not in the centre of the machine

- The vertical port is more than 2 meter long, 50cm wide and max 10 degrees field of view.

2.2 Ab-initio design of the in-vessel optical components compatible with the JT60SA machine constraints

This work was related mainly with the corner-cube reflectors. We have used as an example the corner cubes used for the ToreSupra (now West) machine in Cadarache France. Bulk cooled corner cubes in CuCrZr have been successfully used for years in long duration plasma. Due to the constraints #1 the corner-cubes can be localised in very specific location: between four support tiles.

1st Study of channel localisation

This was CAD driven and was dedicated to find the maximum number of channels that could potentially be installed. This first solution had the following output:

- Maximum 14 channels from which five vertical channels and nine lateral channels
- In-vessel 2-mirror telescopes for ALL vertical channels
- Free propagation for lateral channels
- CAD only driven
- "Beam" diameter 50mm
- No Gaussian beam calculations
- Two channels on two different planes (2.5 degrees toroidally) with respect the other twelve
- Corner cube reflectors in same poloidal plan

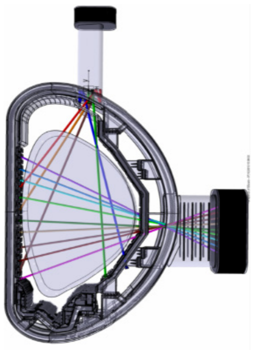

Figure 7 Maximum number of channels

A suitable CAD model for a random octant has been obtained from JAEA. On this model the no-go regions have been marked and should be observed in the future. Given these strict geometric boundaries a polarimeter system model with up to 14 channels can be considered suitable for JT60SA.

EUROfusion Secondment Agreement Nº NJOC/31

I. Jepu

National Institute for Lasers, Plasma and Radiation Physics, NILPRP

WP-PFC-S

The project EUROfusion Secondment Agreement Nº NJOC/31 represents a colaboration between National Institute for Laser, Plasma and Radiation Physics (NILPRP), part of the EUROfusion consortium and Culham Center for Energy Research (CCFE). The project consists of one person secondment from NILPRP to CCFE for 24 month period. During this time, the seconded personel will assist Erosion Deposition Group at CCFE with the installation and removal of long term samples in JET and to help co-ordinate distribution of samples for material migration and fuel retention studies as defined by the current work programme WPJET2.

Within the framework of the WP-PFC-S project the following activities have been performed at CCFE:

i) Attendance to a number of eight mandatory courses for the proper activity development around CCFE working site. These implied office safety instructions, responsible for information, UKAEA fire awareness, beryllium introductory courses on hazards, regulations, exposure to beryllium; work control trainings and risk assessment procedures; radiological protection courses. ii) Pulmonary medical tests and respiratory mask tests using a M3 mask, half mask, tornado hood and pressurised full suit costume for the entitlement as 'beryllium worker' necessary for the Beryllium Handling Facility (BeHF) work zone access. iii) Weekly participation to the FIVER (Follow-up In Vessel replacement) project meetings which consisted in technical and planning meetings. During the technical meetings a series of issues like necessary parts needed for the coming shutdown have not been order; availability of all necessary boxes for all the tiles to be removed in the shutdown as well as parts needed for the inner and outer divertor vacuuming process reporting. Planning meeting were dedicated to the Erosion and Deposition group activities related with the shutdown, the probability of not achieving some of the milestones in the plan and how this would affect the overall shutdown plans.

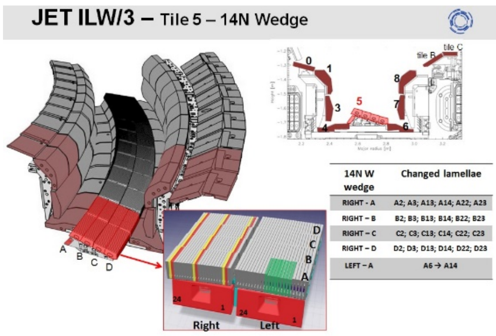

Figure 1 Module 14N wedge reconstruction

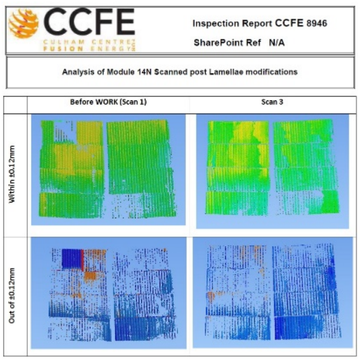

Figure 2 14N wedge inspection report after rebuilt phase

A series of JET 2017 Shutdown related activities have been performed CCFE:

1. 14N W – wedge reconstruction: one of the UKAEA milestones for the 2016 shutdown was the 14N wedge

module rebuilt which consisted of tile 5 reconstruction using new W lamellae. Based on the written method statement for this work procedure, the proper setup was achieved using the MPA tent in J1A facility, a controlled area in which personnel working on this particular job had to respect the beryllium regulations for an enclosed environment.

The reconstruction of the module is highlighted in figure 1. All the marked lamellae had to be replaced with brand new ones from the available stock. The proper technique for the disassembly and reassembly process was assured by the written method statement for this particular activity. After its assembly, an inspection using a point by point height measurement technique (Figure 2) was used to ensure the reconstruction of the 14Nwedge is in the permitted off scaled range to be re-fitted inside JET in the next shutdown campaign.

2. IWC inserts: a series of Inconel inserts have been manufactured according to technical specification ref: FIVER_ST_1420_T001, inspected and distributed for coating. The particularity of these inserts was that they are going to be placed inside a IWC tile, which is a Be coated Inconel and coated half with a 40 nm thick W at IPP Germany and 2.5 microns of Be for the other half at NILPRP in Romania.

3. KV6 system automatization: a new logic scheme was created for the automatization of the QMB devices which is in-situ measuring the deposition of eroded main chamber wall materials into JETs' divertor region. The aim was to replace the existing KV6 application with an automatization version of it, capable to measure these depositions which are part of the material migration phenomena, with no implication of any operators, based on pre-defined scenarios. The changes to the current KV6 application were required to provide an automated operation mode for opening the shutters of the QMBs, thus exposing the crystal during specified plasma conditions. The programme will enable the operator: *I) t*o operate the QMBs in an automated mode by defining particular plasma parameters which will determine a shutter opening interval of a QMB; *II) t*he operator will be required to define the times for the shutter opening interval of a QMB, with delay time start and advance close time. Based on the comparisons which the program will do between the operators set up parameters and the main system parameters, it will choose either to respect the time windows defined by the operator, or to overwrite it when at least one condition is not fulfilled; *III)* to set different conditions for each QMB system independently; *IV)* to define either a single or multiple shutter openings within a given JET pulse.

4. W lamellae cutting and distribution plan: The cutting of the W lamellae part of the 2010-2012 plasma operating tile 5 of the divertor was performed. This plan consisted in choosing the interest tile 5 areas for post mortem analysis out of the four stacks of lamellae characteristic to each individual W wedge. The cutting plan covered samples with different dimensions based on typical analysis to be performed on it. For D-NRA, SEM, EDX, LID and metallography techniques, the provided samples were 9x6x10 mm. For TDS type of samples, the chosen dimensions were 10x6x2.5 mm. (Figure 3)

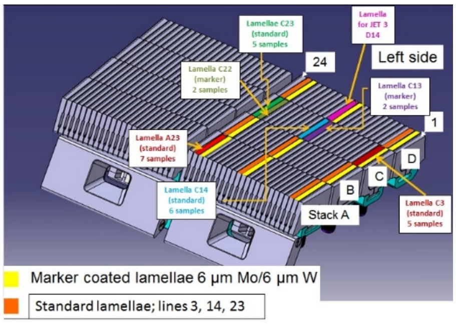

Figure 3 W lamellae distribution plan

5. KT5 diagnostics training was performed for in-situ monitoring of the sub-divertor pressure, main chamber pressure and elemental composition of residual gases collected during pulse mode and continuous mode of JET (Figure 4).

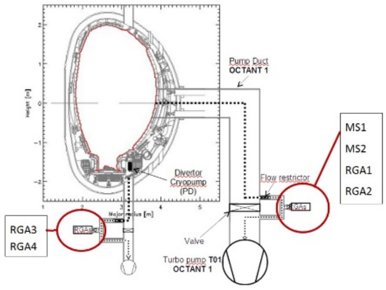

Figure 4 KT5 diagnostics positioning in respect with JET

6. Viewing system operator (VSO) training was performed, which is an in-situ infrared camera system monitoring the inner and outer walls of the main chamber as well as the divertor regions.

7. TDS analysis: the fuel outgassing efficiency in plasma-facing components exposed in JET-ILW has been studied at ITER-relevant baking temperatures. Samples retrieved from the W divertor and Be main chamber were annealed at 350 and 240°C, respectively. Annealing was performed with TDS for 0, 5 and 15 hrs to study the deuterium removal effectiveness at the nominal baking temperatures. Remained fraction was determined by emptying the samples fully of deuterium by heating W and Be samples up to 1000 and 775°C, respectively. Results showed the deposits in the divertor having an increasing effect to the remaining retention at temperatures above baking.

Conclusions

Within the framework of the WP-PFC-S project a series of training and courses were attended for the proper development of work activities under CCFE and UKAEA regulations. Managing activities regarding the JET shutdown plans have been undertaken. An UKAEA milestone was achieved by the reconstruction of the Tile5 of the divertor. TDS measurements on CFC clean samples cut from non-exposed CFC JET tile for beryllium – tritium cross-contamination level checking was performed. KT5 and VSO systems trainings have been achieved. A new automatization KV6 application was implemented for a better control of the in-situ deposition of migrating material from the inner and outer walls to the divertor region. The TDS analysis performed on JET samples highlighted the lack of efficiency of the long baking cycle. Desprtion of He from eurofer implanted samples was achieved proving the efficiency of the implantation method. Cutting plan for the W lamellae from the 2010-2012 campaign was elaborated in accordance with the analysis techniques required for the post mortem study.

Papers

[1] C.V. Atanasiu, L.E. Zakharov, D. Dumitru, Calculation of the reaction of a 3D thin wall to an external kink mode of rotating plasma, Romanian Reports in Physics 67, 2 (2015) 564-572.

[2] C.V. Atanasiu and L.E. Zakharov, Response of a partial wall to an external perturbation of rotating plasma, Phys. Plasmas 20, 092506 (2013).

[3] Curuia, M, Craciunescu, T., Soare, S. Zoita, V., Braic, V., Croft, D., Fernandes, A., Figueiredo, J., Goloborod'ko, V., Gorini, G., Griph, S., Kiptily, V., Lengar, I., Mianowski, S., Naish, J., Naish, R., Nocente, M., Pereira, R.C., Riccardo, V., Schoepf, K., Santos, B., Tardocchi, M., Yavorskij, V., Zychor, I., Upgrade of the tangential gamma-ray spectrometer beam-line for JET DT experiments, submitted to Fusion Eng. Des.

[4] A. Croitoru, D. Palade, M. Vlad, F. Spineanu, Turbulent transport of alpha particles, electronic preprint http://arxiv.org/abs/1603.08343, Nuclear Fusion 57 (2017) 036019.

[5] T. Craciunescu, A. Murari*, Geodesic distance on Gaussian manifolds for the robust identification of chaotic systems,* Nonlinear Dynamics 86—1 (2016) 677–693.

[6] C. Costin, V. Anita, G. Popa, J. Scholten, G. De Temmerman, "*Tailoring the charged particle fluxes across the target surface of Magnum-PSI*", Plasma Sources Sci. Technol. **25** (2016) 025023 (10pp).

[7] G. Carro, A. Muñoz, M.A.Monge, B. Savoini, A. Galatanu, M. Galatanu, R. Pareja,,Thermal conductivity and diffusivity of Cu-Y alloys produced by different powder metallurgy routes, Accepted in Fusion Engineering and Design.

[8] C Desgranges, M Firdaouss, C Hernandez, C Martin, C Ruset, E Grigore, M Missirlian, F Samaille and J Bucalossi, Study of the pores inside tungsten coating after thermal cycling for fusion device, Phys. Scr. T167 (2016) 014060 (7pp)

[9] Figueiredo, J., Murari, A., Perez Von Thun, C., Marocco, D., Tardocchi, M., Belli, F., García Muñoz, M., Silva, A., Soare, S., Craciunescu, T., Santala, M., Blanchard, P., Balboa, I., Hawkes, N., *JET diagnostic enhancements in preparation for DT operations*, Review of Scientific Instruments, 87 (11), art. no. 11D443, 2016.

[10] M. Galatanu, M. Enculescu, G. Ruiu, B. Popescu, A. Galatanu, Cu-based composites as thermal barrier materials in DEMO divertor components, Accepted in Fusion Engineering and Design.

[11] A. Galatanu, M. Galatanu, M. Enculescu, I. Enculescu, G. Ruiu, C. Stancu,W laminates produced by "FAST brazing", submitted to J of Nuclear Materials

[12] M. Galatanu, M. Enculescu, A. Galatanu, Thermal properties of micro- and nano- structured W-Cu functional gradient materials, submitted to J of Thermal Analysis and Calorimetry

[13] S.G. Greculeasa, P. Palade, G. Schinteie, G.A. Lungu, C. Porosnicu, I. Jepu, C.P. Lungu, V. Kuncser/ Be/W and W/Be bilayers deposited on Si substrates with hydrogenated Fe-Cr and Fe-Cr-Al interlayers for plasma facing components / Journal of Nuclear Materials, Volume 481, 1 December 2016, Pages 73-80

[14] E Grigore, C Ruset, M Gherendi, D Chioibasu, A Hakola and JET contributors, Thermo-mechanical properties of W/Mo markers coatings deposited on bulk W, Phys. Scr. T167 (2016) 014028 (4pp)

[15] M. Hoelzl, G. Huijsmans, P. Merkel, C.V. Atanasiu, K. Lackner, E. Nardon, K. Aleynikova, F. Liu, E. Strumberger, R. McAdams, I. Chapman, A. Fil, Non-linear Simulations of MHD Instabilities in Tokamaks Including Eddy Current Effects and Perspectives for the Extension to Halo Currents, Journal of Physics (2014): Conference Series 561 012011

[16] M. Hoelzl, G. Huijsmans, P. Merkel, C.V. Atanasiu, K. Lackner, E. Nardon, K. Aleynikova, F. Liu, E. Strumberger, R. McAdams, I. Chapman, A. Fil, Non-linear Simulations of MHD Instabilities in Tokamaks Including Eddy Current Effects and Perspectives for the Extension to Halo Currents, Journal of Physics (2014): Conference Series 561 012011

[17] H. Isliker, L. Vlahos, Th. Pisokas, D. Constantinescu, A. Anastasiadis, Fractional Transport in Turbulent Reconnection, submitted for publication.

[18] I. Jepu, M.J. Baldwin, D. Nishijima, R.P. Doerner, C. Porosnicu, C.P. Lungu, P. Dinca, A. Marin / The influence of fusion-relevant D2-0.1He plasma on Be-W mixed-materials / Journal of Nuclear Materials, http://dx.doi.org/10.1016/j.jnucmat.2016.10.031

[19] Ye.O. Kazakov , J. Ongena , J.C. Wright , S.J. Wukitch , E. Lerche , M. Mantsinen, D. Van Eester , T. Craciunescu , V.G. Kiptily , Y. Lin , M. Nocente , F. Nabais , F. Nave , Y. Baranov , J. Bielecki , R. Bilato , V. Bobkov, K. Crombe, A. Czarnecka, J. Faustin, R. Felton, M. Fitzgerald, D. Gallart, L. Giacomelli, T. Golfinopoulos, A. Hubbard, Ph. Jacquet, T. Johnson, M. Lennholm , T. Loarer, M. Porkolab , S. Sharapov , D. Valcarcel, M. Van Schoor, H. Weisen, Experimental Evidence for a Novel Method of Fast-Ion Generation in Multi-Ion Plasmas with RF Waves, submitted to Physical Review Letters.

[20] Kiefer, J. Wolfowitz, Annals of Math. Statistics 23, (1952), 462-466.

[21] J. N. Krejic, Z. Luzanin, I. Stojkovska, Appl. Num. Math. 70, (2013) 1-21.

[22] Kwiatkowski, R., Bołtruczyk, G., Gosk, M., Korolczuk, S., Mianowski, S., Szydłowski, A., Zychor, I., Braic, V., Costa Pereira, R., Craciunescu, T., Croft, D., Curuia, M., Fernandes, A., Goloborod'ko, V., Gorini, G., Kiptily, V., Lengar, I., Naish, J., Naish, R., Nocente, M., Schoepf, K., Santos, B., Soare, S., Tardocchi, M., Yavorskij, V., Zoita, V., CeBr3 –based detector for Gamma Spectrometer Upgrade at JET, submitted to Fusion Eng. Des.

[23] Mateus, R. ,Hakola, A., Tiron, V., Porosnicu, C., Lungu, C.P., Alves, E./ Study of deuterium retention in Be-W coatings with distinct roughness profiles / Fusion Engineering and Design, October 03, 2016, article in press

[24] H Maier, M Rasinski, U von Toussaint, H Greuner, B Böswirth, M Balden, S Elgeti, C Ruset and G F Matthews, Kinetics of carbide formation in the molybdenum–tungsten coatings used in the ITER-like Wall, Phys. Scr. T167 (2016) 014048 (4pp)

[25] M Mayer, S Krat, W Van Renterghem, A Baron-Wiechec, S Brezinsek, I Bykov, P Coad, Yu Gasparyan, K Heinola, J Likonen, A Pisarev, C. Ruset, G de Saint-Aubin, A. Widdowson and JET Contributors, Erosion and deposition in the JET divertor during the first ILW campaign, Phys. Scr. T167 (2016) 014051 (9pp)

[26] C. Mortici, T. M. Rassias, Soon-Mo Jung, Applied Mathematics Letters 40 (2015) 23–28.

[27] A.V. Muller, D. Ewert, A. Galatanu, M. Milwich, R. Neu, J.Y. Pastor, U. Siefken, E. Tejado, Melt infiltrated Tungsten-Copper composites as advanced heat sink materials for plasma facing components of future nuclear fusion devices, J.-H. You, submitted to Fusion Engineering and Design.

[28] A. Murari, T. Craciunescu, E. Peluso, M. Gelfusa, M. Lungaroni, L. Garzotti, D. Frigione, P. Gaudio, How to assess the efficiency of synchronization experiments in tokamaks, Nucl. Fusion 56 (2016) 076008.

[29] Murari, A., Figueiredo, J., Bekris, N., Perez Von Thun, C., Batistoni, P., Marocco, D., Belli, F., Tardocchi, M., Garcia Munoz, M., Silva, A., Soare, S., Craciunescu, T., Santala, M., Blanchard, P., Croft, D., *Upgrades of Diagnostic Techniques and Technologies for JET Next D-T Campaigns*, IEEE Transactions on Nuclear Science, 63 (3), art. no. 7497673, pp. 1674-1681, 2016.

[30] M. Negrea, Trajectories of a dust particle in a magnetic field with constant shear, Physics AUC 26, 28-33, 2016.

[31] M. Negrea, I. Petrisor, A. Shalchi, Stochastic field-line wandering in magnetic turbulence with shear, II. Decorrelation trajectory method, submitted for publication in Physics of Plasmas.

[32] N. Negrea, Trajectories of a dust particle in a "sheared slab" unperturbed magnetic configuration, Physics AUC, volume 26, 34-39, 2016.

[33] I. Petrisor, Radial diffusion of inhomogeneous shared stochastic magnetic field lines in tokamak plasma, Physics AUC, volume 26, 40-46, 2016.

[34] C Pardanaud, M I Rusu, G Giacometti, C Martin, Y Addab, P Roubin, C P Lungu, C Porosnicu, I Jepu, P Dinca, M Lungu, O G Pompilian, R Mateus, E Alves, M Rubel and JET contributors / Raman microscopy investigation of beryllium materials /PhysicaScripta 2016 (T167), 014027; doi:10.1088/0031-8949/T167/1/014027

[35] A. Shalchi, M. Negrea, I. Petrisor, Stochastic field-line wandering in magnetic turbulence with shear, I. Quasi-linear theory, Physics of Plasmas 23, 072306 (2016).

[36] G. Sonnino, G. Steinbrecher, A. Cardinali, A. Sonnino, and M. Tlidi, Family of probability distributions derived from maximal entropy principle with scale invariant restrictions, Phys. Rev. E 87 (2013) , 014104.

[37] G. Sonnino, A. Cardinali, G. Steinbrecher, P. Peeters, A. Sonnino, P. Nardone, Reference Distribution Functions for Magnetically Confined Plasmas from the Minimum Entropy Production Theorem and the MaxEnt Principle, subject to the Scale-Invariant Restrictions, Physics Letters A 377 (2013) 3061-3077.

[38] G. Sonnino, A. Cardinali, P. Peeters, and G. Steinbrecher, A. Sonnino, and P. Nardone, Derivation of reference distribution functions for Tokamak plasmas by statistical thermodynamics , Eur. Phys. J. D (2014) 68: 44.

[39] G. Sonnino, P. Peeters, A. Sonnino, P. Nardone and G. Steinbrecher, Stationary distribution functions for ohmic Tokamak-plasmas in the weak-collisional transport regime by MaxEnt principle. J. Plasma Physics (2015), 81(1), 905810116 .

[40] G. Sonnino, G. Steinbrecher, Generalized extensive entropies for studying dynamical systems in highly anisotropic phase space. Phys. Rev. E 89 (2014) 062106.

[41] G. Sonnino, J. Evslin, A. Sonnino, G. Steinbrecher, and E. Tirapegui, Symmetry group and group representations associated with the thermodynamic covariance principle, Phys. Rev. E 94, 042103 – (2016)

[42] G. Sonnino, A. Sonnino, J. Evslin, G. Steinbrecher, Determination of the Dynamic ITER Energy Confinement Time Scalings, Journal of Modern Physics, vol. 7, No 12, (2016). DOI: 10.4236/jmp.2016.712130. arXiv:1412.5935v4 [physics.plasm-ph]

[43] F. Spineanu, M. Vlad, On the late phase of relaxation of two-dimensional fluids: turbulence of unitons, electronic preprint https://arxiv.org/submit/1734036, New Journal of Physics (2017) accepted as invited contribution to Focus on Turbulence in Astrophysical and Laboratory Plasmas. http://dx.2.org/10.1088/1367-2630/aa5a3d

[44] G. Steinbrecher, G. Sonnino, Generalized Rényi Entropy and Structure Detection of Complex Dynamical Systems, arXiv:1512.06108v1 [physics.data-an](2015).

[45] G. Steinbrecher, A. Sonnino, G. Sonnino, Category theoretic properties of the A. Rényi and C.Tsallis entropies. Journal of Modern Physics, 7, 251-266, (2016), DOI: 10.4236/jmp.2016.72025, arXiv:1504.05552v3 [physics.data-an]

[46] G. Steinbrecher, G. Sonnino, Numerical Stability of Generalized Entropies, arXiv:1603.06240v3 [physics.data-an] (2016). Sent to publication.

[47] G. Steinbrecher, G. Sonnino, N. Pometescu, Maximal entropy distribution functions from generalized Rényi entropy, arXiv:1606.08730v3 [cond-mat.stat-mech] (2016). Sent to publication.

[48] G. Steinbrecher, B. Weyssow, "Generalized Randomly Amplified Linear System Driven by Gaussian Noise. Extreme Heavy Tail and Algebraic Correlation Decay in Plasma Turbulence", Physical Review Letters 92, 125003 (2004).

[49] K. Sugiyama, C. Porosnicu, W. Jacob, I. Jepu, C.P. Lungu / Investigation of deuterium retention in/desorption from beryllium-containing mixed layers / Nuclear Materials and Energy, Volume 6, January 2016, Pages 1-9

[50] K. Sugiyama, C. Porosnicu, W. Jacob, I. Jepu, C.P. Lungu, Nuclear Materials and Energy, Volume 6, January 2016, Pages 1-9

[51] A. Szilárd , A. R. Mészáros, Applied Mathematics and Computation, 229 (2014) 131–138.

[52]De Temmerman, G., Baldwin, M.J., Anthoine, D., Heinola, K., Jan, A., Jepu, I., Likonen, J., Lungu, C.P., Porosnicu, C., Pitts, R.A. /Efficiency of thermal outgassing for tritium retention measurement and removal in ITER/ Nuclear Materials and Energy 2016, article in press

[53]I. Tiseanu, T Craciunescu, M Lungu, C Dobrea and JET Contributors, X-ray micro-laminography for the ex situ analysis of W-CFC samples retrieved from JET ITER-like wall, Phys. Scr. T167 (2016) 014050 (8pp)

[54]G. Tigan, D. Constantinescu, Bifurcations in a family of Hamiltonian systems and associated nontwist cubic maps, accepted for publication (in 2016) in International Journal of Bifurcation and Chaos, will appear in 2017.

[55]M. Vlad, F. Spineanu, Random and quasi-coherent aspects in particle motion and their effects on transport and turbulence evolution, electronic preprint http://arxiv.org/abs/1611.08521, New Journal of Physics (2017), invited contribution to Focus on Turbulence in Astrophysical and Laboratory Plasmas. https://doi.org/10.1088/1367-2630/aa602d

[56]M. Vlad, F. Spineanu, Direct effects of the resonant magnetic perturbation on turbulent transport, Nuclear Fusion 56 (2016) 092003.

[57]Velicu, I.-L., Tiron, V. , Porosnicu, C., Burducea, I., Lupu, N., Stoian, G., Popa, G., Munteanu, D./ Enhanced properties of tungsten thin films deposited with a novel HiPIMSapproach / Applied Surface ScienceOctober 08, 2016, article in press;

[58]A. Widdowson, A. Baron-Wiechec, P.Batistoni, E. Belonohy, P. Coad, P. Dinca, D. Flammini, F. Fox, K. Heinola, I. Jepu, J. Likonen, S. Lilley, C. Lungu, G.Matthews, J.Naish, O Pompilian, C. Porosnicu, M.Rubel, R.Villari; Experience of handling beryllium, tritium and activated components from JET ITER Like Wall, Phys. Scr. T167 (2016) 014057-014067.

[59]L. E. Zakharov, C.V. Atanasiu, K. Lackner, M. Hoelzl, E. Strumberger, Electromagnetic Thin Wall Model for Simulations of Plasma Wall Touching Kink and Vertical Modes, J. Plasma Physics 81, 515810610 (2015).

[60]Zychor, I., Boltruczyk, G., Burakowska, A., Craciunescu, T., Fernandes, A., Figueiredo, J., Giacomelli, L., Gorini, G., Gierlik, M., Gosk, M., Grodzicka, M., Iwanowska-Hanke, J., Kaveney, G., Kiptily, V., Korolczuk, S., Kwiatkowski, R., Mianowski, S., Moszynski, M., Murari, A., Nocente, M., Pereira, R.C., Perseo, V., Rigamonti, D., Rzadkiewicz, J., Sibczynski, P., Santos, B., Soare, S., Syntfeld-Kazuch, A., Swiderski, L., Szawlowski, M., Szczesniak, T., Szewinski, J., Szydlowski, A., Tardocchi, M., Urban, A., Zoita, V.L., *High performance detectors for upgraded gamma ray diagnostics for JET DT campaigns*, Physica Scripta, 91 (6), art. no. 064003, (2016).

Conferences

[1] C.V. Atanasiu, L. E. Zakharov, Calculation of eddy currents in 3D thin multiply connected wall structures induced by a rotating plasma perturbation, Proceedings of the International Symposium on Fundamentals of Electrical Engineering 2014, paper 178, Bucharest, Romania, November 28-29, 2014 (invited paper).

[2] C.V. Atanasiu, L. E. Zakharov, K. Lackner, M. Hoelzl, E. Strumberger, Simulations of plasma wall-touching kink and vertical modes in tokamak, The Joint Meeting on Quantum Fields and Nonlinear Phenomena, 09-13 March 2016, Sinaia, Romania.

[3] C.V. Atanasiu, L. E. Zakharov, K. Lackner, M. Hoelzl, E. Strumberger, Simulation of surface currents excited by plasma wall-touching kink and vertical modes in tokamak, International Symposium on Fundamentals of Electrical Engineering, Bucharest, Romania, 30 June-2 July 2016, paper 351 (invited paper).

[4] L. Begrambekov , A. Evsin , Ch. Grisolia , A. Kaplevsky , A. Evsin , I Jepu , J-M. Layet , C. Lungu , C. Porosnicu , A. Zakharov / Hydrogen trapping into and release from tungsten covered by beryllium/aluminum oxide layer under plasma irradiation / International Conference on Plasma Surface Interactions in Controlled Fusion Devices, Rome, Italy, May 30 – June 3, 2016 / P2.4 - Poster

[5] D. Constantinescu, M. Negrea, I. Petrisor, Hamiltonian description of fast particles' dynamics in tokamak, International Conference on Applied Mathematics and Numerical Methods, Craiova, 14-16 April 2016

[6] D. Constantinescu, M. Negrea, I. Petrisor, Regular and chaotic dynamics in low dimensional Hamiltonian systems. Applications to the study of some transport phenomena in fusion plasma physics, Workshop on Qualitative Theory of Differential Equations and Singular Perturbation Theory, School of Mathematical Sciences Shanghai Jiao Tong University, May 6-8, 2016

[7] D. Constantinescu, Fractional dynamics. Applications to the study of some transport phenomena, invited lecture to Shanghai Normal University, Shanghai, China, May 17, 2016

[8] D. Constantinescu, Essentials on fractional calculus. Fractional differential equations and applications in physics and economics. invited lecture to Zhejiang Normal University, Jinhua, China, May 25, 2016

[9] D. Constantinescu, M. Negrea, I. Petrisor, Anisotropic fractional transport models in fusion plasmas, The Joint Meeting of Quantum Fields and Nonlinear Phenomena, Workshop on "Nonlinear Dynamics and Applications in Plasma Physics, March 09-13, 2016, Sinaia, Romania.

[10] Curuia, M, Craciunescu, T., Soare, S. Zoita, V., Braic, V., Croft, D., Fernandes, A., Figueiredo, J., Goloborod'ko, V., Gorini, G., Griph, S., Kiptily, V., Lengar, I., Mianowski, S., Naish, J., Naish, R., Nocente, M., Pereira, R.C., Riccardo, V., Schoepf, K., Santos, B., Tardocchi, M., Yavorskij, V., Zychor, I., Upgrade of the tangential gamma-ray spectrometer beam-line for JET DT experiments, 29th Symposium on Fusion Technology, Sept. 5-9, Prague, 2016.

[11] P. Dinca, O.G. Pompilian, C. Porosnicu, B. Butoi, I. Jepu, I. Burducea, C. P. Lungu / Structural and morphological influence on deuterium retention for Be-W pure and mixed layers exposed to low frequency D plasma / 16th International Balkan Workshop on Applied Physics (IBWAP), Constanta, Romania, 7-9 July, 2016 / S2 – O7 – Oral talk

[12] A. Galatanu, M. Galatanu, M Enculescu, G. Ruiu, C. Stancu, FAST brazing technology for W multi-metal laminates, 29th Symposium on Fusion Technology SOFT 2016, September 5-9, 2016, Prague, Czech Republic.

[13] A. Galatanu , M. Galatanu , A. Jianu, A. Weisenburger, "Heat Transfer Analysis for Metal-Liquid Lead Interface", Nuclear 2016 - Annual International Conference on Sustainable Development through Nuclear Research and Education , May 18-20, 2016, Pitesti, Romania.

[14] M. Galatanu, M. Enculescu, A. Galatanu, "Thermal properties of micro- and nano- structured W-Cu functional gradient materials", The 25th Symposium on Thermal Analysis and Calorimetry–Eugen SEGAL, April 15th, 2016, Bucharest, Romania.

[15] M. Galatanu, M. Enculescu, G. Ruiu, B. Popescu, A. Galatanu, Cu-based composites as thermal barrier materials in DEMO divertor components, 29th Symposium on Fusion Technology SOFT 2016, September 5-9, 2016, Prague, Czech Republic.

[16] D. Gallart, L. Giacomelli, J. Graves, Ph. Jacquet, N. Krawczy, M. Lennholm, T. Loarer, M. Mantsinen, A. Messiaen, I. Monakhov, F. Nave, T. Johnson, D. Valcarcel, H. Weisen, M. Schneider, Plasma heating and generation of energetic ions with novel three-ion ICRF scenarios on Alcator C-Mod and JET tokamak facilities, 58th Annual Meeting of the APS Division of Plasma Physics, San Jose, California, USA October 31 - November 4, 2016.

[17] K. Heinola, J. Likonen, T. Ahlgren, S. Brezinsek, I. Jepu, G. F. Matthews, R. A. Pitts, G. De Temmerman, A. Widdowson, JET Contributors / Long-term fuel retention and release in JET ITER-Like Wall at ITER-relevant baking temperatures / 26th IAEA Fusion Energy Conference, Kyoto, Japan, 17 – 22 October 2016
[18] I Jepu, A. Widdowson, K. Heinola, J.P. Coad, A. Baron-Wiechec, A. Ayres; "JET 2016 Shutdown, PFC/sample removal"; Ion Beam Analysis report meeting, 4-5th of April 2016, CCFE, CULHAM, UK – oral presentation;
[19] Yevgen Kazakov1, J. Ongena, D. Van Eester, R. Bilato, T. Craciunescu, R. Dumont, V. Kiptily, E. Lerche, M. Mantsinen, A. Messiaen, M. Nocente, S. Sharapov, J. Wright, S. Wukitch, Applications of Three-Ion ICRF Scenarios for Full-Field ITER Operation, Theory of fusion plasmas - Joint Varenna-Lausanne International Workshop, Varenna, Italy, Villa Monastero, Varenna, Italy August 29 – September 2, 2016.
[20] Y. Kazakov ,S. Wukitch, J. Wright, E. Edlund, Y. Lin, M. Porkolab, E.F. Jaeger, J. Ongena, E. Lerche, D. Van Eester, M. Nocente, V. Kiptily, T. Craciunescu, S. Sharapov, Y. Baranov, J. Bielecki, R. Bilato, V. Bobkov, A. Cardinali, C. Castaldo, K. Crombé, A. Czarnecka, R. Dumont, P. Dumortier, F. Durodie, J. Eriksson, J. Faustin, M. Fitzgerald, M. Rubel , P. Petersson , Y. Zhou , J.P. Coad , K. Heinola , C. Lungu , S. Brezinsek , C. Porosnicu , A. Widdowson and JET Contributors* / An Overview of Fuel Inventory and Deposition in Castellated Beryllium Structures in JET / International Conference on Plasma Surface Interactions in Controlled Fusion Devices, Rome, Italy, May 30 – June 3, 2016 / I-01 – Invited lecture
[21] N.S. Klimov, V.L. Podkovyrov , I.B. Kupriyanov , J. Linke , R.A. Pitts , V.M. Safronov , D.V. Kovalenko , Th. Loewenhoff , C.P. Lungu , G. Pintsuk , G. De Temmerman , A.D. Muzichenko , A.A. Markin , P.N. Taratorkin , N.E. Zabirova , A.M. Zhitlukhin / Beryllium layer response to ITER-like ELM plasma pulses in QSPA-Be / International Conference on Plasma Surface Interactions in Controlled Fusion Devices, Rome, Italy, May 30 – June 3, 2016 / P1.57 - Poster
[22] Kwiatkowski, R., Bołtruczyk, G., Gosk, M., Korolczuk, S., Mianowski, S., Szydłowski, A., Zychor, I., Braic, V., Costa Pereira, R., Craciunescu, T., Croft, D., Curuia, M., Fernandes, A., Goloborod'ko, V., Gorini, G., Kiptily, V., Lengar, I., Naish, J., Naish, R., Nocente, M., Schoepf, K., Santos, B., Soare, S., Tardocchi, M., Yavorskij, V., Zoita, V., CeBr3 –based detector for Gamma Spectrometer Upgrade at JET, 29th Symposium on Fusion Technology, Sept. 5-9, Prague, 2016.
[23] C. P. Lungu , C. Porosnicu , O. Pompilian , I. Jepu , O. Pompilian , M. Lungu , I. Tiseanu , C. Ayres , P. Coad, M. Rubel , A. Widdowson, Sectioning Techniques and Analysis of Selected Beryllium Tiles from JET-ILW, PSI 22nd, Plasma Surface Interactions in Controlled Devices, Rome, May 30 – June 3, 2016.
[24] M. Lungu, I. Tiseanu, C. Porosnicu, C. Dobrea / The study of erosion phenomena on fusion related marker samples by applying μXRF method / 16th International Balkan Workshop on Applied Physics (IBWAP), Constanta, Romania, 7-9 July, 2016 / S2 – O1 – Oral talk
[25] C. P. Lungu, C. Porosnicu, O. Pompilian, I. Jepu, M. Lungu, I. Tiseanu, C. Ayres, P. Coad, M. Rubel, A. Widdowson and JET Contributors, "Sectioning Techniques and Analysis of Selected Beryllium Tiles from JET-ILW", International Conference on Plasma Surface Interactions In Controlled Devices (PSI2016), 30 May – 3rd June 2016, Rome, ITALY – poster
[26] R. Mateus, M.C. Sequeira , C. Porosnicu , C.P. Lungu , E. Alves / Thermal and chemical stability of the β-W2N nitride phase / International Conference on Plasma Surface Interactions in Controlled Fusion Devices, Rome, Italy, May 30 – June 3, 2016 / P3.70 – Poster
[27] I. G. Miron, Modelling of seed magnetic island formation, 43rd EPS conference on Plasma Physics 4-8 July 2016, Leuven, Belgium.
[28] M. Negrea, I. Petrisor, D. Constantinescu, Motion of charged particles in tokamak perturbed toroidal magnetic field, The Joint Meeting of Quantum Fields and Nonlinear Phenomena, Workshop on "Nonlinear Dynamics and Applications in Plasma Physics, March 09-13, 2016, Sinaia, Romania.
[29] M. Negrea, I. Petrisor, D. Constantinescu, Influence of the gradient pressure and magnetic field inhomogeneity on dust dynamics in tokamak plasma, The Joint Meeting of Quantum Fields and Nonlinear Phenomena, Workshop on "Nonlinear Dynamics and Applications in Plasma Physics, March 09-13, 2016, Sinaia, Romania.
[30] S. Nowak, E. Lazzaro, O. Sauter, .., I. G. Miron et al, Effect of the EC torque on slow plasma rotation under central ECH/ECCD for NTM onset, 26th IAEA Fusion Energy Conference, Kyoto, Japan, 17–22 October 2016.
[31] C. Porosnicu, V. Tiron, P. Dinca, I. Jepu, O.G. Pompilian, I. Burducea, C. P. Lungu / HiPIMS And Reactive Magnetron Sputtering Techniques used for Obtaining Fusion Related Materials / 16th International Balkan Workshop on Applied

[32] M. Pribula , J. Karhunen , P. Paris , P. Veis , K. Piip , C. Porosnicu , C. Lungu , and A. Hakola / Determination of deuterium depth profiles in fusion-relevant wall materials by nanosecond LIBS / International Conference on Plasma Surface Interactions in Controlled Fusion Devices, Rome, Italy, May 30 – June 3, 2016 / P3.90 - Poster

[33] M. Rubel, P. Petersson, Y. Zhou, J.P. Coad, C. Lungu, I. Jepu, C. Porosnicu, D. Matveev, A. Kirschner, Brezinsek, A. Widdowson, JET Contributors / Fuel Inventory and Deposition in Castellated Structures in JET-ILW / 26th IAEA Fusion Energy Conference, Kyoto, Japan, 17 – 22 October 2016.

[34] M. Rubel , P. Petersson , Y. Zhou , J.P. Coad , K. Heinola , C. Lungu, S. Brezinsek , C. Porosnicu, A. Widdowson, An Overview of Fuel Inventory and Deposition in Castellated Beryllium Structures in JET, International Conference on Plasma Surface Interactions in Controlled Fusion Devices, Rome, Italy, May 30 – June 3, 2016, Invited lecture

[35] C. Ruset, D. Falie, E. Grigore, M. Gherendi, V. Zoita, K-D. Zastrow, G. Matthews, X. Courtois, J. Bucalossi, J. Likonen, JET Contributors, The emissivity of W coatings deposited on carbon materials for fusion applications, 29th Symposium on Fusion Technology, Prague, Czech Republic, September 5-9, 2016 – Poster

[36] M. I. Rusu, C. Pardanaud , C. Martin , Y. Addab , P. Roubin , Y. Ferro , E. Cannuccia , L. Ferry, F. Virot , M. Barrachin, C P Lungu , C Porosnicu , P Dinca , M Lungu , M. Köppen , P. Dollase , T. Dittmar , Ch. Linsmeier / Multi wavelength Raman microscopy: a tool sensitive to both structure and chemistry in Be containing samples mimicking future JET/ITER samples / International Conference on Plasma Surface Interactions in Controlled Fusion Devices, Rome, Italy, May 30 – June 3, 2016 / P2.63 - Poster

[37] M. Vlad, F. Spineanu, Turbulence and zonal-flow generation: a semi-analytical study based on the iterated self-consistent method, The Joint Meeting of Quantum Fields and Nonlinear Phenomena, Workshop on "Nonlinear Dynamics and Applications in Plasma Physics, March 09-13, 2016, Sinaia, Romania.

[38] G. Steinbrecher, G. Sonnino, N. Pometescu, Generalized Rényi entropy as Liapunov functional, maximal entropy distribution functions, International Workshop on "Nonlinear dynamics in Plasma Physics" - Sinaia, March 9-13, 2016.

[39] M. Suchoňová , M. Pribula , V. Martišovitš , J. Krištof , C. Porosnicu , C. P. Lungu , A. Hakola P. Veis / Detection of fuel and trace elements in plasma-facing components using RF-discharge enhanced LIBS / International Conference on Plasma Surface Interactions in Controlled Fusion Devices, Rome, Italy, May 30 – June 3, 2016 / P3.89 - Poster

[40] G. De Temmerman, M.J. Baldwin , D. Anthoin, K. Heinola , A. Jan, I. Jepu , J. Likonen , C.P. Lungu , C. Porosnicu , and R.A. Pitts; "Efficiency of thermal outgassing for tritium retention measurement and removal in ITER", International Conference on Plasma Surface Interactions In Controlled Devices (PSI2016), 30 May – 3rd June 2016, Rome, ITALY – oral talk

[41] A. Widdowson, K. Heinola, J.P. Coad, A. Baron-Wiechec, A. Ayres, I Jepu; "JET 2016 Shutdown activities, PFC/sample removal"; WPJET2 Annual Meeting, CIEMAT, Madrid, Nov.2016

Annex 1

Members of the EUROfusion Consortium:

Country	Institute, University or Finance Agency
Austria	Austrian Academy of Sciences, Vienna
Belgium	Ecole Royale Militaire-Koninklijke Militaire School, Plasma Physics Laboratory, Brussels
Bulgaria	Bulgarian Academy of Sciences, Institute of Nuclear Research and Nuclear Energy, Sofia
Croatia	Ruđer Bošković Institute, Zagreb
Cyprus	University of Cyprus, Nicosia
Czech Republic	Academy of Sciences of the Czech Republic, Institute of Plasma Physics, Prague
Denmark	DTU, Plasma Physics and Fusion Energy, Lyngby
Estonia	University of Tartu, Institute of Physics
Finland	VTT Technical Research Centre of Finland, Espoo
France	Commissariat à l'énergie atomique et aux énergies alternatives,CEA, Cadarache
Germany	Forschungszentrum Jülich, FZJ; Karlsruhe Institute of Technology, KIT; Max Planck Institute of Plasma Physics, IPP, Garching and Greifswald
Greece	National Center For Scientific Research "DEMOKRITOS", Athens
Hungary	Hungarian Academy of Science, Wigner Research Centre for Physics, Budapest
Ireland	Dublin City University, Plasma Research Laboratory
Italy	Agenzia nazionale per le nuove tecnologie, l'energia e lo sviluppo economico sostenibile, ENEA (Italy), Frascati
Latvia	University of Latvia, Institute of Solid State Physics, Riga
Lithuania	Lithuanian Energy Institute, Kaunas
The Netherlands	FOM, Foundation for Fundamental Research on Matter, Utrecht
Poland	Institute of Plasma Physics and Laser Microfusion, Warsaw
Portugal	Universidade Técnica de Lisboa, Instituto Superior Técnico, IST IPFN
Romania	Institutul de Fizica Atomica (IFA), Illfov
Slovakia	Comenius University, Department of Experimental Physics, Bratislava
Slovenia	JSI Jozef Stefan Institute, Ljubljana
Spain	Centro de Investigataciones Energeticas, Medioambientales y Tecnologicas, (CIEMAT), Madrid
Sweden	Vetenskapsrådet, Stockholm
Switzerland	École Polytechnique Federale de Lausanne EPFL, Swiss Plasma Center (SPC), Lausanne
United Kingdom	Culham Centre for Fusion Energy (CCFE), Host to JET

Annex 2

EUROfusionWork Packages:

- WPJET1 JET Campaign*
- WPJET2 Plasma-Facing Components*
- WPJET3 Technological Exploitation of DT Operation*
- WPJET4 JET Enhancements*
- WPMST1 Medium-Size Tokamak Campaigns*
- WPMST2 Preparation of the exploitation of Medium Size Tokamaks
- WPPFC Preparation of efficient PFC operation for ITER and DEMO*
- WPDTT1 Assessment of alternative divertor geometries and liquid metals PFC
- WPDTT2 Definition and design of the DTT
- WPSA Preparation of exploitation of JT-60SA*
- WPS1 Preparation and Exploitation of W7-X Campaigns
- WPS2 Stellarator Theory Development and Modelling
- WPCD Integrated Tokamak Modelling Code*
- WPISA Infrastructure Support Activities*
- WPPMI Plant Level System Engineering, Design Integration and Physics Integration
- WPMAG Magnet system*
- WPBB Breeding blanket
- WPCS Containment Structures
- WPDIV Divertor
- WPHCD Heating and current drive systems
- WPTFV Tritium, fuelling & vacuum systems
- WPBOP Heat transfer, balance-of-plant and site
- WPD&C Diagnostic and control
- WPRM Remote Maintenance Systems
- WPMAT Materials*
- WPENS Early Neutron Source
- WPSAE Safety and Environment
- WPSES Socio Economic studies
- WPPI Public Information
- WPEDU Education*
- WPTRA Training
- WPENR Enabling Research*
- WPPMU Management*

* with Romanian participation

Collaborations of Romanian teams:

- *Max Planck Institute for Plasma Physics, Garching, Germany*
  (National Institute for Laser, Plasma and Radiation Physics, Romania; pag 13)
- *Consorzio RFX (CNR, ENEA, INFN, Universita' di Padova, Acciaierie Venete SpA), Corso Stati Uniti 4, 35127 Padova, Italy*
  (National Institute for Laser, Plasma and Radiation Physics, -, Romania, pag 32)
- *Instituto de Plasmas e Fusão Nuclear, Instituto Superior Técnico, Universidade de Lisboa*
  (Institute of Atomic Physics, Bucharest, Romania; pag 40)
- *University of Rome "Tor Vergata", Via del Politecnico 1, 00133 Rome, Italy*
  (National Institute for Laser, Plasma and Radiation Physics, -, Romania, pag 32)
- *University of Innsbruck, Fusion@Österreichische Akademie der Wissenschaften, Austria*
  (Institute of Atomic Physics, Bucharest, Romania; pag 40)
- *Instituto di Fisica del Plasma "Piero Caldirola«, Consiglio Nazionale delle Ricerche, Milano, Italy*
  (Institute of Atomic Physics, Bucharest, Romania; pag 40)
- *Slovenian Fusion Association (SFA), Jozef Stefan Institute, Reactor Physics Department, Ljubljana, Slovenia*
  (Institute of Atomic Physics, Bucharest, Romania; pag 40)
- *Institute of Plasma Physics and Laser Microfusion, Warsaw, Poland,*
  (Institute of Atomic Physics, Bucharest, Romania; pag 40)
- *Princeton Plasma Physics Laboratory, Princeton, USA*
  (National Institute for Laser, Plasma and Radiation Physics, Romania; pag 13)

INSTITUTE OF ATOMIC PHYSICS
407 Atomistilor St., Magurele, ILFOV, 077125, P.O.Box MG-3, ROMANIA
Phone: (+4021) 457.44.93, (+4031) 710.15.54
Fax: (+4021) 457.44.56
e-mail: contact@ifa-mg.ro
www.ifa-mg.ro